UNIVERSITÀ DEGLI STUDI FIRENZE

DOTTORATO DI RICERCA IN
Fisica e Astronomia

CICLO XXXIII

COORDINATORE Prof. Raffaello D'Alessandro

PROBA-3: coronografia spaziale in *formation flight*

Settore Scientifico Disciplinare FIS/06

Dottorando
Dott. Noce Vladimiro
(firma)

Tutore
Prof. Marco Romoli
(firma)

Coordinatore
Prof. Raffaello D'Alessandro
(firma)

Anni 2017/2021

A mia madre

Acknowledgments

I would like to acknowledge the support of my supervisor, Prof. Marco Romoli, and all the colleagues of the Dept. of Physics and Astronomy in Florence and the INAF - Astrophysical Observatory of Turin who were of great help during my research. In particular my thanks go to Davide Loreggia, Gerardo Capobianco and Massimiliano Belluso with whom I have cooperated on the main parts of my research work, namely the numerous test activities and documents produced. I would like also thank Mauro Focardi, for having me introduced to PROBA-3 project, Silvano Fineschi for his advice and support and Steven Buckley for the huge work done on SPS design and development. Finally, many thanks to my family: Marina, Federico and Giulia for the support given.

Contents

Chapter 1

Introduction

This thesis gathers the work done during my Ph.D. dedicated to the co-engineering and analysis of the performance of the SPS (Shadow Position Sensor) electronics readout board within the ESA PROBA-3 project.

SPS is a subsystem of ASPIICS (Association of Spacecraft for Polarimetric and Imaging Investigation of the Corona of the Sun), the coronagraph telescope of the PROBA-3 ESA two-satellites formation flying mission, and has the purpose of sensing the penumbra cast from the occulter disk placed at a distance of about 150 meters around the instrument aperture to determine the correct alignment of the two satellites.

Beside its scientific tasks, PROBA-3 is a technology demonstration mission too, whose aim is to reach unprecedented goals in terms of relative positioning accuracy of its two spacecraft flying in formation. Under this aspect, SPS is crucial to obtain the desired performance.

The present thesis work describes the process of SPS electronics design from phase B2 (end of the preliminary design definition) to just before the qualification and production of the Flight Model (phase D).

1.1 PROBA-3

PROBA-3[1] is part of a series (PROBA - PRoject for On-Board Autonomy) of ESA missions dedicated to in-orbit demonstration of technologies. This

[1]The part of this section describing the PROBA-3 mission has been published as "Metrology on-board PROBA-3: the Shadow Position Sensors subsystem" in *Advances in Space Research (Special Issue: Sat Constellations and FF), 2020* [36].

mission [27], in particular, is devoted to the validation of formation-flying (FF) [18] techniques of two satellites named, respectively: CSC (Coronagraph S/C, about 340 kg, hosting the Coronagraph Instrument - CI) and OSC (Occulter S/C, 150 kg and shaped as a disk 1.4 m diameter), forming a giant externally occulted Lyot[2] coronagraph. To accomplish the payload scientific tasks, PROBA-3 will ensure millimeter level reciprocal positioning of its two satellites using closed-loop on-board metrology.

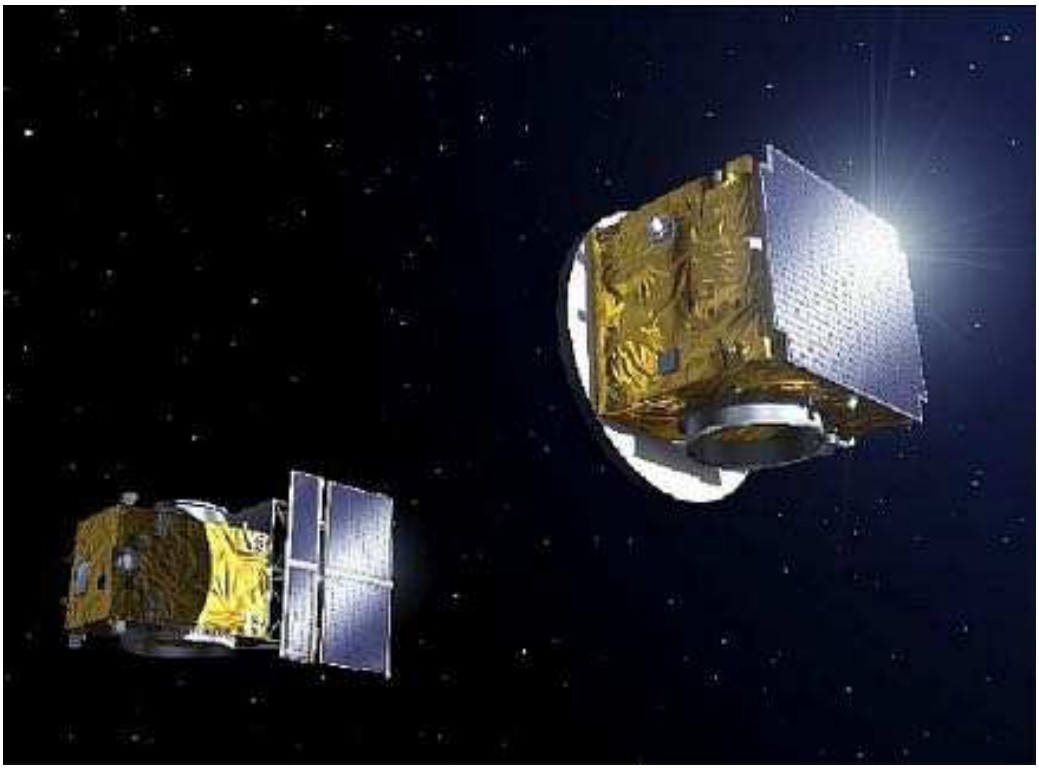

Figure 1.1: Picture showing the two spacecrafts composing the PROBA-3 mission, the distance is not to scale (Courtesy ESA).

The two spacecrafts will orbit around the Earth on an elliptic path (from 600 km to 60 530 km, 59° inclination and 19^h38^m period), allowing periodical observations of the solar corona in optimal conditions at orbit apogee.
The highly elliptical orbit does not permit the continuous remote control from Earth, then, the GNC (Guidance, Navigation and Control) system will maintain the formation in full autonomy.

[2]Bernard Lyot (1897 - 1952) is the inventor of the occulted solar coronagraph [25].

When passing near the Earth, using GPS, PROBA-3 will calculate the relative positioning and velocities of the two spacecraft and will propagate them to the next apogee passage, where a suite of metrology systems will gradually permit to reach the observation positioning i.e. the perfect alignment (at millimeter level) of the two spacecraft with respect to the Sun direction. In formation keeping, PROBA-3 will fly in strict formation for about eight hours, including formation acquisition and break, allowing scientific observations. In the rest of the orbit, the two S/C will reach a safe, collision risk free, reciprocal configuration (about 250 m apart) until approaching the apogee when they will regain the formation at the nominal ISD (Inter-Satellite Distance) of 144-146 m (season dependent).

The PROBA-3 mission is designed to execute autonomously its orbital activities without any support from ground for more than seven days (or eight orbits). The duration of the mission is two and half years, including a period of four months for commissioning.

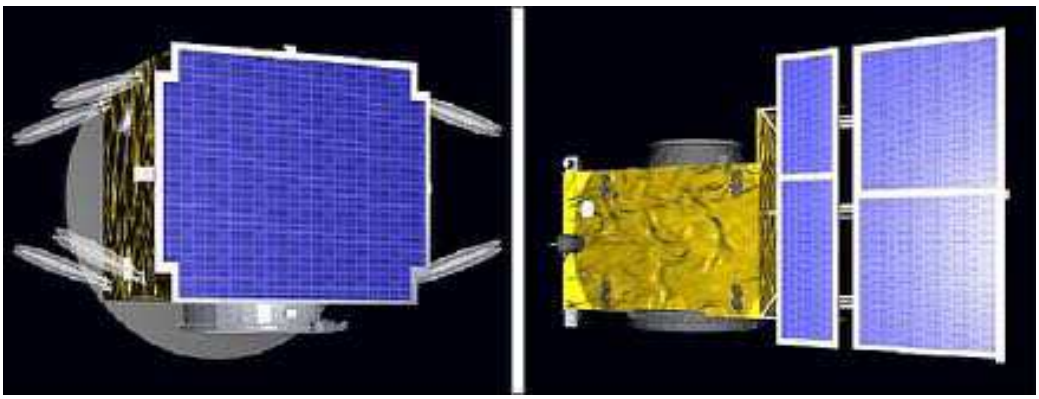

Figure 1.2: The two spacecrafts, OSC (Occulter S/C) (left) and CSC (Coronagraph S/C) (right), composing the PROBA-3 mission (Courtesy ESA).

1.2 ASPIICS

The two satellites forming PROBA-3 will realize, when aligned with the Sun, a 150-meter-long coronagraph whose scientific purpose is to study the solar corona closer to the solar limb than has ever been achieved before ($1.08R_{\odot}$). The instrument [52] [43] is called ASPIICS (Association of Spacecraft for Polarimetric and Imaging Investigation of the Corona of the Sun) and is

composed of two parts: the Coronagraph Instrument and the External Occulter.

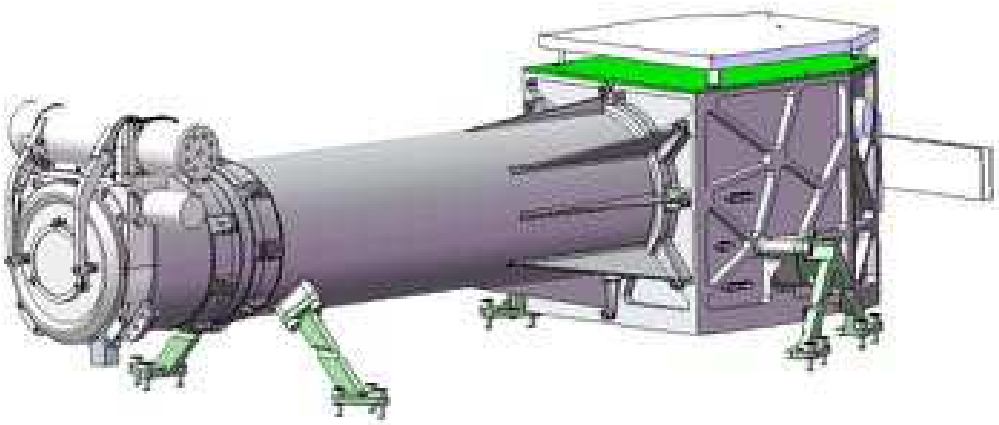

Figure 1.3: ASPIICS mechanical drawing

The Coronagraph Instrument represents the telescope portion of an externally occulted Lyot coronagraph [25]. The External Occulter (EO) is a disk 1.4 meters diameter placed on the second spacecraft OSC (for a detailed description, see scheme 2.6).

In visible light, the brightness of the Sun corona is less than one million times lower than that of the Sun disk (from 10^{-6} near the disk to 10^{-9} at $5R_{\odot}$). In practice, in every optic instrument part of the incoming light is diffused and in coronagraphs this parasitic light comes from a source so intense (the Sun disk) that it can be orders of magnitude higher than the coronal light we want to observe. For this reason it is necessary to obscure the disk and adopt measures to limit the light diffused from the occulter's edge in order to observe properly the corona with a sufficient SNR (Signal-to Noise Ratio).

For its proximity to the solar surface this zone is of primary interest for solar physics because it is the place where the plasma is heated to million degrees temperatures and the most energetic phenomena take place (e.g. CME, coronal mass ejections). Furthermore, the solar wind origins from here and is accelerated to asymptotic speeds. Until now, previous space-based,

Sun-observing missions, hosted internally (e.g. SOHO) or externally occulted coronagraphs (e.g. SOHO, STEREO, Solar Orbiter, etc.). In both cases, the occulting efficacy is limited by stray-light caused by the diffraction of the Sun disk light on the edge of the occulter; this phenomenon is ultimately linked to the occulter diameter and distance. With its 1.4 meter diameter occulter hosted on a separate spacecraft, PROBA-3 provides an optimal solution for maintaining an almost perfect total solar eclipse (as the one produced by the Moon) continuously adjusting the Occulter S/C in front of the Coronagraph S/C.

1.3 SPS - *Shadow Position Sensor*

PROBA-3 GNC system will progressively use several metrology systems to reach the desired absolute and relative position and attitude of the two spacecraft with unprecedented accuracy. The last metrology system intervening in the loop is SPS [15] [16] [37], a crown of sensors placed around the coronagraph entrance pupil diaphragm, sensing the Sun penumbra cast by the occulter spacecraft. Figure 1.4 shows the location of the SPS sensors behind the door aperture.

SPS[3] measures the illumination level on eight SiPM (Silicon Photomultipliers) arranged on a circle of 55 mm radius around the coronagraph entrance pupil and runs a dedicated on-board algorithm that translates the light measured on opposite sensors into a 3D position of the pupil's center around its nominal position. The eight sensors are hosted on a circular PCB and split into two sets (A and B) that can be switched on and off independently.

A transimpedance amplification stage converts the SiPM current into a voltage covering with margin the desired illumination range (Low Gain - LG), then, an amplification $\times 5$ enhances the resolution for low luminosities (High Gain - HG).

A 12-bit serial ADC, working at 4.16 MHz, samples the analog signals at a rate of 32.5 ksps (samples per second), then an FPGA operates a running average on the digitized data and provides the proper value, LG or HG, to the algorithm.

[3]The part of this section relative to SPS description has been published as "Metrology on-board PROBA-3: The Shadow Position Sensor (SPS) subsystem" in *Nuovo Cimento (Colloquia: SoHe3 2018), vol. 42C, pag. 27, 2019* [35].

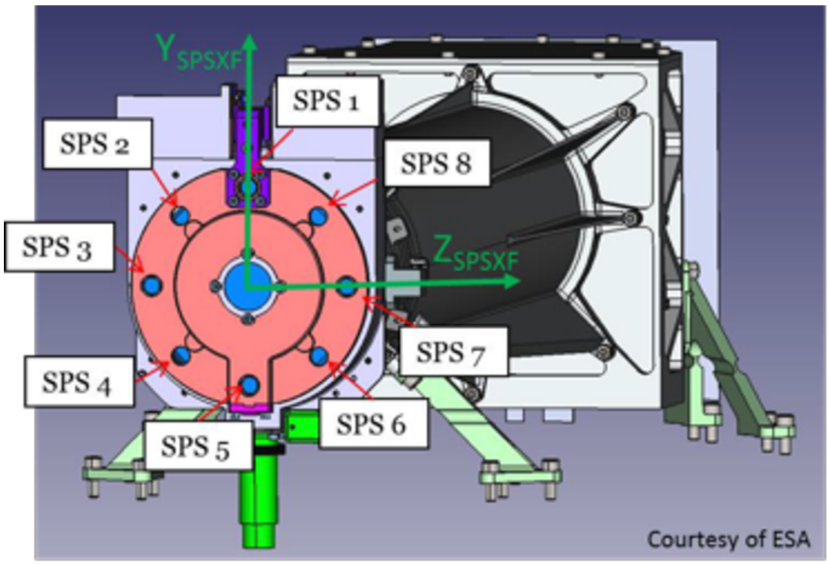

Figure 1.4: Location and numbering of the eight SPS sensors with respect to the reference system.

Extensive electrical and functional tests have been performed on the development models foreseen by the model philosophy, and the lessons learned led to several changes implemented in the final design.

1.4 Organization of the thesis

This thesis work is organized as follows: after this introduction, Chapter 2 describes the two main aims of PROBA-3 project: the ASPIICS instrument and the formation-flying opportunities. This chapter explains why the best conditions for solar corona observations in visible light are from space and how PROBA-3 can reproduce an almost ideal eclipse similar to the ones created by the Moon. They are illustrated, from a scientific point of view, the benefits that the mission will bring to the study of the Sun, how its observations will fit in the context of solar observatories in space and the connection between formation-flying accuracy and coronagraphic performance. Furthermore, we focus on the concept of Formation Flying, on a description of PROBA-3 GNC operations and of the different mission phases, and on the relative positioning accuracy that can be obtained.

Chapter 3 describes in detail the SPS, the *Shadow Position Sensor* sub-

system, the requirements it must satisfy, the penumbra simulations, the physical chain bringing from stimulus to measurements and the algorithms used to recover data.

From Chapter 4 to the end the various phases of SPS development and design evolution are explained.
These sections contain my contribution to PROBA-3 that mainly consisted in performing analyses and laboratory tests on all the SPS electronics models. The results were documented in several *design justification documents* and led to important design changes. Furthermore I wrote, or contributed to write, technical documentation (Part Stress Analysis, Failure Mode Effects Analysis, Worst Case Analysis, Error Budget etc.) required during the project progress.

In particular, Chapters 4 and 5 describe the various phases of SPS design development, the choices made, the lessons learned from theoretical analyses and from the tests on the different models. An additional development model (ADM - Advanced Demonstration Model) has been produced by INAF in order to represent more faithfully the electronics status.

Chapter 6 deals with the qualification process that consisted in several electric, functional and environmental tests on the EQM (Engineering Qualification Model).

Last chapter outlines the future activities: SPS radiometric calibration, integration in the spacecraft and acceptance process. After the launch, planned in 2022, it will be necessary to calibrate in-flight the penumbra profile, at the mission beginning, and, periodically, the SPS electronics.

Chapter 2

Coronagraphy and Formation Flying with PROBA-3

Observing the Sun from space has the unique benefit of the absence of an atmosphere and consequently of the Rayleigh scattering of light producing the blue sky. This is particularly important for coronagraphy because the total brightness of the solar corona is less than one millionth of the brightness of the Sun, comparable or less than the sky brightness.
Stray light rejection inside the telescope is an additional aspect extremely important for the quality of observations and requires occultations of the solar disk in order to simulate a natural total eclipse.

The performance of a coronagraph improves with the distance between the occulter and the telescope; the farther is the occulter, closer to the disk it is possible to observe the inner corona. For space observatories the deployment of large structures can rapidly become prohibitive due to limitations in weight, mass and, ultimately, by cost concerns.
A solution to the problem of the cost and feasibility for placing in space structures larger than what could be hosted on a single spacecraft can be found in satellites' formation flying (FF) techniques [53].

In recent years there were significant progresses in the field of multiple satellite missions, e.g. the PRISMA mission [3] (SNSA - Swedish National Space Agency 2010 - 2013/2016) demonstrated formation flying (and *rendezvous*) capabilities maintaining its two small satellites, named Mango and Tango, across tens of meters with a centimeter level accuracy using a combination of: relative GPS, visual-based systems and RF link. TanDEM-X [20] (DLR - Germany 2010 - to date) mission, instead, is able to control au-

tonomously the formation of its two spacecrafts with an accuracy of 10 m over typical distances of 250-500 m using relative GPS.

In the next future, PROBA-3 [26] will represent the cutting edge of precise relative positioning between spacecrafts and will be used to test formation flying technologies applicable to future ESA missions.

2.1 PROBA-3 mission

PROBA-3 (*PRoject for On-Board Autonomy*) is the fourth of a series of ESA missions dedicated to in-orbit demonstration of technologies:

1. PROBA-1 (2001 - to date): a small satellite dedicated to hyperspectral observations of Earth. Still operative, has long outlived the two year mission duration initially planned.
2. PROBA-2 (2009 - to date): solar corona observations in EUV (SWAP instrument, operating at 17.4 nm) and *space weather*.
3. PROBA-V (*Vegetation*, 2013 - to date): monitoring the worldwide vegetation.

PROBA-3 mission aims [39] at demonstrating formation-flying capabilities in the deployment of a large telescope in space, obtained by aligning periodically two satellites, named CSC (Coronagraph Spacecraft) and OSC (Occulter Spacecraft) in the direction of the Sun and creating a giant coronagraph.
The relative positioning requirement is at millimeter level, thus getting the highest precision ever reached in formation flying.
The mission will orbit around Earth on a Highly Elliptical Orbit (HEO) with about 20 hours period; the formation will be acquired near the apogee and broken during the perigee passages.

The mission is designed to demonstrate formation flying in the context of a large-scale science experiment, but, beside its scientific interest, this experiment will be the ideal ground to measure the achievements of the precise positioning of the two spacecrafts.
With the deployment of ASPIICS (see Section 2.4.3), the two satellites will form a giant solar coronagraph to study the solar corona closer to the limb than has ever done before. In addition, a second instrument, DARA (*Davos Absolute Radiometer*), will be hosted inside the OSC, dedicated to precise measurements of the Totat Solar Irradiance [47].

Launch date	End 2022
Coronagraph spacecraft mass	340 kg
Occulter spacecraft mass	200 kg
Orbit eccentricity	0.811
Orbit inclination	59°
Orbital period	19h 38m
Apogee height	60 530 km
Perigee height	600 km
Ground station	Santa Maria (Azores, Portugal)

Table 2.1: PROBA-3 facts and figures

2.2 Orbit and mission phases

Table 2.1 lists the main facts about the S/C and its orbit. The Highly Elliptical Orbit was chosen as a compromise between the energy needed to launch the satellites and the distance from Earth that could be reached.
The inclination (59°) has been selected in order to minimize the radiation dose received due to the periodical crossing of the Van Allen radiations belts surrounding Earth.

2.2.1 Early mission phase

The two spacecrafts will be launched with the OSC stacked on the CSC who is, in turn, joined to the launcher (see Figure 2.2). After deployment, the two jointed spacecrafts will be parked in a Low Earth Orbit (LEOP phase) for two days and then sent in the HEO where the attitude will be such that both CSC and OSC sun panels will point to Sun. A simplified scheme of the phases progression is shown in Figure 2.1. Figure 2.3, instead, illustrates the different operations that occur during a nominal orbit.
For about one month no formation flying will be attempted and preliminary commissioning will be performed on the metrology systems and the scientific instruments. In this phase, OSC is passive and the movements are governed by CSC.

After separation, the two satellites are put on a safe relative orbit, their attitudes continue to be Sun-pointing, but separately. Commissioning and calibration activities of the formation flying metrologies and GNC can begin.

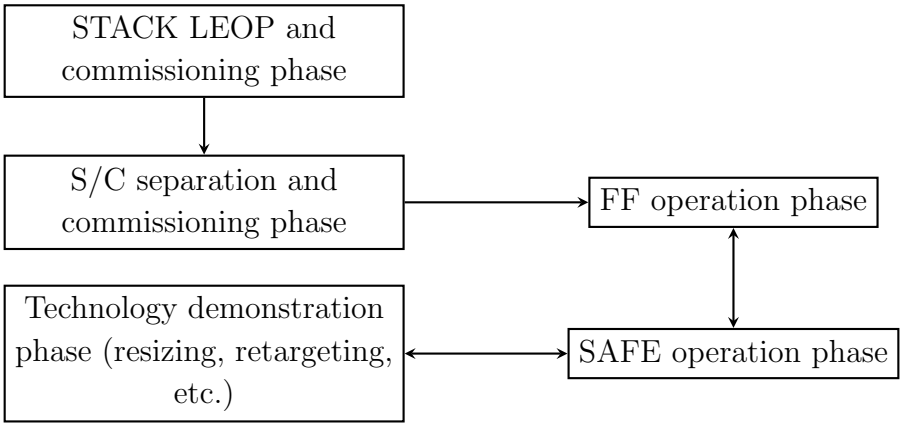

Figure 2.1: PROBA-3 mission phases

In order to commission laser (FLLS) and visual-based (VBS) metrological systems, the two spacecraft will be directed to point one another.

The very first formation flying acquisition with GNC in closed-loop will be performed without SPS. After the calibration of the alignment between Star Trackers and laser-based metrology (FLLS), the calibration of the penumbra profile and the update of the on board parameters, the GNC will use the laser metrology and CSC and OSC Star Trackers to control the formation up to nominal station-keeping geometry. Only after the two satellites will have reached a relative positioning such that the SPS is within its operational range, SPS will be used for formation control in closed-loop.

ASPIICS is equipped with a front door that prevents the full Sun intrusion into the Coronagraph Instrument, it is normally closed except when PROBA-3 is in observation mode. Once the formation control is achieved, the door will be safely opened in the shadow for the first time. During the first orbit with the door opened the SPS (and the alignment between Star Trackers and FLLS) can be further calibrated.

2.2.2 Nominal mission phase

Nominal station-keeping at apogee for coronagraphy

During nominal operation for coronagraphy and formation flying maneuvers the two satellites relative orbit is actively controlled:

- The two satellites are co-aligned and the common reference frame is

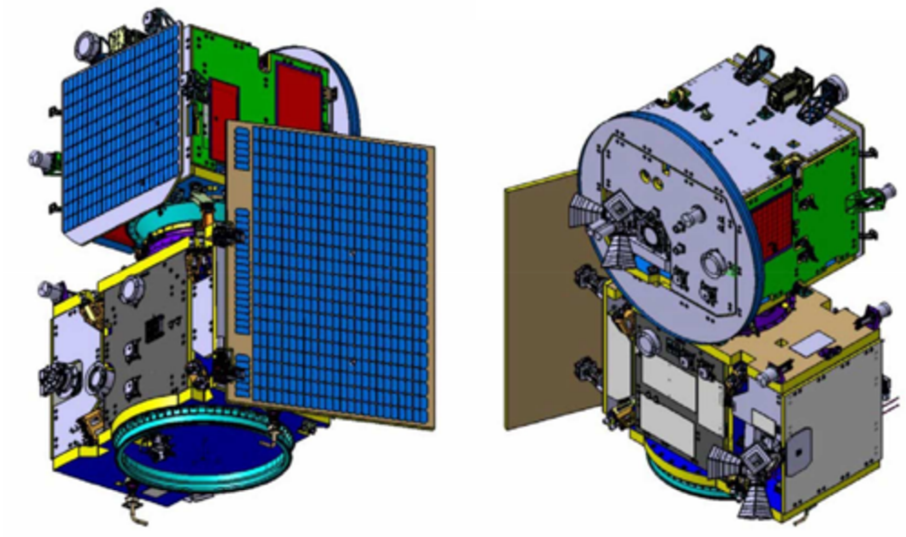

Figure 2.2: The two satellites composing PROBA-3 in stacked configuration.

pointed to Sun.

- The distance between the satellites is adjusted.

DTM Direct Transfer Maneuvers

During an operational orbit, two impulsive *Direct Transfer Maneuvers,* ΔV, are applied, at the beginning and at the end of the perigee passage, firing the 1 N monopropellant propulsion system incorporated in the coronagraph satellite CSC (see Figure 2.3).

DTM#1: formation separation maneuver for collision avoidance purpose.

DTM#2: maneuver to stop relative drift between S/C after perigee pass and to set the formation acquisition phase.

Formation acquisition

After DTM#2, the Guidance and Navigation Control system begins to drive the formation-flying acquisition using the different metrology systems in sequence in an *incremental* fashion, meaning: from the less precise (and longer range) to the more accurate ones (see Section 2.5); the measurements taken with the next system are normally used to calibrate the previous one.

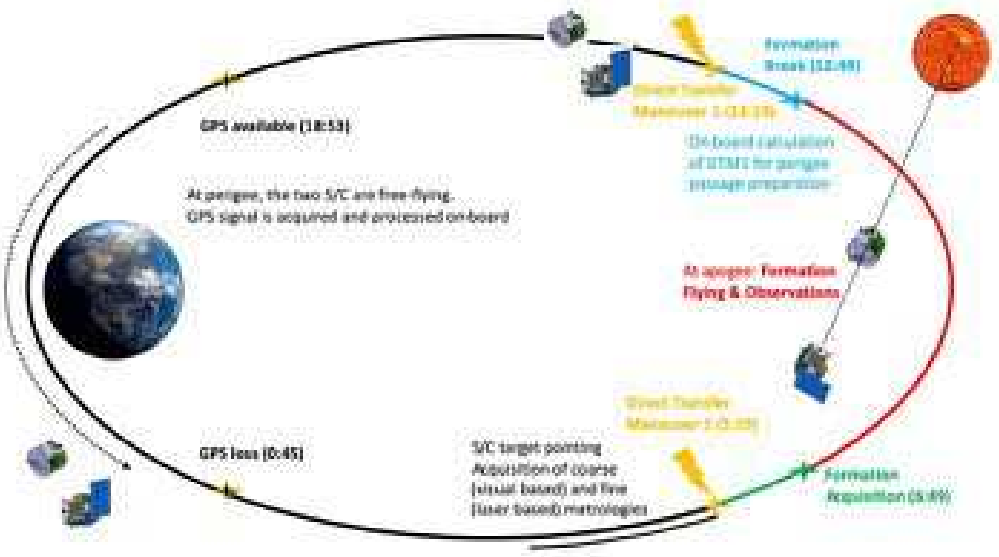

Figure 2.3: Description of the different steps taking place during an orbit.

During the formation acquisition and station-keeping phases, the CSC is free-flying with a Sun-pointing attitude and the relative movement is in charge of the OSC only, controlled by the fine 10 mN cold gas propulsion. In this case the OSC is the *chaser* and CSC represents the *target*.
During these phases, GNC uses all the metrologies to control the formation up to nominal station-keeping configuration bringing SPS within its operational range; at this point the SPS can be used for position control in closed-loop. When the SPS returns a safe position, the front door can be securely opened in the shadow.

Formation breaking

After the apogee arc, and after the observation or formation-flying activities, the CSC thrusters are fired to apply an impulsive ΔV to break the formation and place the two satellites on a safe passive orbit lasting all the perigee pass. The direction and magnitude of the separation ΔV needed for separation are

not constant from one orbit to another and depend on the relative trajectory required for the perigee passage.

2.2.3 Formation flying demonstration maneuvers

In addition to station-keeping for coronagraphy science, additional types of maneuvers are scheduled during the apogee passage having the purpose of demonstrating formation-flying capabilities:

1. Resizing: with both satellites aligned in the Sun direction, the Inter-Satellite Distance (ISD) is changed in the range 30-250 m.
2. Retargeting: with both satellites aligned, the formation is rigidly rotated up to a maximum of 30° about the Y axis.
3. Combination of resizing and retargeting.
4. 180° roll, with both satellites aligned in Sun direction, the OSC is rotated about the X axis.

2.2.4 Safe relative orbit

The orbital parameters (position and velocity) of the two spacecraft must comply to different and competing needs:

1. The two spacecrafts must not be too separated to minimize the need of ΔV maneuvers and, consequently, the energy necessary to return to the nominal operational orbit.
2. It must be absolutely avoided the risk of collision, keeping a minimum distance between the spacecrafts (tipically 250-500 m), when free-flying.

The two spacecrafts travel the safe relative orbit during commissioning phase (just after spacecraft separation) but also in case of failure, for safety reasons, or survival during long eclipse periods. In fact, the mission is subject to periods of eclipses given by Earth interposing between PROBA-3 and the Sun. There are two types of eclipses:

Long: with a season lasting about 15 days, in which the eclipse duration is more than 3 hours and observations are not feasible;

Short: with a duration of about 30 minutes during which normal operations can continue.

During long eclipses the spacecrafts are put in safe orbit and no formation-flying activity is performed.

2.3 Environment

The environments considered [49] for PROBA-3 mission include:

1. Solar and planetary electromagnetic (EM) radiation
2. Plasmas
3. Energetic particles radiation
4. Particulates and molecolar contamination

The PROBA-3 spacecraft will receive electromagnetic radiation from three primary sources: the direct solar flux, Earth albedo and Earth infrared (IR) radiation, the biggest contribution coming from the direct solar flux summing up to about $1366\,\mathrm{W\,m^{-2}}$ (solar constant at 1 AU).
The albedo is the fraction of solar radiation that is reflected by a planet (in this case, the Earth) and in average it is 0.3 but with huge variations due to e.g. cloud coverage. The total varies also as a function of the illuminated fraction seen by the SPS sensors through their field of view of $21^\circ \times 21^\circ$. The albedo contribution to various PROBA-3 subsystems has been thoroughly investigated in [44] (maximum $1.73\,\mathrm{W/m^2}$ for an ASPIICS band-pass of 30 nm) and it can be extrapolated to about $9\,\mathrm{W/m^2}$ for SPS (band-pass of 160 nm). The effect on SPS system is negligible for lateral displacements (same effect on all sensors), and minimal for the longitudinal error (included in the error budget [32]).
The infrared part is calculated considering the Earth as a 288 K *Black Body*; the average IR radiation emitted is $230\,\mathrm{W\,m^{-2}}$, but, being out-of-band with respect to the band-pass filter (500-660 nm), it has no effect.

The plasma affects in particular high-voltage devices and communication systems (radio etc.). SPS electronics is enclosed in a metallic flange and communicates digitally by wires, so the only concern could be for the possibility of external surfaces (chassis) charging and the consequent harmful electrostatic discharges (ESD). SPS electronics is compliant with the general

prescriptions about ESD immunity and follows the S/C grounding scheme described in Section 5.2.

Concerning space radiation, the SPS is placed outside the Service Module (SVM) so the spacecraft structure does not provide any shielding from it. The only protection against radiation for the SPS electronics consists in the metal walls of the mechanical flange whose thickness is detailed in Table 6.2. In the Requirement Specification document [50] they are listed: Total Integrated Dose, Proton fluence equivalence for Non-Ionising Energy Loss (NIEL) in Si material and Displacement Damage Dose. The relevant values, applicable for Aluminium shielding thicknesses from 3 to 5 mm, are extracted and summarized in Table 2.2.

Thickness (mm)	TID [krad]	p fluence [$\#/cm^2$]	DDD [MeV/g(Si)]
3	65.00	2.07E+10	1.286E+8
4	26.46	1.42E+10	9.288E+7
5	12.08	1.08E+10	7.195E+7

Table 2.2: PROBA-3 Total Integrated Dose, 10 MeV proton fluence and displacement damage dose for different thicknesses of Al.

We consider the SPS-PCB as surrounded by an average 4 mm thickness of Aluminium. All SPS components are space-qualified and rad-hard at least at the level of 43 krad.

Finally, concerning particulates and molecular contamination, it must be considered that the sensor active surface is protected by a rad-hard glass and that SPS is hosted in a flange. The flange is pierced by eight pinholes, four of which (set A) are covered by neutral density filters most of the time, while the others are uncovered also when the front door is closed (see Figures 3.7). The internal production of contaminants is limited by cleanliness control procedures and avoiding the use of outgassing materials. Concerning external deposition, in [44] it is estimated a molecular deposition of 30 Å per year, a quantity that is not harmful for the optical properties of SPS.

2.4 Observation of the solar corona

The main scientific task of PROBA-3 is to observe the solar corona in visible light (VL), by means of the instrument ASPIICS.

The solar corona is composed mainly of ionized plasma permeated by magnetic fields. Despite the difficulties in its observation, Sun corona deserves this effort because this is the region where most energetic phenomena like CME (Coronal Mass Ejections) and solar flares originate and where the temperature raises from the 5770 K of the Sun surface to million degrees. The physical parameters involved: plasma density and temperature, magnetic field etc. require observations with high resolution at different wavelengths and, possibly, in conjunction with other space and ground based observatories.

Figure 2.4: The solar corona as imaged during the 2010 total solar eclipse.

2.4.1 Coronagraphs

On Earth, the optimal situation for observing the solar corona is during a total solar eclipse, an event extremely rare, that takes place in different geographical locations (often difficult to reach), subject to meteorological conditions, and of short duration (see Figure 2.4).

The coronagraph, invented by the French astronomer Bernard Lyot in 1939 [24] [25], has been used since then to observe the solar corona at any

time. The original design consists of a telescope equipped with an opaque disk (internal occulter), placed on the focal plane of the primary objective, whose purpose is to block the light from the Sun disk.
In order to bring the stray light below the level of the coronal signal, the coronagraph needs to remove the light diffracted by the edge of the entrance pupil (in Lyot coronagraph, the edge of the primary objective lens) by means of the *Lyot stop* that blocks internally the image of the edge.
Nevertheless, ground based coronagraphs are limited by the brightness of the sky, which overwhelms the coronal signal.

The solar corona is made of plasma heated at million degree temperatures, emitting radiation in the UV and in the X wavelength band.

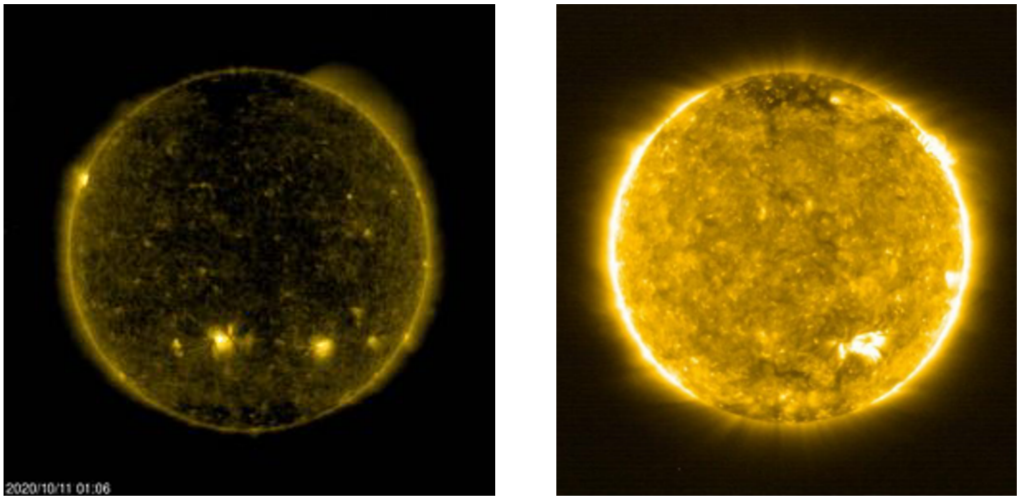

Figure 2.5: Left: SOHO EIT instrument observations in the Fe XV 28.4 nm line. Right: Solar Orbiter EUI observation in the Fe IX and Fe X line blend at 17.4 nm.

EUV and X solar disk imagers and spectrographs, although able to operate only from space, provide the best way to study the base of the corona, as seen from the Solar Orbiter/EUI images of Figure 2.5. In order to explore the extended corona, instead, a coronagraph is needed.

An improvement of the Lyot coronagraph is given by the externally occulted coronagraph. This configuration has an external occulter disk that shadows the primary objective from the solar disk radiation, allowing to observe the fainter outer corona. Most of the space coronagraph are of this kind (UVCS, LASCO C2 and C3 [4] on SOHO, SECCHI on STEREO, etc.). With reference to Figure 2.6, the external occulter O blocks the light coming

from the Sun disk and lets the coronal light to pass around and enter the coronagraph pupil defined by the primary objective on the plane A.
The primary objective (L1) forms an image of the external occulter onto the internal occulter, O', usually cemented on the secondary objective (L2). The internal occulter blocks the image of the edge of the external occulter. It is slightly oversized to take into account optical aberrations, errors in mechanical positioning and stability.
The secondary objective, L2, images the entrance pupil on the *Lyot Stop*, C, that blocks the light diffracted by the edges of the pupil.
Finally, the coronal image is formed by the relay lens, L3, onto the detector plane (D).

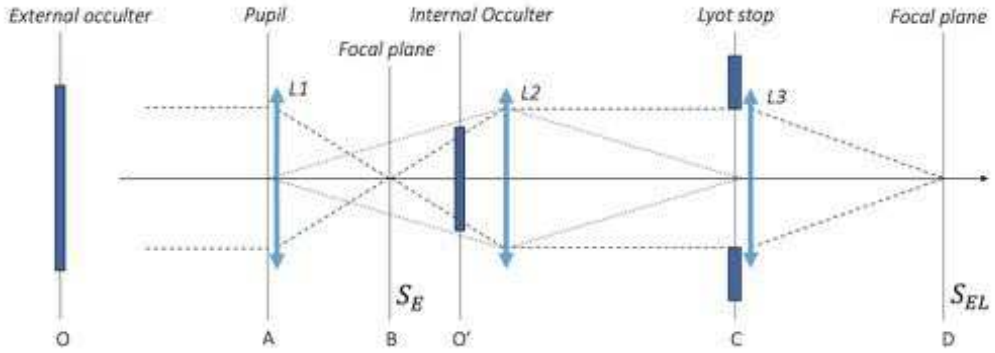

Figure 2.6: Externally occulted Lyot coronagraph scheme. See text for the description. The figure is not to scale. [45]

2.4.2 Space Coronagraphs: field of view

Externally occulted coronagraphs are used in space to observe the outer corona. This type of telescope suffers from the vignetting of the inner field of view that strongly limits the capability of the instrument to observe close to the limb, creating an unobserved gap between the FOVs of disk imagers and of the coronagraph (see Figure 2.7). An improvement in the extension of the lower end of the field of view is the extension of the distance between the telescope and the external occulter. Pushing this distance to the limit, a result similar to the solar total eclipse is obtained, where the Moon acts as external occulter. A comparison of the FOV lower limit reached by different coronagraphs is shown in Figure 2.8).

A large improvement on this limit is introduced by ASPIICS with its ISD of the order of 150 m.

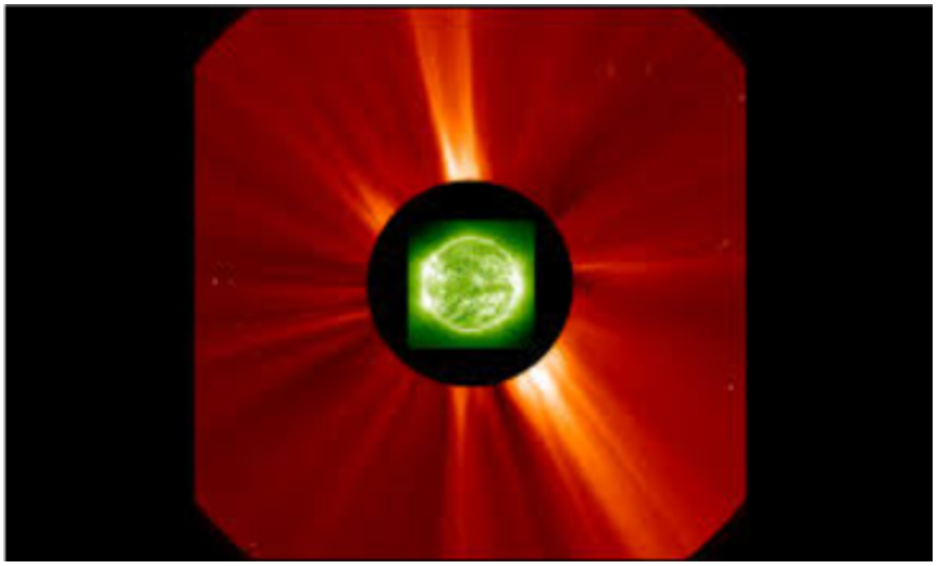

Figure 2.7: Superposition of the image from SOHO EIT and LASCO C2 showing the gap in observations between a EUV imager and a coronagraph.

2.4.3 ASPIICS

ASPIICS is a visible-light space-based coronagraph built by a consortium led by CSL (Centre Spatial de Liège, Belgium) and including more than twenty scientific and/or industrial partners from several European countries: Belgium, Czech Republic, Greece, Ireland, Italy, Poland and Romania.

The Work Breakdown Structure (WBS) [48] lists all work packages and assigns the responsibility of producing the SPS electronics to SensL (Ireland) and the SPS engineering, integration and testing activities to INAF (Italy). The SPS electronics project management competes to CSL. Another relevant partner is CBK (Poland) for the CCB (Coronagraph Control Box) system interfacing with SPS. Finally, the future ASPIICS calibrations with Sun Simulator, comprising also SPS metrology calibrations are under the responsibility of INAF.

The ASPIICS scientific objective is to investigate the physical processes taking place in the solar corona. Several important problems in solar physics

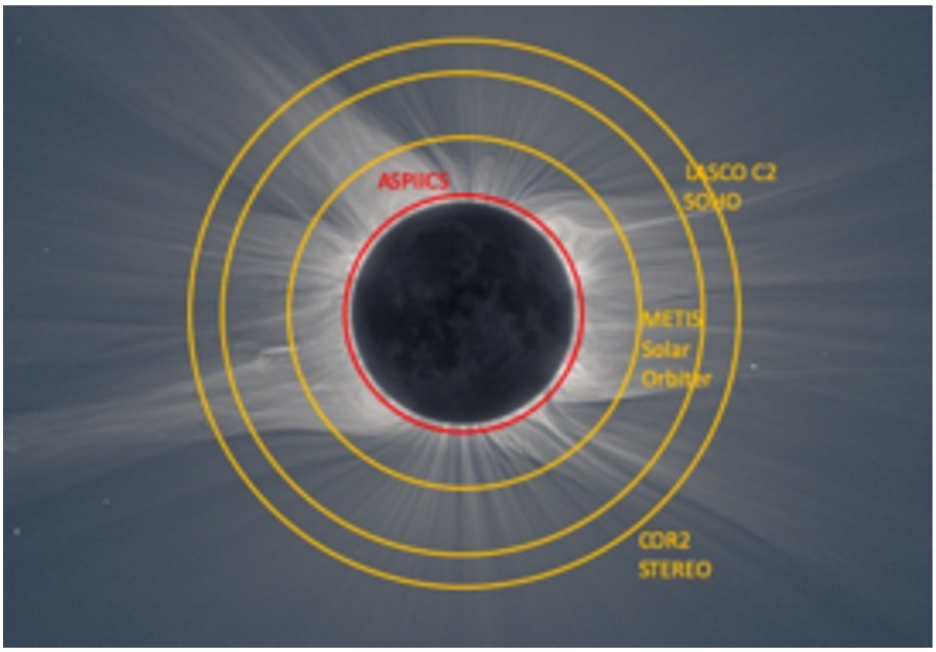

Figure 2.8: Comparison between the minimum distance reached by different space-based coronagraphers in terms of $R_{\odot}$.

could be faced using PROBA-3/ASPIICS observations. These will provide important information on the structure of the coronal magnetic field and therefore to the modeling of the sources of solar wind and of the interplanetary magnetic field:

- What processes contribute to the heating of the corona and to the solar wind acceleration.
- What is the nature of the coronal structures that form the Coronal Mass Ejections and how they are generated and accelerated in the low corona.

ASPIICS, with its 144-146 m distance between the 1.42 m External Occulter, mounted on the OSC S/C and the Coronagraph Instrument, mounted on the CSC S/C, will be capable to cover the gap between the observations made by EUV imagers and the ones made in VL by the externally occulted coronagraphs, reaching an inner field of view edge of 1.08 $R_{\odot}$. ASPIICS coronagraph has an entrance pupil of 50 mm and provides images of the solar corona between 1.2 and 3 solar radii in the following wavelength bands:

- Wide (535-565 nm) white-light ("orange") passband containing essentially the coronal continuum produced by the Thomson scattering.
- Wide white-light passband combined with 3 polarizers oriented at angles of 0°, 60°, 120°.
- Narrow (0.6 nm) passband centered at 530.4 nm (coronal green line of Fe XIV + coronal continuum).
- Narrow (2.0 nm) passband centered at 587.7 nm (prominence line of He I D3 + coronal and prominence continuum).

The characteristics of the PROBA-3 mission and in particular its dual nature, technological and scientific will pose anyway limits to ASPIICS performance; in fact, ASPIICS will be not able to provide a continuous monitoring of CMEs due to:

- Duty cycle: 6 hours of coronagraphic observations out of 19 h 38 min of orbit duration; not all the orbits are dedicated to the solar science.
- Data latency: downlink of the science data is not guaranteed during every orbit.
- Small field of view: most of the halo CMEs are not yet completely developed at 3 $R_{\odot}$, and the CME acceleration is often still ongoing at these distances.

2.5 Metrology subsystems

PROBA-3 will use, in sequence, several metrology subsystems to reach the desired absolute and relative positions and attitudes of the two spacecrafts. The metrology systems involved in precise formation flying are listed in Table 2.3 with an indication of the spacecraft on which the elements are distributed. GNC will exploit classical sensors such as star trackers (STR) sun sensors and gyroscopes, for absolute attitude control of both spacecrafts.

Critical space systems are usually built with internal hardware duplicate (Redundant) so to provide a backup solution in case of failure of the principal (Nominal) component.

Item	CSC	OSC
Formation Flying units		
OPSE (Occulter Position Sensor Emitters)	ASPIICS detector	3× LED (N+R)
FLLS (Fine Lateral and Longitudinal Sensors)	Corner cube	Optical Head Unit (Sensors and laser emitters)
SPS (Shadow Position Sensors)	4× SiPM (2 sets)	Sun + Occulter ($\varnothing$=1.4 m)
VBS (Visual Based Sensors)	8× IR LED (N+R)	Wide-Area & + Narrow-Area Cameras (N+R)
ISL (Inter Satellite Link) RF S-band	Rx-Tx + antenna	Rx-Tx + antenna
GNC units		
Star trackers	3× Optical Heads + electronics	3× Optical Heads + electronics
3-axis rate-sensors	2× gyroscopes	3× gyroscopes
Sun Sensors	5× (1 Fine and 4 Coarse) redundant cosine sensors	5×
GPS	Receiver + antenna	Receiver + antenna
Actuators		
Propulsion Thrusters	$2 \times 8 \times 1\,N$ Monopropellant	$2 \times 12 \times 10\,mN$ Cold gas
Reaction Wheels	Pyramid of 4 units	Pyramid of 4 units

Table 2.3: PROBA-3 Formation-Flying metrology systems, sensors and actuators.

Concerning the actuators, each S/C is stabilized by means of four reaction wheels, oriented in space as the sides of a pyramid in order to optimally distribute three-dimensional torque.

For the movement, instead, OSC is equipped with precision 10 mN cold-gas thrusters while CSC is controlled by 1 N monopropellant thrusters for generating Direct Transfer Maneuvers and, in case, put in action collision-avoidance maneuvers.

The Inter-Satellite link (ISL) connects the two spacecrafts, allowing the data exchange and the range measurements, up to a few km. ISL is capable of recovering also from *lost-in-space* situations.

At perigee passage, near the Earth, both satellites enter in the visibility range of GPS (Global Positioning System) signal and this information is used to calculate and forecast the relative positions and velocities at DTM#2, where GPS signal is not available.
During the rest of the orbit PROBA-3 is able to operate GNC controls and Formation-Flight activities in full autonomy; this capability to operate autonomously can be prolonged for a week or more.

During the Formation Acquisition phase, attitudes and relative positions are accurately measured using: visual-based sensor (VBS), the OPSE (a pattern of LED imaged on the CI camera) and, finally, by the fine laser-based metrology (FLLS) and SPS.

The Occulter Disk Position Sensor (OPSE) is under the responsibility of INAF and is composed by three light emitting LED, placed on the anti-Sun face of the Occulter disk, that are imaged by the CI detector and whose output is processed by on-ground post processing to obtain an estimate of in-flight geometry.

The OPSE can be used:

- During coronagraphy station-keeping in conjunction with SPS, providing a more accurate estimate of the instrument's pointing.

- In resizing maneuvers: if the CSC position is not provided by the SPS, OPSE can help to estimate the instrument position along the target line to calibrate the alignment between FLLS and OSC Star Trackers.

2.5.1 SPS - Shadow Position Sensors

Shadow Position Sensors[1] is the last metrology system to intervene in the GNC loop and the most accurate between them. It is based on the continuous measurement (with a 2 Hz readout cadence) of the penumbra profile around the nominal position and on its fitting with a model of the light expected behind the occulter. The 3-D actual positioning of the center of the entrance pupil of the telescope, placed on the Coronagraph S/C, is calculated with respect to its nominal position i.e. the umbra center at the nominal ISD (Inter-Satellite Distance, defined in Section 2.6.2).

SPS consists of eight Silicon Photomultipliers (SiPM), divided in two independent sets, placed on a circular PCB, at a constant distance of 55 mm from the center of the coronagraph entrance pupil diaphragm. All signals are amplified and digitized on the PCB itself feeding an on-board algorithm that translates the digital values in absolute 3-D displacements with respect to the nominal position.

A two-stage electronics (see Figure 5.4) converts the photo-current generated by each SiPM in a voltage that is digitized by a 12-bit ADC. The second stage amplifier is used to improve the sensitivity in the lower light range. More details on the final design are given in Chapter 5.

The difference between opposite sensors measurements is obviously related to the direction and to the amount of displacement from the ideal position. But, in order to translate them in absolute displacement measurements with the desired performance, these values are fitted [9] [10] to a third-order pseudo-paraboloid with the axis of symmetry parallel to the optical axis. This metrology algorithm converts the digital readouts into three spatial coordinates stating how the origin of the reference frame moved from its nominal position.

When the door lid is closed, the nominal set of photodiodes (1/3/5/7) are covered by a filter (Optical Density 2, placed on the door lid) attenuating the Sun light of a factor 1/100, such that also in full Sun the electronics can work within its dynamic range. When the door is open, these photodiodes saturate if they are too far from the shadow central line (at least 125 mm distance from the shadow center, or 70 mm off from the nominal coronagraph position

[1] This description of SPS has been published as part of "Metrology on-board PROBA-3: The Shadow Position Sensors subsystem" in *Advances in Space Research - Special Issue on Satellite Constellations and Formation Flying* [36].

plus a considerable margin). The redundant SPS photodiodes (2/4/6/8) are not covered by a light attenuator so that they can correctly measure the light irradiance up to at least 125 mm from the shadow center, independently of the status (open or closed) of the door lid. It is expected that there will be a small overlap between the lateral range of covered and uncovered photodiodes. That is, at 120/125 mm from the shadow, a photodiode covered by the light attenuator receives an irradiance above its minimum measurement threshold, and a photodiode not covered receives an irradiance below its saturation limit.

When in station-keeping for coronagraphy, the SPS is able to provide direct (real time) measurement of the umbra axis direction. The SPS will be switched on at least one and half hours before the beginning of observation period in which formation maneuvers take place.

2.6 GNC - *Guidance and Navigation Control system*

2.6.1 Reference frames

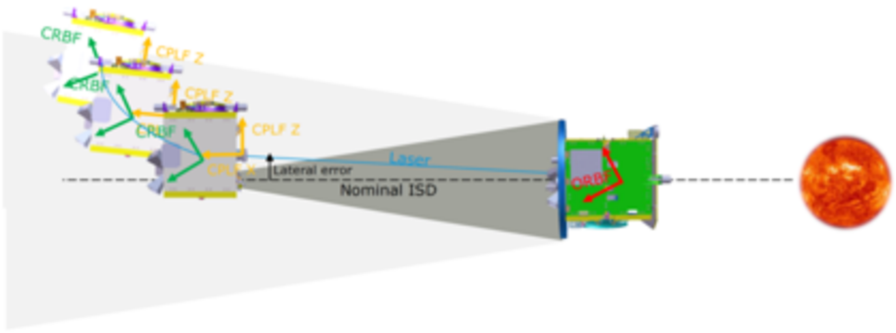

Figure 2.9: Position acquisition sequence using metrology control loop (Courtesy of ESA). OPLF is joint to OSC and it is not shown.

PROBA-3 is a complex system consisting of two independent spacecraft and relative subsystems, then, there is the need to define multiple reference systems that are described in Table 2.4.

In Figure 2.9 it is shown the progressive reaching of the nominal position with the alignment of CPLF with OPLF in direction of the Sun.

CPLF	*Coronagraph P/L Frame*; it is the main ASPIICS frame, to be precisely positioned and oriented during station-keeping. Its X axis corresponds to the coronagraph optical axis and is defined as the line joining the center of the primary objective and the center of the internal occulter, pointing in direction opposed to Sun.
STF	*Sun Target Frame*; the origin is the center of the occulter disk, the X axis points nominally from the Sun to the origin and the Z axis is along the ecliptic plane angular moment. The Y axis completes the triad.
FRF	*Formation Reference Frame*; its origin coincides with the CSC Center of Mass; it must be co-aligned with STF during Coronagraphy station-keeping.
OPLF	*Occulter P/L Frame*; the origin is the center of the occulter disk, on the anti-Sun surface of the disk panel, the X axis is normal to the disk, pointing towards anti-Sun and Y,Z axis are on the disk plane.
CRBF and ORBF	*CSC and OSC Rotating Body Frames*; having origin in CSC and OSC Centers of Mass. The orientation is fixed to the S/C structures.

Table 2.4: PROBA-3 reference frames definitions.

2.6.2 Nominal Inter-Satellite distance

The nominal Inter-Satellite Distance (ISD) is the distance between the origins of the Occulter Disk (OPLF) and of the Coronagraph (CPLF) frames, provided that the OPLF origin is on the X axis of the STF (Sun Target Frame).

For a proper operation, the image of the EO disk (overoccultation 1.02 $R_\odot$) must be fully contained by the IO (1.08 $R_\odot$), then, the Coronagraph Instrument must be at the distance $ISD = (R_D - r_p)/\tan(1.02\,\vartheta_{sun})$ where:

- R_D is the occulter disk radius (0.71 m)
- r_p is the entrance pupil radius (25 mm)
- $\vartheta_{sun} \approx R_{sun}/1AU$ is the Sun disk apparent angular dimension (about 0.0046524 radians), seasonally changing
- 1.02 is the overoccultation factor

The nominal ISD varies with the season (different Earth-to-Sun distances) and is constantly recomputed on board. Its value is $(144.5 \pm 2.4)\, m$.

The shadow radius can be computed as a function of the ISD and it is in average:

$$R_{shad} = R_D - ISD \times \tan(\vartheta_{sun}) = 38.43\, mm$$

.

2.6.3 Formation acquisition

During station-keeping the GNC control operates in this way:

- The guidance functions compute the target position of the OSC (origin of OPLF reference frame, see Section 2.6.1, with respect to the CPLF origin in the FRF and of the laser beam with respect to the retro-reflector.
- Furthermore, they calculate the final inertial orientation of ORBF and CRBF (which, during coronagraphy station-keeping, must be such that the CPLF points to the Sun).
- The navigation functions estimate the actual values of these coordinates using the available sensors (visual based, laser, star trackers, etc.) with or without SPS.
- The controller tries to nullify the difference navigation - guidance, using only the CSC and OSC reaction wheels and the OSC cold gas thrusters.

The attitude control is performed on both spacecraft at a frequency of 4 Hz, 40 times faster than the position control (at 0.1 Hz, on OSC only) minimizing possible problems of dynamic coupling between attitude and position errors.

2.6.4 Formation performance

The formation stability, as prescribed by PROBA-3 Science Requirements, is such that:

- The absolute pointing stability over 6 hours shall be better than 10 arcsec (SPR-17)

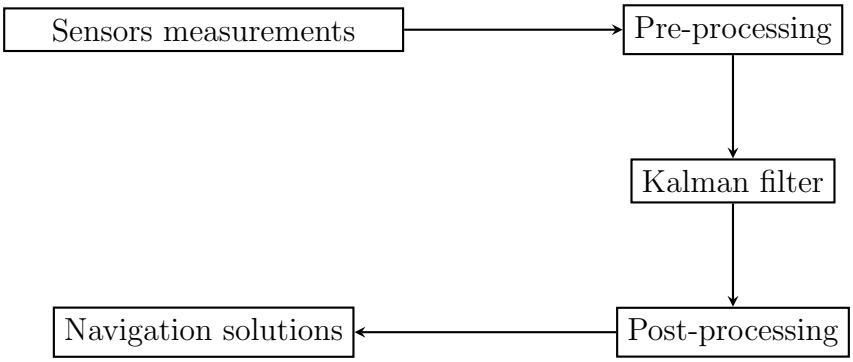

Figure 2.10: PROBA-3 GNC process.

- The absolute pointing stability over exposure time < 10 sec shall be better than 2.5 arcsec (2σ) (SPR-18) with a goal of 1.4 arcsec (SPGR-11)

To meet the Coronagraph scientific performance requirements, the PROBA-3 must be able to hold formation such that the lateral and longitudinal errors fall within a region shaped as a double cone (2× RDEx long and 2× RDEy or RDEz wide) so that the occultation remains within a range [1.01 - 1.03] during the 6 hours of station-keeping.

Table 2.5 summarizes the pointing and positioning requirements.

Requirement	Value
Absolute Attitude Pointing	7.1 arcsec
Absolute Attitude Pointing stability (10 s)	2.6 arcsec
Relative displacement lateral error @ 40 m distance	2.2 mm
Relative displacement lateral error @ 150 m distance	4.9 mm
Relative displacement lateral error @ 250 m distance	8.1 mm
Relative displacement longitudinal error	14.8 mm
Relative velocity error	0.15 mm/ sec

Table 2.5: The attitude and relative displacement maximum errors.

The expected lateral position error (combination of RDEy and RDEz) is about 10 mm using FLLS only (SPS used only for calibration at commissioning) and 1-2 mm with SPS in closed-loop (assuming 0.5 mm SPS error).

2.6.5 SPS as a subsystem of ASPIICS

SPS is a subsystem of the coronagraph ASPIICS, that is composed of the External Occulter (including OPSE, hosted on its anti-Sun surface) and of the Coronagraph Instrument (CI) (see scheme 2.11). The CI is mounted on the CSC optical bench and consists of:

1. Coronagraph Optical Box (COB), a tube holding the Front Door Assembly (FDA), hosting the SPS in the front flange and containing the ASPIICS optics and the Filter Wheel Assembly. The rear part interfaces with the Focal Plane Assembly (FPA). COB is held in position on the optical bench by two monopods in front and two bipods in the back (see Figure 1.3).
2. Camera Electronics Box (CEB) containing the electronics interfacing with the FPA.
3. Coronagraph Control Box (CCB) containing the Power Conversion Unit (PCU), the Data Processing Unit and the Auxiliary Equipment Unit. An FPGA, internal to CCB, interfaces with SPS.

The following coronagraph requirement defines the SPS operation and the expected functionalities. ADPMS is the Advanced Data and Power Management System (the spacecraft on-board computer).

Req. ID	Req. Text	Verif. Method(s)
COR-7197	The CCB shall drive the SPS and read out the SPS data at least at 2 Hz. (...) The CCB shall transmit the calculated position results, photodiode raw data and validity flag to the Spacecraft ADPMS. Upon reception of the corresponding telecommand from the ADPMS, the SPS data shall be delivered as Housekeeping telemetry in less than 100 ms. Note: the position estimator algorithm shall be provided by the SPS Developer to the CCB Developer.	D, T

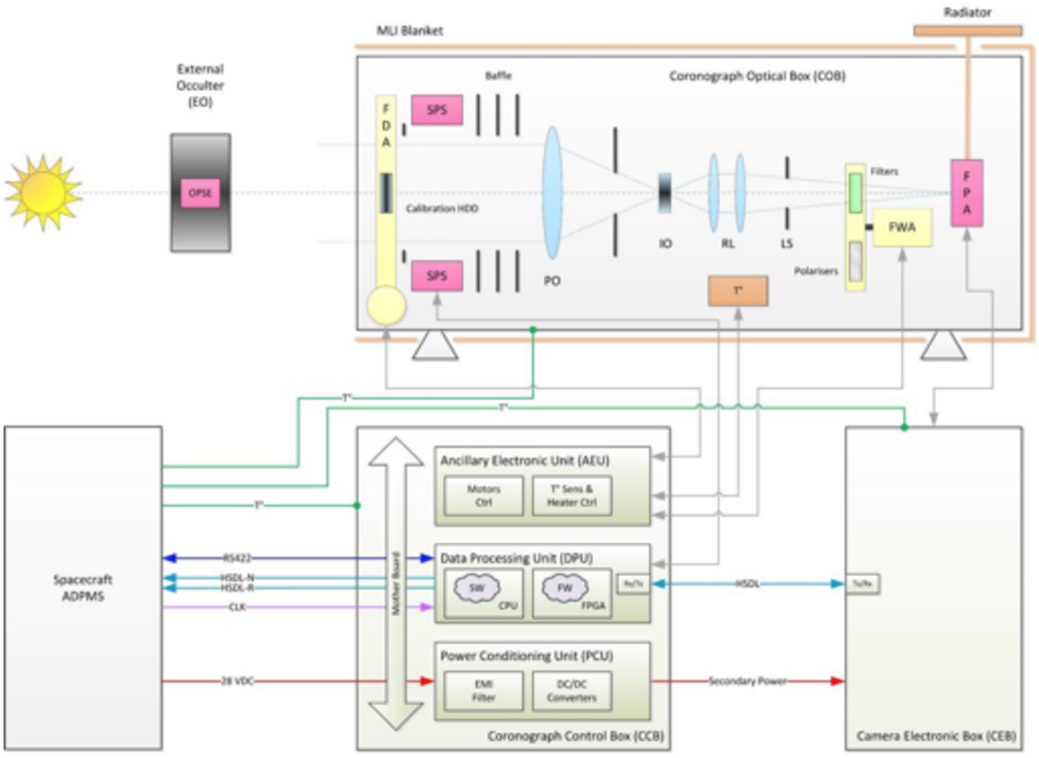

Figure 2.11: ASPIICS instrument block diagram.

Chapter 3

SPS and the shadow sensing algorithm

In this chapter we introduce the SPS working principle and the algorithms used to reconstruct the coronagraph satellite position. We explain also how the SPS electronics fulfills the requirements stated in several ESA and CSL documents. Starting from an ESA general system requirement document [40], more specific requirements were defined in the ASPIICS coronagraph Instrument Interface Document [41]. Then, these were flown down, as depicted in scheme 3.1, by CSL into two documents [42] and [50] specific for the coronagraph and for the SPS. Both documents are applicable to our case. The requirements are uniquely identified by an abbreviation and 3 or 4 digits as schemed in Figure 3.1.

The verification of these SPS requirements must be accomplished by one or more of the verification methods foreseen by ECSS-E-ST-10-02C standard:

T	Test (including demonstration);
A	Analysis (including similarity);
D	Design review;
I	Inspection.

3.1 Introduction

The need of a system of sensors surrounding the coronagraph aperture stems from the following "coronagraph design and accommodation requirement" [40]:

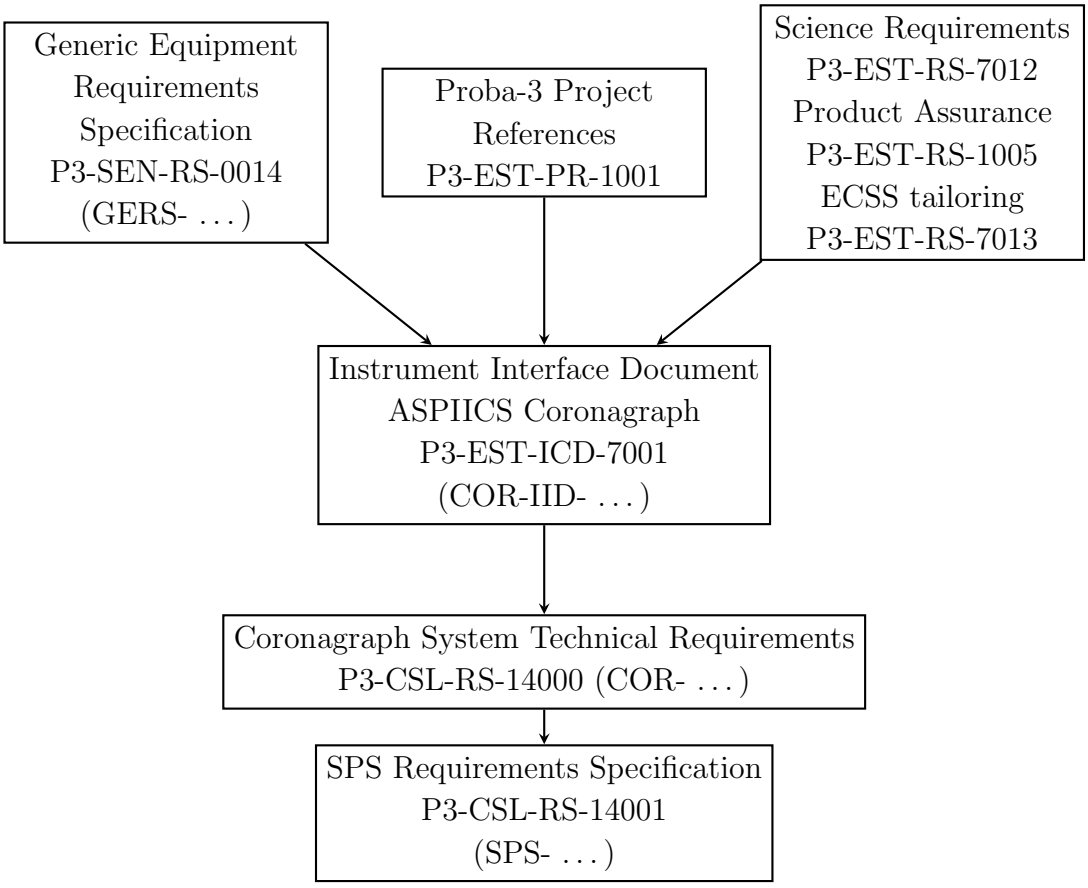

Figure 3.1: *Flow-down* of the SPS relevant requirements documentation.

CO-31-R	A Shadow Position Sensor (SPS) shall be used to verify that the Coronagraph Instrument entrance pupil is centered within the shadow cone of the occulting disk.

This requirement is quite generic and does not specify the precision of this verification. More details on the performance are contained in two ASPIICS requirements that are extensively treated in Sections 3.3.2 and 3.3.3.

3.1.1 SPS position and placement

At the end of the bridging phase (phase B, see Section 4.1.1) it was planned that the eight SPS sensors should be distributed onto two concentric circles with radii 45 and 52 mm. Afterwards, based on thorough trade-off studies

[14], it was decided to place the sensors on a single circular crown at 55 mm from the center of the entrance pupil of the coronagraph instrument, see Figure 3.2.

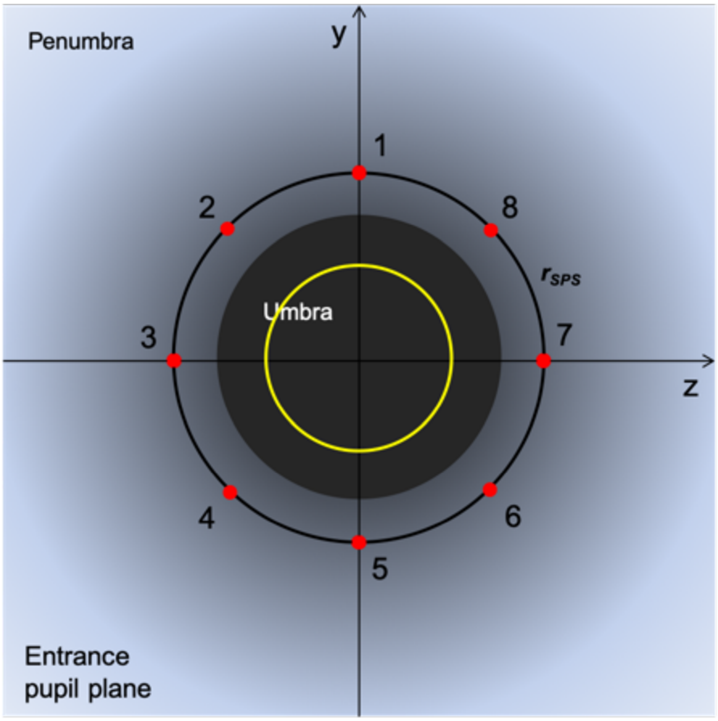

Figure 3.2: Definitive positioning of the eight SPS (red dots). The yellow circle indicates the pupil diaphragm.

The eight sensors belong to two different sets: A (1-3-5-7) and B (2-4-6-8). The A set is the one normally used and gives directly the offset along y and z axes, while the B set requires a 45° rotation.

3.1.2 Sensor type and characteristics

The sensors used are SiPM (Silicon Photo-Multipliers) model MicroFC-30035-X05 produced by SensL (an Irish company afterwards absorbed by ON-Semi), are $3\,mm \times 3\,mm$ square arrays of 4774 (77×62) 35 µm resistor-coupled diodes (see Figure 3.3) enclosed in a TO-5 case shown in Figure 3.4. These photomultipliers are based on a commercial product [19] realized using an established CMOS process. The same company has been in charge of

manufacturing the SPS readout electronics for all the models and the EGSE (Electrical Ground Support Equipment).

The main difference between the type of sensor adopted by SPS and a classical, large collecting area, photodiode is that these array-based sensors are composed of thousands of microcells, thus being more reliable because any open-circuit damage induced by radiation will affect only individual diodes, while short-circuit effects are limited by the presence of the current limiting resistors (see Figure 3.3).
Given the large dynamic interval of light that must be sensed, the sensors, usually operated in "Geiger mode" (thus biased exceeding the threshold voltage, a configuration more suitable for low light level sensing), are used by the SPS in "zero bias mode", that is with the anode directly tied to ground. In this configuration the sensor has a lower responsivity, but its response is much more linear with the incoming light intensity.

One of the main issues, since the beginning, was the dependence of responsivity from temperature as shown in Figure 3.5. Although the temperature on the PCB is continuously measured by means of thermistors, this data are not provided to the SPS algorithm. The adopted solution is a narrowing of the wavelength bandpass to the less temperature-sensitive range obtained by means of a filter coating on the sensor entrance window.

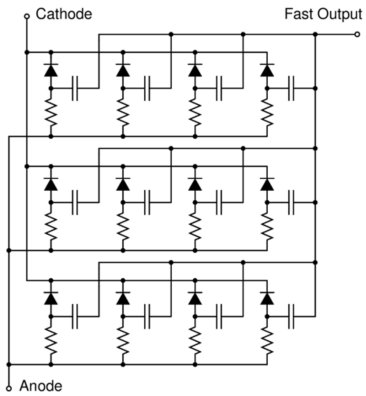

Figure 3.3: Simplified circuit schematic of a SiPM.

Figure 3.4: TO-5 package.

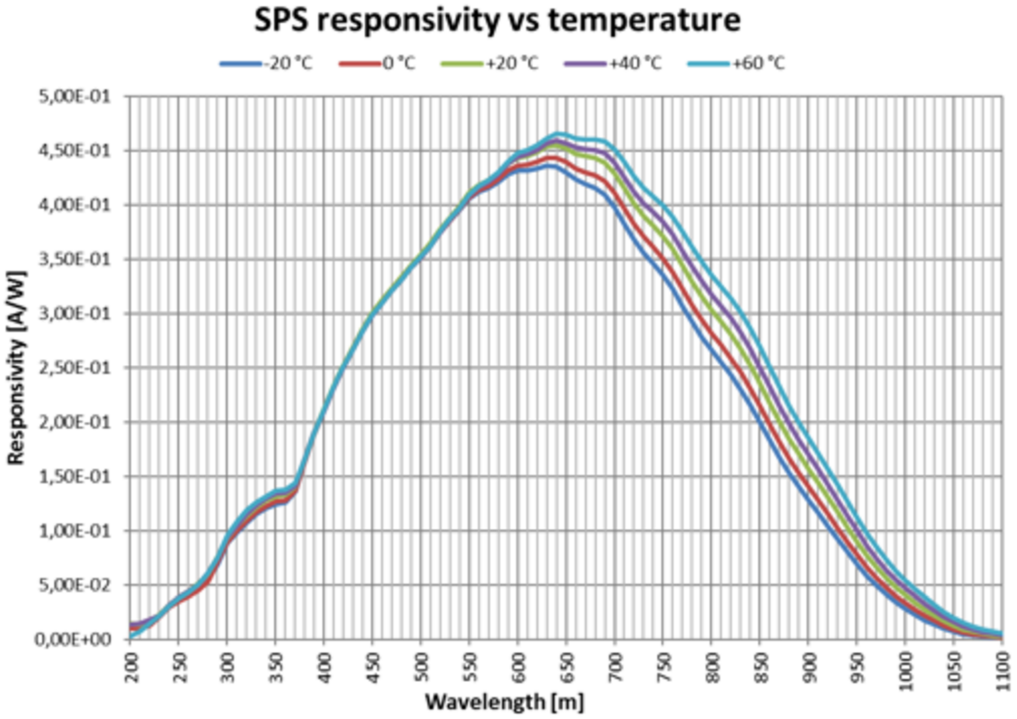

Figure 3.5: The responsivity (A/W) curves measured on a SiPM (MicroFB-30035-X18) with the same characteristics of the one finally adopted (MicroFC-30035-X05) as a function of wavelength for different temperatures from $-20\,^{\circ}\mathrm{C}$ to $40\,^{\circ}\mathrm{C}$.

3.1.3 The flange and the pinholes

The flange hosting the SPS PCB (Printed Circuit Board) is built in Aluminium type 6061, machined with standard workshop procedures.

After cleaning, all the following manipulations, inspections and assemblies have been done in clean room in controlled conditions.

Polished aluminium is applied to the SPS front surface in order to reduce the radiative heat flux loss to deep space during the coronagraphy period considering that the flange must be passively stabilized in temperature. For this reason the SPS flange is conductively linked to the Coronagraph Optical Tube with a 0.2 mm thickness CHO-THERM® interstitial material (conductivity $2\,\mathrm{W\,mK^{-1}}$).

The radiative environment is specified by the request that the SPS thermal design shall consider a conductive interface temperature as shown in

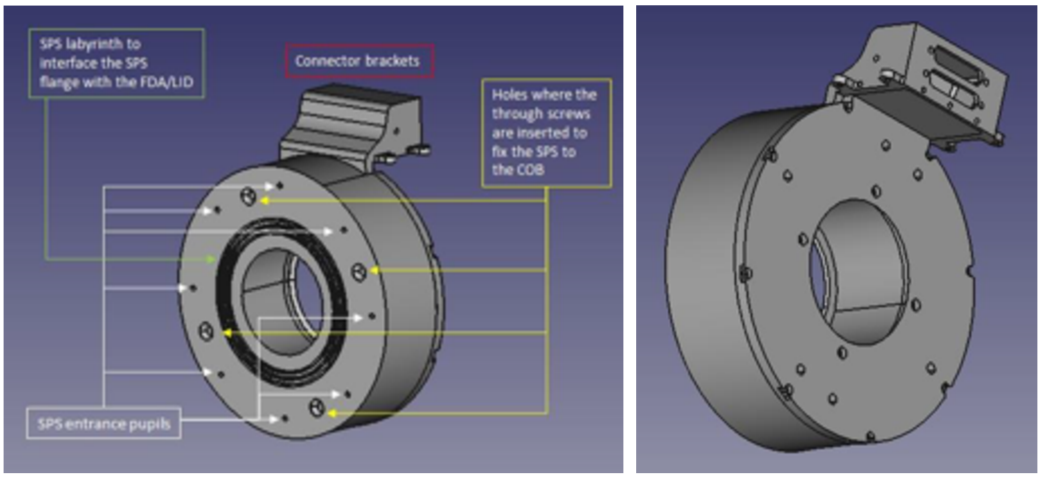

Figure 3.6: CAD views of the SPS flange. Left: front view with the indication of SPS holes positions. Right: the back part before mounting on the optics tube.

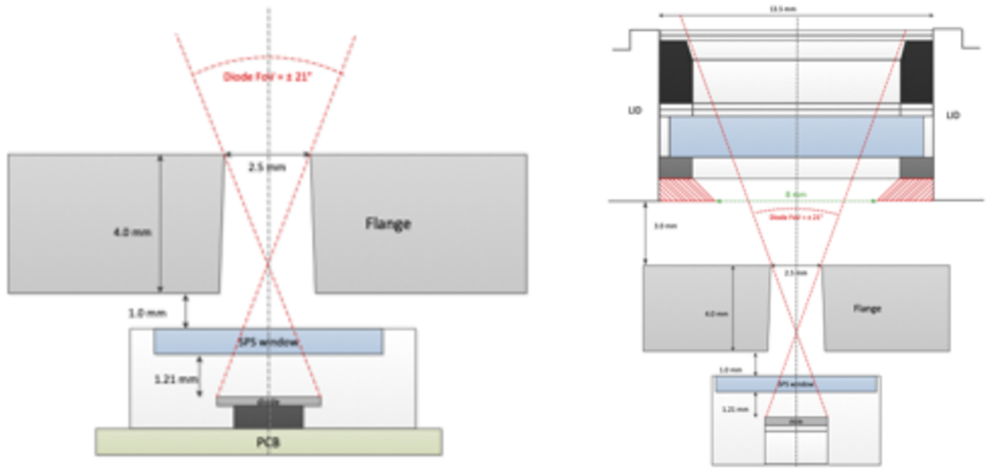

Figure 3.7: Sections of the SPS pinholes field of view when in operation (left) and with the front door closed (right).

Table 3.1 and a CTE (Coefficient of linear Thermal Expansion) of $23.6 \times 10^{-6}\, m/m \cdot K$ (Aluminium) (SPS-6301 and SPS-6303).

The temperatures reported in Table 3.1 refer to the four cases: minimum and maximum temperature (COLD and HOT) in operative and non-operative conditions (OP and NOP).

The Aluminium surface is treated externally with a chromate conversion coating and the internal and optically active surfaces are black painted with

(°C)	HOT OP	COLD OP	HOT NOP	COLD NOP
SPS	**40.7**	**29.8**	78.7	-19.6
Tube	36	34	77.3	-14.6
FDA structure	70.3	-36.8	72.9	-34.2
FDA lid	68.5	-80	72.9	-82.3
Pupil	36	34	70	-14.5

Table 3.1: SPS flange and interfaces thermal environment (FDA: Front Door Aperture).

ACKTAR *Magic Black*™. The flange is bolted with M4 screws to the optics tube.

In the front side of flange there are eight pinholes of 2.5 mm diameter, leaving enough margin (250 µm) on each side of the square SiPM to take into account the mechanical uncertainties. The area effectively illuminated is thus:

$$S = (2.5\,mm)^2 \times \pi/4 = 4.91\,mm^2 \tag{3.1}$$

The field of view is 21°×21°, also when covered by the lid, as shown in Figures 3.7.

The SPS is designed to operate in vacuum $<10^{-4}$ hPa (SPS-7220). In order to avoid structure deformations during launch depressurisation, the flange is equipped with venting holes. SPS shall have to withstand depressurisation rates up to 20 mbar/s during launch vehicle ascent phase.

3.2 SPS working principle

SPS measures the levels of illumination in the penumbra and provides data to the algorithm that translates the DNs (Digital Numbers) into three-dimension displacement of the Coronagraph spacecraft with respect to the Occulter spacecraft.

The level of light impinging on the sensor is linked to the fraction of the solar disk seen by the point in which the sensor is located. It spans from no illumination at all (with the exception of stray-light), when the sensor is located in the umbra, up to full Sun, for positions out of the penumbra. When in the penumbra, the quantity of light impinging the SPS sensors can be, theoretically, quantified by calculating the fraction of the solar disk in

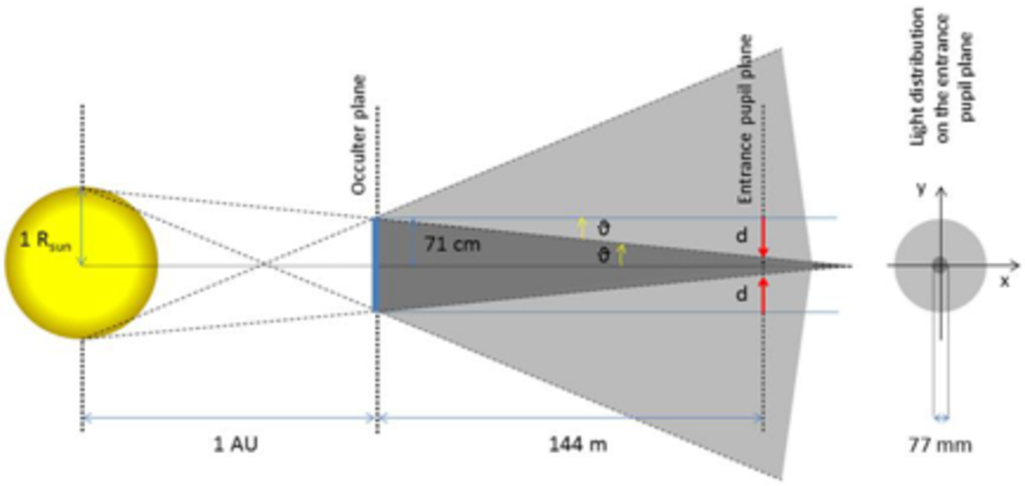

Figure 3.8: Image, not to scale, showing the penumbra (light grey) and the umbra (dark grey). On the right, umbra and penumbra projected over the entrance pupil plane.

the sensor field of view.

3.2.1 Sun irradiance profile

Geometrically, the solar disk shape can be considered with good approximation as a circle, while the occulter is better described as an ellipse in order to take in account any OSC tilt. In Figure 3.9 the sector of Sun disk emerging behind the occulter is given by the intersection between the yellow circle representing the solar disk and the grey ellipse representing the tilted occulter.

Being the SPS sensors located very close to the edge of the umbra region, the crescent-shaped fraction of the disk is located at the solar limb. For this reason we must consider the "limb darkening effect" and the possible presence of sunspots close to the Sun limb (see Figure 3.10).

Because of the *limb darkening* effect, the emission at the Sun center is about 2.7 times stronger than at the limb. Furthermore, the light spectral content changes with a bigger contribution at longer wavelengths [17] (reddening, see Figure 3.10) moving away from the center.

This effect can be included in the formula (3.2) below [13] considering

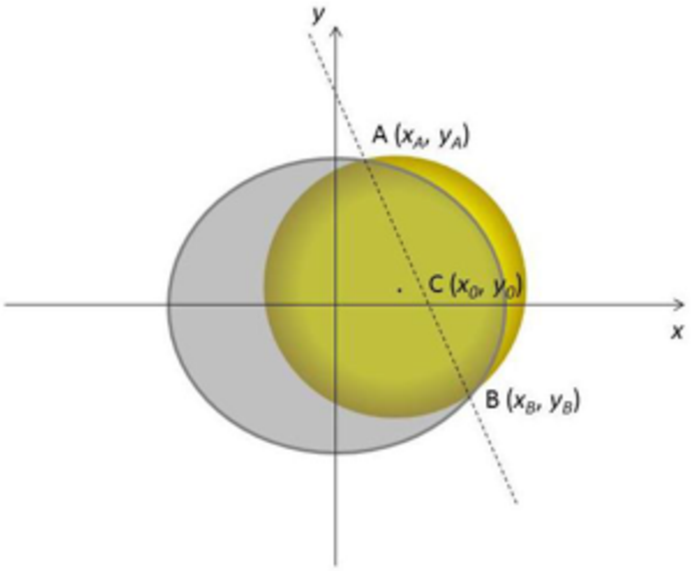

Figure 3.9: Image of the geometrical fraction of Sun (yellow disk) emerging behind the occulter (grey ellipse).

the right parameterization of the spectral content:

$$I_\lambda(\vartheta) = I_{\lambda 0}(1 - u_\lambda - v_\lambda + u_\lambda cos(\vartheta) + v_\lambda cos^2(\vartheta)) = I_{\lambda 0}\, G(\vartheta) \tag{3.2}$$

where λ is the wavelength, u_λ and v_λ are the limb darkening coefficients and ϑ is the angle formed by the normal to the Sun and the line-of-sight.

On the other hand, it is not possible to know in advance if a single sunspot or a group of them will be located close to the Sun limb. In this case there could be a significant reduction depending on the size and the number of the sunspots. The sunspot contribution is treated in detail in the error budget section (5.4.4).

This area needs to be integrated over the variable function of the limb darkening that provides the disk brightness as a function of the angle ϑ between the considered point on the disk and the line of sight. The input irradiance [mW cm^{-2}] computed above is converted to input power [mW] and, finally, into a current signal [A] if the area S [cm^2] of the entrance pinhole in front of the SPS is known. This cannot be obtained by means of a simple algebraic multiplication, but rather it is a smoothing of the input irradiance curve over the geometric 2-D dimensions of the entrance pinhole.

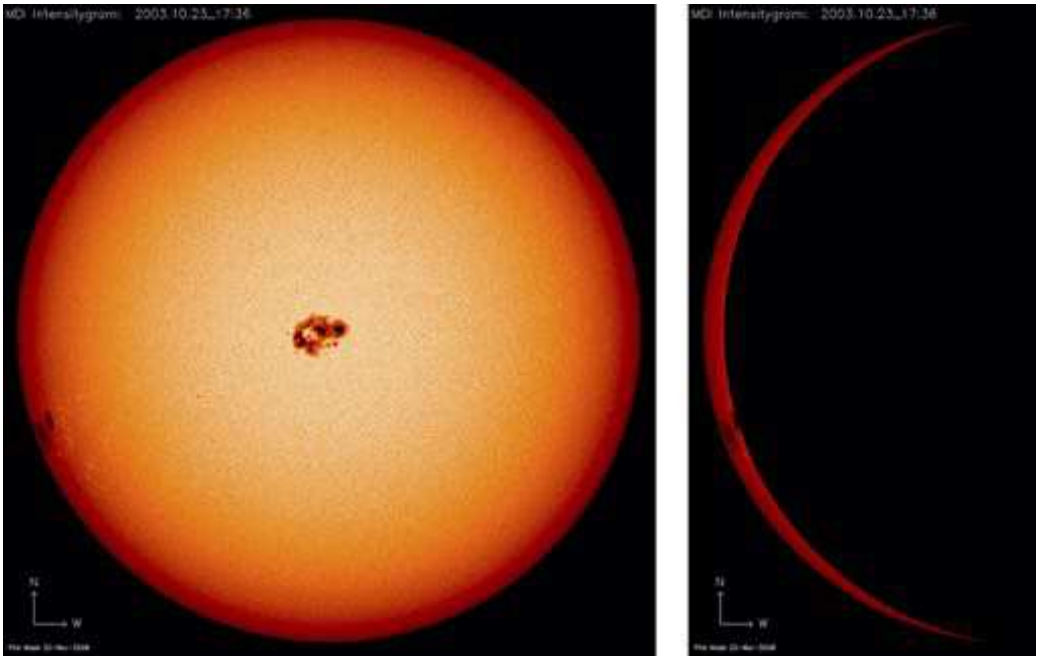

Figure 3.10: Left: a full Sun image with sunspots showing the limb darkening effect. Right: a partial occultation of the Sun disk that clarifies how important is the limb darkening effect and how one or multiple sunspots on the Sun edge can influence the SPS measurements.

The input solar power, L, is obtained from the following integral:

$$L = \int_{A_{pinhole}} \int_{\Omega_{SPS}} \int_{\lambda_{min}}^{\lambda_{max}} I_{\lambda 0} \left(1 - u_\lambda - v_\lambda + u_\lambda cos(\vartheta) + v_\lambda cos^2(\vartheta)\right) d\lambda \, d\omega \, dy \, dz \tag{3.3}$$

where $\lambda_{min} = 500\,nm$, $\lambda_{max} = 660\,nm$ delimit the filter bandpass, and Ω_{SPS} is the solid angle subtended by the fraction of solar disk area seen in the penumbra.
The SPS radiometric calibration function is a parameter K (W/A) that is intended to be used for the in-flight SPS calibration measuring the output of the detectors covered by neutral density filters exposed to full Sun light.

$$K = \frac{\int_{A_{pinhole}} \int_{\Omega_{SPS}} \int_{500}^{660} I_{\lambda 0} \left(1 - u_\lambda - v_\lambda + u_\lambda cos(\vartheta) + v_\lambda cos^2(\vartheta)\right) d\lambda \, d\omega \, dy \, dz}{\int_{A_{pinhole}} f_{SPS} \frac{\langle G(\vartheta)\rangle_{\Omega_{SPS}}}{\langle G(\vartheta)\rangle_{\Omega_s}} \int_{500}^{660} F_\lambda T_W(\lambda) T_F(\lambda) \varepsilon_{SPS}(\lambda,\ T_{SPS}) d\lambda \, dy \, dz} \tag{3.4}$$

where $T_W(\lambda)$ is the neutral density filter transmissivity, $T_F(\lambda)$ is the band-pass filter transmissivity, $\varepsilon_{SPS}(\lambda,\ T_{SPS})$ is the sensor responsivity, f_{SPS} is the fraction of the solar disk area seen by the SPS in the penumbra, $\langle G(\vartheta)\rangle_{\Omega_{SPS}}$ and $\langle G(\vartheta)\rangle_{\Omega_s}$ are, respectively, the limb darkening function $G(\vartheta)$ averaged over the fraction of solar disk seen by the SPS and over the full Sun.

K, with all the precautions (in particular the wavelength cut-off under 500 nm), does not vary more than 1%, a level of uniformity fit to the precision required.

It is possible to obtain, by simulations: penumbra profiles, the expected current signals or the equivalent digits (DN). These values were calculated at the nominal ISD, as a function of the radial distance from umbra to 120 mm, and are tabulated in [2] and shown in Fig. 3.11. The values corresponding to the edges of *requirement* and *goal box*, defined in Section 3.3.1 below, were used to dimension opportunely the electronics parameters. Some of the significant values are written in Table 3.2.

3.2.2 External Occulter diffraction and shape

The external occulter produces a diffraction pattern on the plane of the telescope entrance pupil that may disturb the coronagraph observations.
For the SPS subsystem the diffraction profile laying around the entrance aperture plane has an impact on the detected signal, especially at low signal levels.

Detailed studies [21] [22] have been performed in order to decide which was the best shape for the occulter edge (knife-edge, toroidal etc.).
Diffraction has been calculated [1], at a fixed wavelength of 550 nm, on the pupil plane for a knife-edge occulter and the whole solar disk as a source.

At the end the final design foresees a toroidal border having a curvature radius of 700 mm. With this profile, having a radius of curvature comparable with the external occulter radius, we obtain a reduction of $\approx 67\%$ of the diffracted light in the telescope pupil with respect to the knife-edge case.
The characterization of the stray light contribution falls outside the scope of this work.

Y or Z pos. (mm)	input power (µW)	output current (µA)	output (DN)
37	0	0	0
38	2.32E-02	8.89E-03	3
39	7.02E-02	2.69E-02	11
40	1.70E-01	6.53E-02	26
41	3.35E-01	1.28E-01	52
...	...	...	...
54	5.88	2.26	925
55	6.47	2.49	1017
56	7.08	2.72	1113
...	...	...	...
69	16.18	6.21	2544
70	16.96	6.51	2666
...	...	...	...
120	64.65	24.82	10165

Table 3.2: Tabulated values of SPS input power (L) output currents (C) and DN as a function of the radial distance in mm at nominal ISD [2].

3.3 SPS requirements

The SPS subsystem, sensors and electronics, must be entirely enclosed in the empty volume present in the flange holding the front door. This is required by: "The SPS dimensions shall be included within the envelope volume of the Coronagraph Optical Box" (requirement: COR-IID-0053).

Concerning the SPS performance, the specific SPS subsystem requirements apply: the SPS photodiodes shall measure the penumbra light intensity, without saturation or zero signal (only for requirement box, SPS-4201), in a lateral volume of ± 50 mm and a longitudinal volume of ± 500 mm with respect to their nominal positions (SPS-4202) and shall have a current sensitivity compatible with the penumbra illumination profile (SPS-4203).

The requirements above stem from the coronagraph requirements:

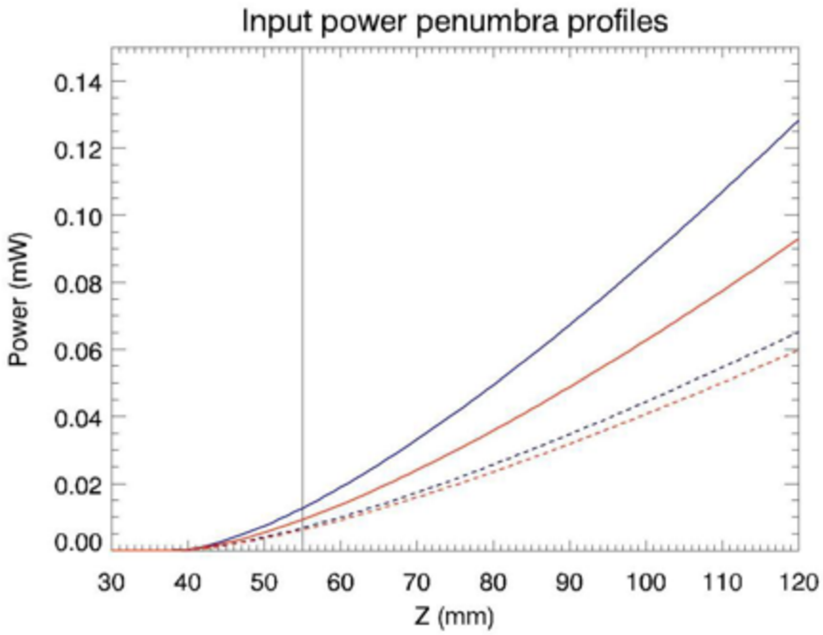

Figure 3.11: Input power penumbra profiles (mW) integrated between 300 nm and 700 nm (blue solid line) and between 500 nm and 660 nm (blue dashed lines). The red curves correspond to the blue curves after the inclusion of the SPS window glass transmittance and the SPS filter coating transmittance. Vertical line shows the nominal location of SPS.

Req. ID	Req. Title	Req. Text
COR-IID-0018	SPS performance requirement	The Shadow Position Sensor (SPS) shall be used to verify that the Coronagraph Instrument's entrance pupil is centered within the umbra cone of the Occulter Disk. At the ISD (specified in Section 2.6.2) and within ±10 mm of the ideal position in lateral and ±100 mm in range, the SPS shall have a lateral measurement accuracy of 50 µm (3σ) in each axis, and a longitudinal measurement accuracy of 1 mm (3σ). These accuracies are with respect to the axis connecting the center of the Occulter with the center of the Sun.
COR-IID-3005	SPS performance goal	The SPS should be able to return a 3-D relative position measurement at reduced performance within a range of ±50 mm in lateral and ±500 mm in longitudinal (i.e. the SPS should always return a 3-D measurement within a box of 100 mm in width and height and ±1000 mm in depth, centered on the ideal position), and assuming a maximum relative velocity of the CI with respect to the umbra cone of 5 mm s^{-1} along Y or Z axis and 50 mm s^{-1} along X axis.

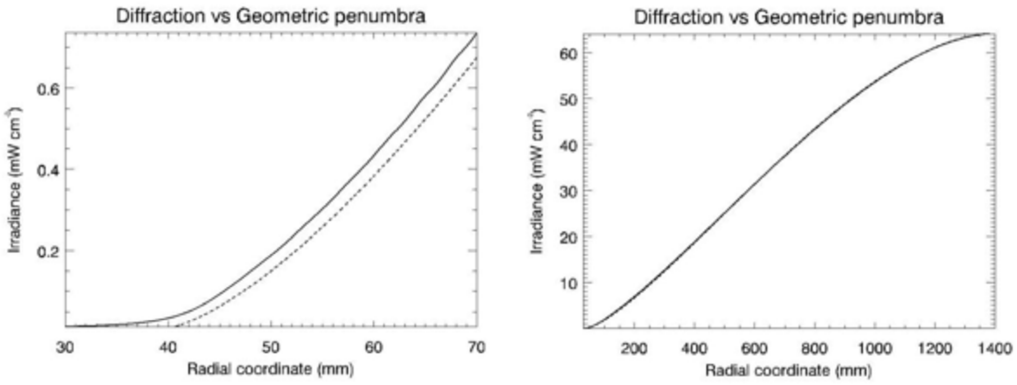

Figure 3.12: Geometrical (dashed) and diffracted (solid) irradiances in the low-end region (left) and in the whole range extending up to the full Sun (right).

Other relevant requirements ask that "the SPS data shall be sent to the Onboard Data Handling system with an update rate of 2 Hz" (COR-IID-0024) and that "upon reception of the relevant TC from the OBSW (On-Board Software), the SPS data shall be sent as Housekeeping TM in less than 100 ms" (COR-IID-7002).
The SPS data shall be as a minimum (COR-IID-7003):

1. the output from the position estimator that uses the reading from the SPS diodes;
2. the "raw" SPS diode readings as they are used by the position estimator in the Coronagraph System;
3. a validity flag that indicates whether the SPS data can be considered valid by the OBSW for use in the GNC loop.

Finally, "the Coronagraph System design shall allow SPS measurements even when the Coronagraph Front Door Assembly is closed" (COR-IID-7004); and "the SPS design shall not contain any single point of failure" (COR-IID-3007).

This last requirement needs an interpretation (see also Section 5.1.3) because: SPS itself could be designed to be free from single points of failure (SPF), but, depending on controller (CCB) architecture, one failure on the CCB side could make the full SPS non-operational.

3.3.1 *Requirement box* and *goal box*

Referring to the requirements COR-IID-0018 and COR-IID-3005, two operational spatial regions (*boxes*) are defined around each sensor in which it is expected to perform measurements with different performance that are:

1. **Requirement box**, centered in the nominal position coordinates of each sensor (e.g. (0, 55 mm, 0) for sensor #1) and considering displacements in the plane Y-Z up to ±10 mm and up to ±100 mm in the X direction.

2. **Goal box**, centered as above and considering displacements in the plane Y-Z up to ±50 mm and up to ±500 mm in the X direction.

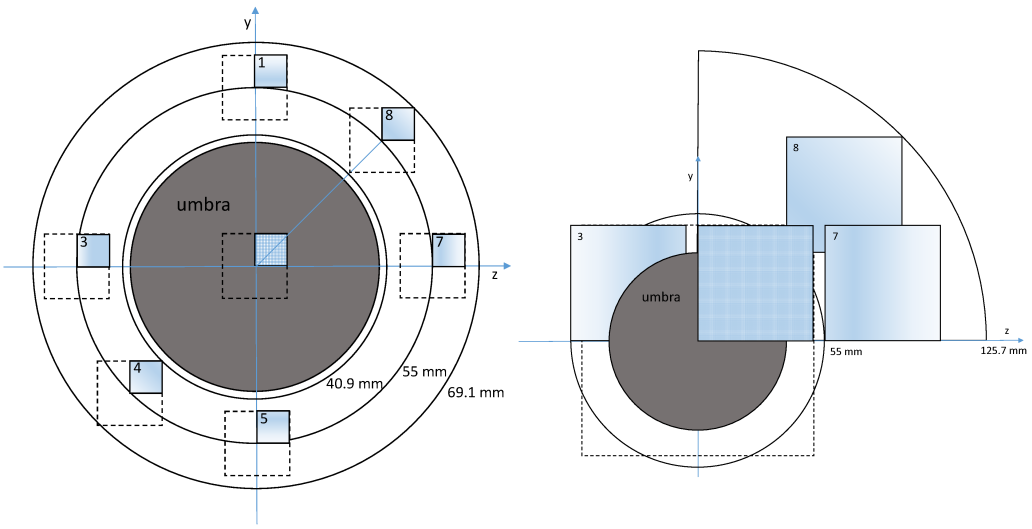

Figure 3.13: The zones of the plane Y-Z reached by some of the eight SPS sensors when in the *requirement box* (left) and *goal box* (right). For sake of simplicity, only positive displacements are considered and 1/4 of the covered region is shown.

These two 3-D spaces have been extensively used in all the SPS development process in order to identify the two regions of interest: the small one ($20 \times 20 \times 200\,mm^3$), in which there is a request on the attainable precision both in lateral and in longitudinal displacements, and the large ($100 \times 100 \times 1000\,mm^3$), in which it is sufficient to return a measurement.

The two ESA requirements can be translated into constraints on the SPS electronics parameters and we treat them separately: COR-IID-3005 sets the

range and COR-IID-0018 defines the sensitivity needs and, after the range is established, the dynamic range and the number of equivalent bits.

In Table 3.3, the values of the expected irradiances, currents and DN [2] are listed in some representative positions (identified by the sensor coordinates (x,y,z)). The minimum and maximum values are taken at the boundaries of the *requirement box* and of *goal box*.

Table 3.3: Irradiances and dynamic range requirements

Position	Expected value in µW	Expected value in µA	DN	Notes
Nominal (0, +55, 0)	6.472161	2.485035	1017	ISD
Variation for 50 µm displ. at nominal (0, $+55 \pm 0.05$, 0)	± 0.02977	± 0.01145	± 5	50 µm transversal
Min. for req. box (-100, +28.9, +28.9)	0.25	0.096	39	ISD-100 mm
Max. for req. (+100, +48.9, +48.9)	16.5	6.335	2595	ISD+100 mm
Min. for req. box sensor (-100, +28.9, +28.9)	≈ 0	≈ 0	≈ 0	Electronic noise or residual diffraction
Max. for goal box sensor (+500, +88.9, +88.9)	70.7	27.1	11120	ISD + 500 mm

3.3.2 SPS operative range

ESA requirement COR-IID-3005 provides the relevant constraint concerning the range that derives from the condition of "non-saturation" for the measurements taking place inside the larger *goal box*. For this box the upper radial distance is $55 + 50\sqrt{2} \approx 125.7mm$ whereas the lower limit falls in the umbra, that is we consider, ignoring the diffraction, a zero signal. No accuracy requirement is given.

This requirement can be satisfied setting opportunely R_F, the feedback resistor of the trans-impedance amplifier (A_{TIA}) in the first stage of the SPS readout electronics. In the first version of the SPS electronics the range was established by the first two stages $A_{TIA} = 10\,k\Omega$ and $A_{LG} = 12$).

In the final version of SPS electronics the gain $A_{TIA}(V/A) = R_F(\Omega)$ have been tuned considering also the presence of the coating on the SiPM rad-hard windows filtering the solar spectrum ($500nm \leq \lambda \leq 660nm$). From tabulated values of irradiance [2] we used the simplified inequality:

$$I_{max} \times S \times K \times R_F \leq 5\,V$$

where I_{max} is the maximum value of irradiance present at the goal box external edges (e.g. position (+500,0,125.7)), S=4.91 mm^2 is the sensor illuminated area, and K is the proportionality factor between power and current (K=L/C, comprising responsivity, band-pass filter and rad-hard windows transmissivity, illuminated area convolution etc.) reduces to 2.67 W A^{-1} and is quite constant as a function of the wavelength.

The formula expresses the concept that the current generated by the SiPM, for the maximum irradiance impinging on the area S, is transformed in a voltage by the resistor R_F and this cannot exceed the ADC input range of 5V.

Setting the proper value for $R_F = 100\,k\Omega$, with reference to Table 3.3, between the upper margin of the *goal box* (125.7 mm) and the saturation level at about 175 mm, we have margins of about 85% in terms of power and current and of about 40% in terms of lateral displacements.

3.3.3 SPS resolution and sensitivity

ESA requirement COR-IID-0018 specifies the readout electronics sensitivity needs in the requirement box only. We have taken into consideration, for the requirement box, the radial distances between $55 - 10\sqrt{2} \approx 40.9mm$ (lower limit) and $55 + 10\sqrt{2} \approx 69.1mm$ (upper limit). For the sizing of the electronics it was considered, at the beginning [6], a maximum current density of 412.4 µA/cm^2, a minimum of 6.273 µA/cm^2 and, in the low-end of the range, a required sensitivity of only 0.025 µA/cm^2. The last value is the sensitivity required to detect a longitudinal displacement of 1 mm, while for a 50 µm lateral movement the sensitivity is ten times higher. We can conclude that the leading requirement on sensitivity is the longitudinal one

and that, in case it is satisfied, the requirement on lateral displacements is automatically satisfied too.

There was the need to develop an electronics having a dynamic range equivalent to 14 bits or higher, in fact: $\frac{412.4}{0.025} = 16496 \approx 2^{14}$. Two solutions were proposed to obtain this resolution:

1. using a 16-bit ADC interfaced with a multiplexer;
2. using a serial, 8 inputs ADC and enhance the precision subtracting to each input a programmable voltage pedestal.

At the end, for reasons linked to the input impedance of the available space-qualified multiplexers, it was decided to adopt the second solution, described in Section 4.1.3.

In the final design, as a consequence of the changes explained throughout Chapters 4 and 5, a second amplification stage $\times 5$ allows us to obtain the improved resolution necessary only for the lowest signal levels. For these signals, one LSB (Least Significant Bit) at the output of the second stage (high-gain) corresponds to an input of 2.44 nA compared to 12.2 nA of the first (low-gain) stage output. The two measurements are digitized and provided simultaneously. The algorithm compares the high-gain value to a threshold in order to check if it is too near saturation and, in this case, multiplies by 5 the low-gain value to make data homogeneous.

To quantify error contributions, the displacements around the nominal position can be translated in number of DN using the responsivity factor $g = 10\mu m/DN$.

A plot of the data counts (DN) as a function of the lateral position in (mm) is shown in Figure 3.14, demonstrating that we are still compliant with the original request of a 50 µm sensitivity.

3.4 Algorithm

Several metrology algorithms [1] [12] [11] convert the digital readouts into three spatial coordinates that express how the origin of the CPLF reference frame (nominally placed at the center of the coronagraph aperture on the

[1]This description of the SPS algorithm has been published as "Metrology on-board PROBA-3: The Shadow Position Sensors subsystem" in *Advances in Space Research - Special Issue on Satellite Constellations and Formation Flying* [36].

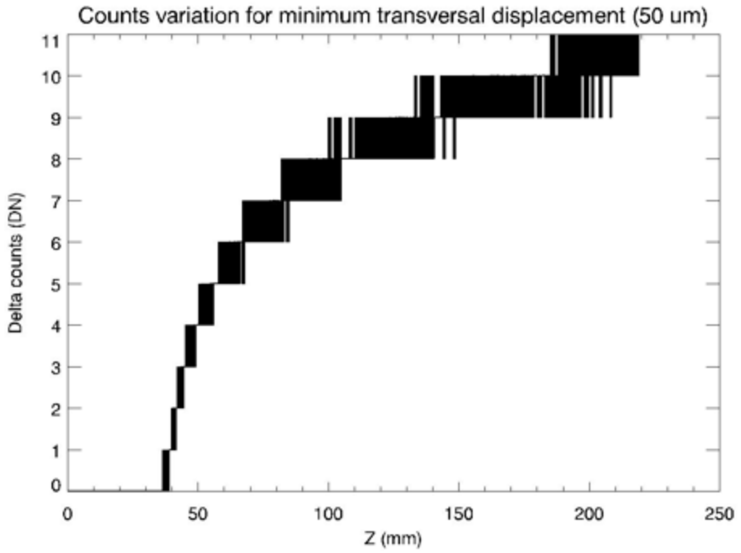

Figure 3.14: Expected variation of counts detected by a single SPS for the minimum transverse displacement by 50 µm.

CSC, Y and Z on the plane, X pointing internally to the instrument) moved from its nominal position.

Beside the fundamental data concerning the 3-D position (low and high gain measurements, temperatures), other functions (flags) are given in order to comply with COR-7197 (see requirement 2.6.5).

3.4.1 Pseudo-paraboloid algorithm (lateral)

In order to obtain the performance originally requested of 50 µm accuracy in a $200 \times 20 \times 20 mm^3$ box (as explained in Section 3.3.3), an accurate method based on a third order polynomial equation ("pseudo-paraboloid") was used to fit the penumbra profile.

$$\begin{cases} z_0 = 2 \cdot \sqrt{-\frac{A}{3}} \cdot \cos\left\{\frac{1}{3}\left[\arccos\frac{(R_7-R_3)a^3}{4\sqrt{-\frac{A^3}{3}}}\right]\right\} \\ y_0 = 2 \cdot \sqrt{-\frac{A}{3}} \cdot \cos\left\{\frac{1}{3}\left[\arccos\frac{(R_1-R_5)a^3}{4\sqrt{-\frac{A^3}{3}}}\right]\right\} \end{cases}$$

where:

$$A = c^3\left(\frac{1}{a} + \frac{2r_{SPS}}{b^2} + \frac{3r_{SPS}^2}{c^3}\right)$$

with $r_{SPS} = 55\,mm$.
R_n are the digital readings of opposite sensors.
The coefficients of this curve a, b and c, are re-configurable and depend on the distance between the two spacecraft (ISD).

3.4.2 Linear algorithm (lateral)

The pseudo-paraboloid algorithm is prone to give inaccurate results (e.g. in cases it which it generates complex numbers), for this reason a more stable algorithm is used to raise a flag on the results, signaling to the GNC not to use SPS output.

This method is based on a proportionality relation between the difference of the digital reading (R_n) of opposite sensors and the coordinates of the umbra center within the lateral plane. The computation of the Y-Z coordinates is performed using a linear equation, parameterized with re-configurable coefficients d_z and d_y in order to consider any possible occulter distortion.

$$\begin{cases} z_0 = \frac{(R_7 - R_3)}{d_z} \\ y_0 = \frac{(R_1 - R_5)}{d_y} \end{cases}$$

3.4.3 Longitudinal position computation

The longitudinal coordinate x_0 of the pupil center is calculated considering a quadratic fitting describing the dependence of the signal present at 55 mm from the coordinate X only. Inverting this relationship:

$$x_0 = \left(\frac{-K - \sqrt{K^2 - 4H\,(L - R_{55comp})}}{2H} + J\,d_0^2 \right)$$

where: $R_{55comp} = R_{0comp} - \Delta R$, and $d_0^2 = z_0^2 + y_0^2$.
R_{0comp} (linked to the location x_0 of the occulter center) is the average of four values calculated independently from the radiance values R_n exploiting the knowledge of the y_0 and z_0 coordinates obtained with the previous methods, while H, J, K and L are the quadratic fit coefficients and are re-configurable.

Chapter 4

SPS - design evolution

4.1 Introduction

4.1.1 Development Plan

Every space project having the purpose of realizing a spacecraft or an instruments typically passes through a series of 7 phases, from 0 (mission analysis and identification) to F (disposal), described in ECSS-M-ST-10C standard. The conclusion of most phases is marked with a *review*, a formal passage in which documents are given to the client (data-pack), design is frozen or products are delivered.

The PROBA-3 Development Plan [48] is summarized in the following Table 4.1:

Phase	Milestone	Description
Bridging	KO	Kick off
	MS1	-
	MS2 (PCM)	Payload Consolidation Milestone
Phase C	KO	Kick off
	CDR	Critical Design Review
Phase D	QR	Qualification Review
	AR	Delivery, Acceptance Review
Phase E1	IOCR	In-orbit Commissioning Review

Table 4.1: Overall initial PROBA-3 project Development Plan schedule

After the reviews concerning requirements (PRR and SRR, Preliminary

and System Requirements Reviews) in which all system requirements have been properly identified, the PDR (Preliminary Definition) concludes B (bridging) phase.
Phase C is devoted to the detailed definition of the design and to the fabrication of the system (in our case SPS). It has been concluded by the CDR (Critical Design Review). PDR and CDR are iterative processes in which RIDs (Review Item Discrepancies) are open, discussed and, finally, closed.
At this moment, PROBA-3 is in the middle of D phase (qualification accomplished, production of flight hardware in course, integration, and launch in 2022).
Next phases will be the utilization (E), i.e. the space mission activities and the disposal (F) with the re-entering in atmosphere, after 2.5 years of mission, of the two spacecrafts.

4.1.2 Model philosophy

The items produced (*deliverable*) during a space project, hardware, software etc., evolve from a functional design to a final instrument with proven performance that will fly on the finished mission.

The "model philosophy" consists in the programmatic definition of a series of *models*, in our case hardware, that help to progress from the initial conception of a device or instrument to the final version (FM or PFM, Flight or Proto-Flight model).

The SPS model philosophy is summarized in Table 4.2.

The various models have different purposes and different grades of similarity ("representativeness") with respect to the final SPS. They are subject to several tests either electrical/functional or environmental (listed in Table 6.1).

4.1.3 Original design

Following the argumentation developed in Section 3.3.3, about competing needs in range and sensitivity, we can illustrate [29] the design of SPS electronics as it was at the end of the bridging phase. Figure 4.2 shows a scheme of the readout process. The 3-stages amplification chain is shown in Figure 4.1.

The first two amplifiers transform the SiPM photo-current in a voltage

Model	Representativeness	Use
Evaluation Board (EB)	Breadboard, single sensor amplification chain	Validation of sensor characteristics
Development Model (DM)	Functionally and electrically representative of the PDR design, COTS	Subject to electrical and functional tests, design verification
Structural-Thermal Model (STM)	Thermo-mechanical representative	Thermal models correlation, integrated into SPS flange and subject to system level tests
Advanced Demonstration Model (ADM)	Functionally and electrically representative of the CDR design, COTS	Subject to electrical and functional tests, preparation of EQM test setup and procedures. Part of data-chain (Section 7.2
Engineering Qualification Model (EQM)	Flight representative (full flight design & flight standard with respect to dimensions, components and footprints) space-qualified processes and materials	Qualification, integration into the flange, environmental and electrical/functional tests. Calibration campaign. Part of data-chain
Flight Model (FM)	Full flight design & flight standard	Acceptance testing, integrated into the SPS Flight Model

Table 4.2: SPS model philosophy, ADM was not originally planned, INAF initiative.

(transimpedance amplifier - TIA) that is further amplified $\times 12$ in order to generate a signal V(LG) (Low Gain) compatible with the ADC (Analog to Digital Converter) input range (0-5V). The voltage V(LG) is digitized and provides a 12-bit value N(LG) that is used to select one of the 32 voltage levels present in a Look-Up Table V(LUT).

The output of the LG amplifier is also routed to the input of a $\times 10$ differential amplifier (High Gain). The HG differential amplifier subtracts the DC offset voltage ("pedestal"), provided by the DAC (Digital to Analog Converter) from the input signal and amplifies the difference, giving a new value V(HG) that is digitized in the 12-bit value N(HG).

Finally, the desired input is obtained as: $V = V_{LUT} + \frac{V_{HG}}{10}$ This voltage,

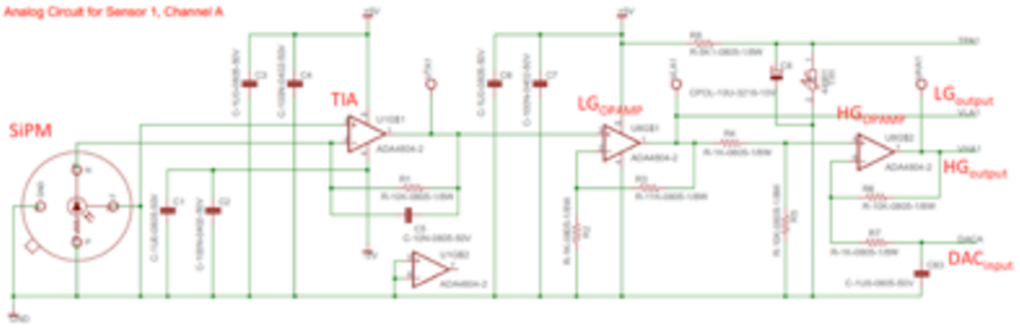

Figure 4.1: The amplification chain of one SiPM (original design)

being proportional to the input irradiance, can be translated in mW cm^{-2} applying only a constant multiplying factor.

The analog signals from the amplifiers and temperature sensors are digitized in such a way that the SPS to CCB interface shall comprise only digital signals (beside supply voltages). To convert signals from analog to digital, a 12-bit serial ADC model ADC128S102 with 8 inputs has been adopted. This ADC is available either as a commercial part or as a space qualified model ADC128S102QML. The serial readout allows a compact design of the electronics with a minimum signal count for the interface bus. The ADC input/output signals are *single-ended*, then a set of transmitters/receivers must be used for the final design LVDS (Low-Voltage Differential Signal) transmission.

4.2 EB - *Evaluation Board*

The Evaluation Board is a development model hosting a single sensor, type MicroFB-30035-X05, and a readout electronics based on the OP484 quadruple amplifier; the other characteristics as the amplification factors and components such as DAC and ADC, are the same as in the Development Model described below.

By means of a PC interface (GUI - Graphic User Interface, see Figure 4.4) it is possible to evaluate the performance of the sensor and of the readout electronics. The GUI allows the user to manually set a number from 0 to 4095 to program the DAC (Digital-to-Analog Converter) and to read back the N(LG) and N(HG) values provided by the ADC, optionally converted in voltages and in irradiances.

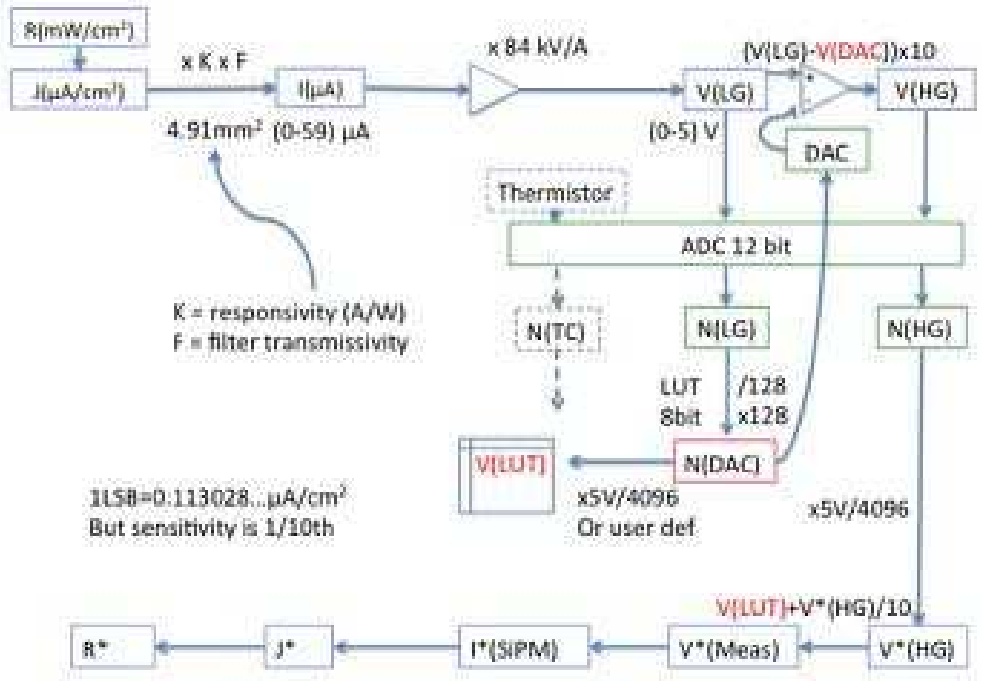

Figure 4.2: A scheme of the measurements taking place in the original SPS design.

In automatic mode, 20 pre-loaded DAC settings are used to cover the desired dynamic range. The interface software uses a readout scheme very similar to what is described in Section 4.3.

4.2.1 EB laboratory tests

I performed, in the laboratory of electronics of the University of Florence, several hardware (electrical) and software (functional) tests [29] on the EB device.

The first campaign of measurements regarded:

- Electrical tests (power supply, connections, USB communications, etc.).
- Cross-check of measurements taken in manual and automatic modes.
- Dark current measurements.

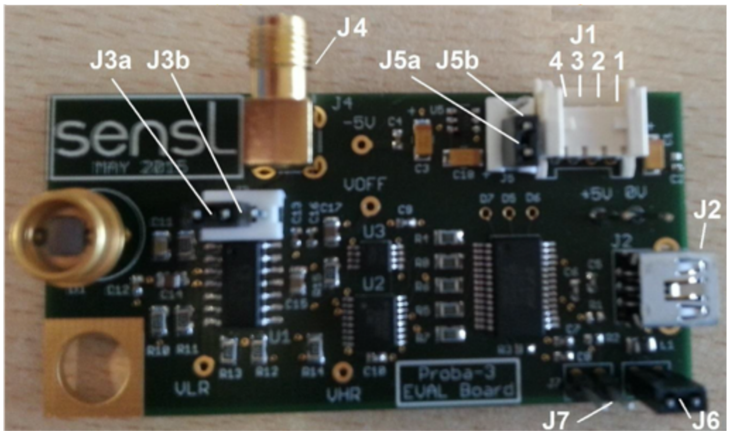

Figure 4.3: The single sensor evaluation board.

- Power supply noise tests using internal and external sources.
- Preliminary tests on the statistical distribution of measurements.

The output is given as the arithmetic average of a number *Sample Count* of measurements. I repeated the automatic readout for different *Sample Count* values so to collect significant statistics and to perform a study about the dependence of the variance from the number of samples. The results are given in Section 4.5.1.

The functional test allowed to verify the coherence of the readings taken in manual or in automatic mode exposing the sensors to 10 different levels of light flux (from dark to saturation). It was verified the proportionality, with a fixed ratio: $\frac{5}{4096} \times \frac{1000}{12} \times \frac{10}{9} = 0.113028$, between manual and automatic readout measurements.

The measured dark current was negligible, in fact the readout inside the black box gave a result of 0 both in manual and in automatic mode.

Other tests were done in conjunction with DM and reported below.

4.3 DM - *Development Model*

The SPS Development Model was fully representative in shape, dimensions and electrical characteristics of the final models as they were planned at the end of phase B, except for being built with COTS (Commercial Off-The-Shelf) components.

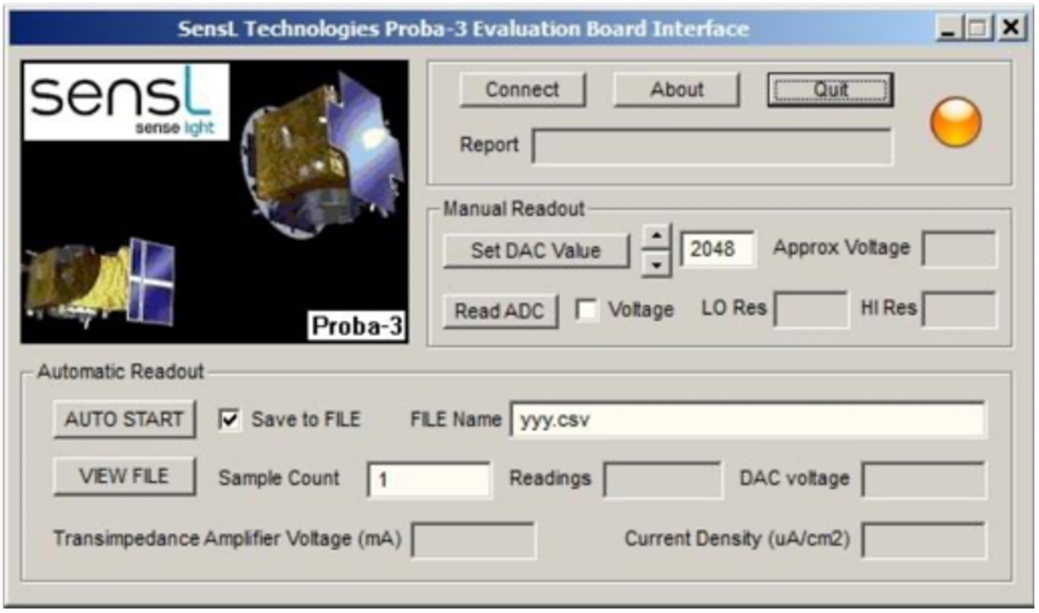

Figure 4.4: the Evaluation Board GUI main front panel.

It contains two identical circuits: Channel A and Channel B and each circuit consists of four analog sections interfacing to the SensL sensors model MicroFC-30035-X05. The analog readout circuits connect to a single-ended digital section for processing the signals and reporting the results to the interface bus. The schematic of a single chain is shown in Figure 4.1.

Another difference with respect to Evaluation Board, is that the OpAmp (Operational Amplifier) type has changed from quadruple (OP484) to dual (ADA4084-2). Anyway, the operation mode and the performance of the two OpAmp are very similar and the reason for changing was due to a potential problem discovered during the evaluation of the EB concerning the possibility of the HG amplifier to drive the ADC channel over negative values. The adoption of two ADA4084-2 separated devices allowed the trans-impedance amplifier to have a dual $\pm 5\,\mathrm{V}$ supply and the following amplifiers to have a single $+5\,\mathrm{V}$ supply.

Both in the EB and in the DM, only for testing purpose, the value of V-DAC can be arbitrarily set with a 12-bit resolution in manual mode by means of the graphical interface.

A separated Controller Board, commanded by the GUI, connects the Development Model with a host computer by means of a USB port. The

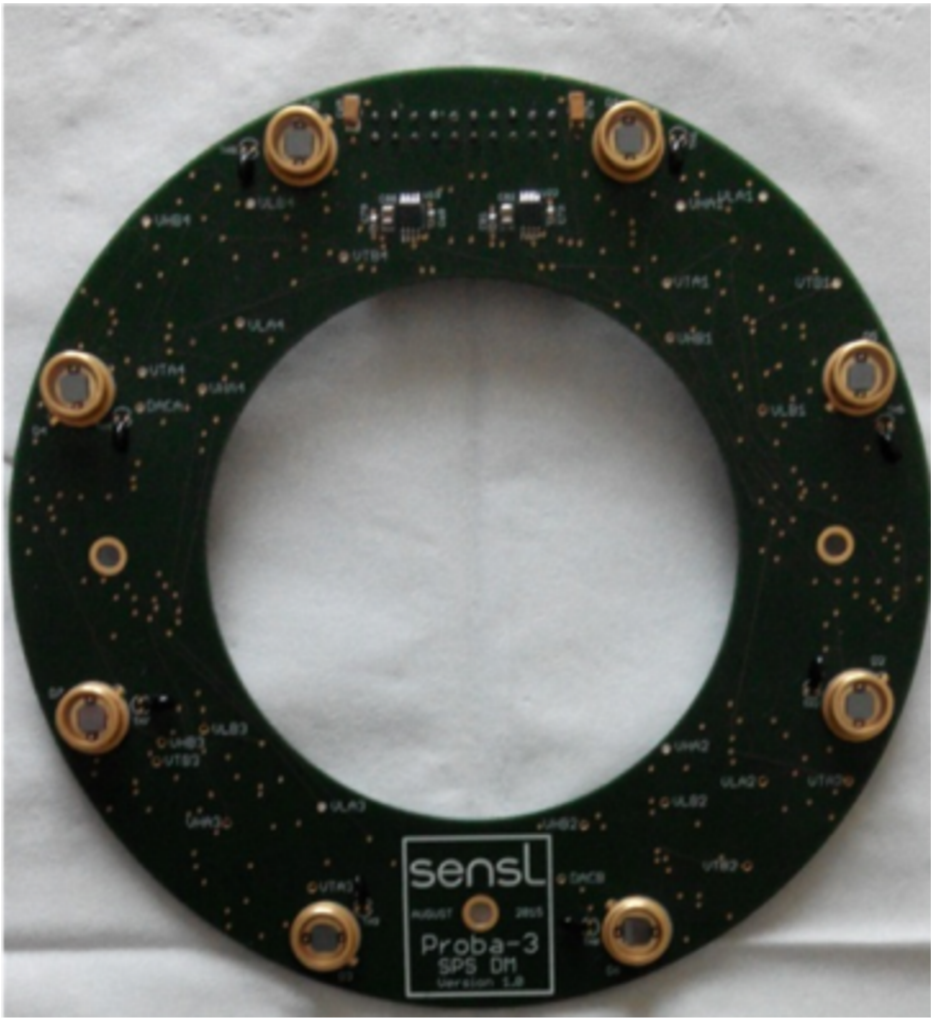

Figure 4.5: The Development Model.

graphic interface is very similar to the EB one: the SPS electronics can be read in **manual mode**, setting the N(DAC) values (one value for each channel A or B of four sensors) and reading back the ADC values N(LG) and N(HG) (in digital values or translated in voltages) or in **autonomous mode**, that is replicating the real readout algorithm that should have taken place in the flight model. In autonomous mode the FPGA continuously sets the DAC values and reads the ADC for the programmed number of samples.

The DM GUI gives the possibility to enter in the field **Ref. Voltage** the exact value of $V_A = V_{ref}$, from a minimum of 4.7 V to a maximum of 5.3 V; affecting the ADC conversion to irradiance values.

4.3.1 DM Laboratory tests

The Development Model was subject to the same hardware and software tests described in Section 4.2.1 for the EB and the results written in the P3-INF-RP-16004 report [29]. Additionally, relative DM/EB behaviour measurements were performed placing the Development Model and the Evaluation Board side-by-side on the optical bench.

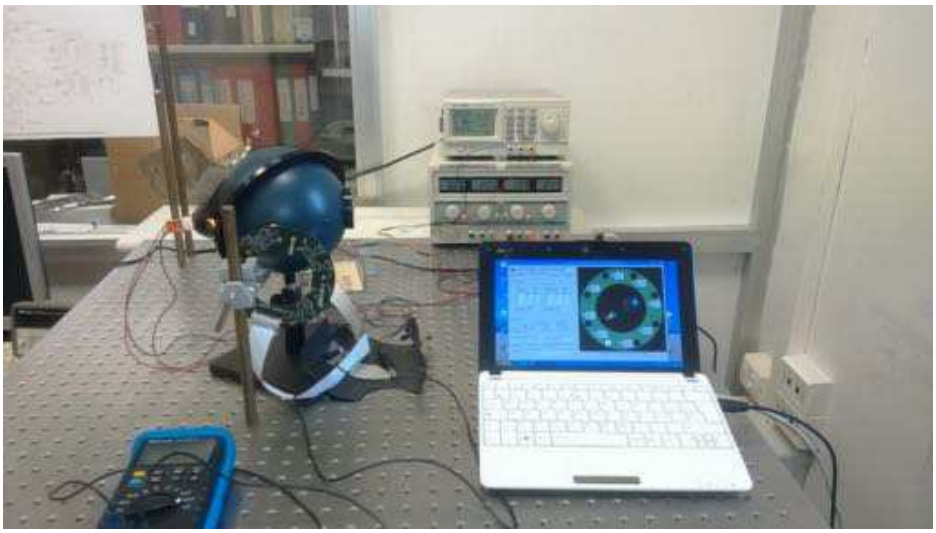

Figure 4.6: The laboratory setup for DM tests.

The DM and EB were powered alternatively by the SensL-provided power sources (a +6 V plug-in type in the case of the DM and the USB connection in the case of the EB) or by a laboratory power supply model IPS-2010.

The preliminary tests have been performed using a light source rather constant (not having available radiometric calibrated sources) obtained from a dichroic lamp powered by a bench power supply model DF 1731 SB 3A. The same tests have been repeated with a 4-inch integrating sphere, improving the statistical measurements accuracy. The light from the dichroic lamp was diffused by means of a sheet of Makrolon, 3 mm thick, having a transmission coefficient of about 60%.

During the functional tests some minor problems emerged, mainly due to the Application Software, but, a more serious anomaly for the DM was identified as a deviation from the ideal behaviour when operated in automated mode. The problem and its solution are described in detail in Section 4.3.2.

The dark current resulted negligible, inside the dark box each sensor

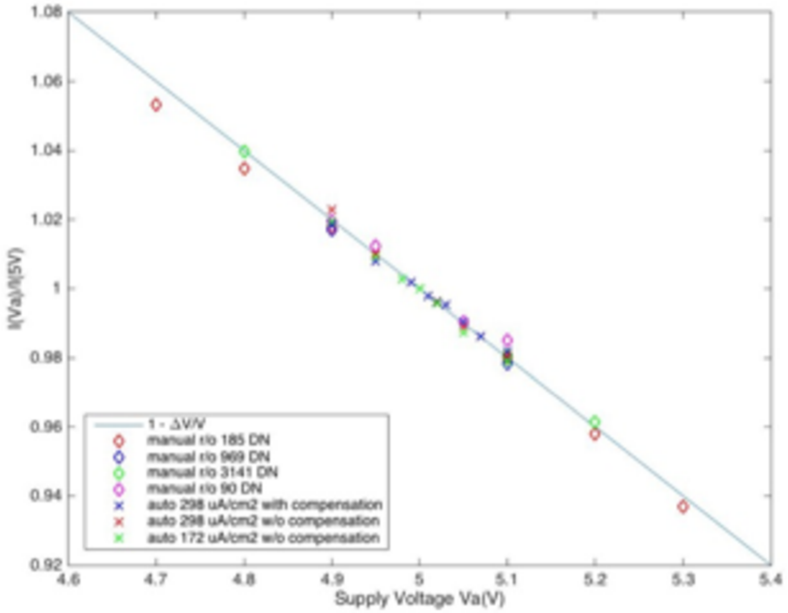

Figure 4.7: I(5V)/I(VA) ratio as a function of the supply voltage V_A

gave a different zero level readout, from a minimum of $0.023\,\mu A\,cm^{-2}$ (that is 2 LSB of the last ADC) to a maximum of $0.226\,\mu A\,cm^{-2}$ (20 LSB). The cumulative supply current absorbed by the DM and by the interface board was about 180 mA.

The dependence of the readout values from the supply voltage has been found as purely proportional, as shown in Figure 4.7 plotting the ratio I_{5V}/I_{V_A} of outputs taken with the same light conditions and different supply voltages versus the supply voltage V_A. I_{5V} is measured when DM is supplied with the nominal 5 V and I_{V_A} at different voltages between 4.7 and 5.3 V. The plot shows that any variation of the voltage supply produces an equivalent variation of the response. The various colours represent different levels of light flux.

4.3.2 The automatic reading anomaly: problem and solution

During preliminary tests the Development Model behaved anomalously, when operated in automatic mode. The values reported by the GUI, from about

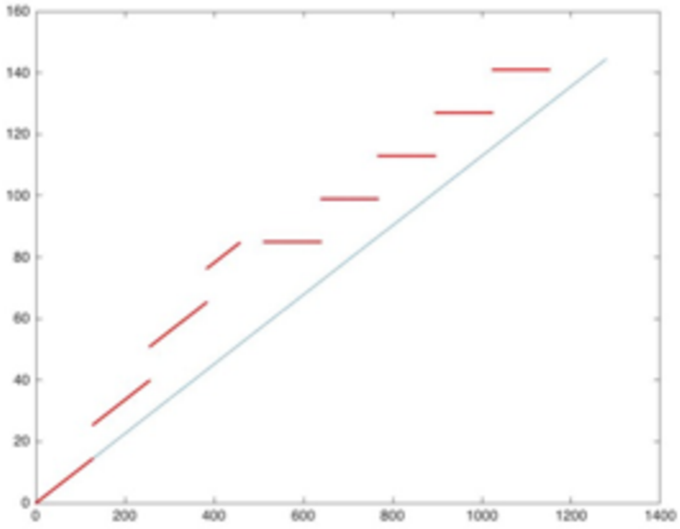

Figure 4.8: Particular: the deviation from the ideal response for the lower values 0-1280 of N(LG)

$80\,\mu A\,cm^{-2}$ to the saturation, which occurs at about $496\,\mu A\,cm^{-2}$, did not vary in a uniform way but rather assumed discreet values spaced by about $14\,\mu A\,cm^{-2}$.

The behaviour is represented graphically in Figure 4.8; shortly, apart for some details in the low end, the entire system behaved as a 5-bit ADC.

This effect was present on all the sensors with the same values and spacing. For comparison, the Evaluation Breadboard was simultaneously illuminated and it behaved as expected.

SensL, the company producer of the DM, warned about this misbehaviour, released a new version of the software application and of the FPGA VHDL code to solve the problem. The procedure for the solution of this abnormal behaviour consisted in:

1. Removing eight capacitors: C83, C84, C85, C86, C87, C88, C89, C90, to cope with timing issues.

2. Replacing the application Proba3-DM.exe with the new version 1.02.

3. Updating the *Cyclone III* FPGA with the file Proba3-1p01.pof by means of the USB-blaster and of the Quartus environment from Altera

All these actions finally made the DM working properly

4.4 STM - *Structural Thermal Model*

The Structural Thermal Model (STM) is a board, not functionally representative, whose aim is to allow mechanical and thermal analyses. The PCB contains only the few components necessary to dissipate the power allocated to SPS, has the same physical dimensions of the final flight model (FM) as detailed at the end of B phase and must be vacuum-compatible. The desired dissipation is obtained using ten 330 Ω resistor in series.

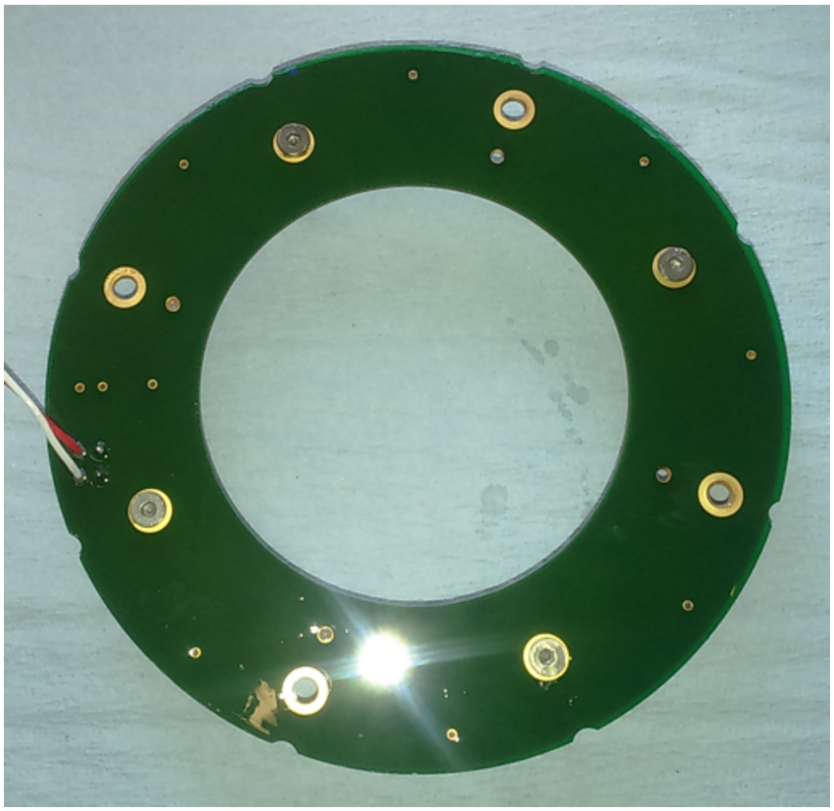

Figure 4.9: Picture of the STM PCB.

The board is realized in standard FR-4 material, free of any *silkscreen* (the characters and numbers usually written on any PCB) and treated with Arathane 5750 at INAF laboratories in Florence to obtain the vacuum compatibility. The Arathane *Conformal Coating*, used by NASA, is a transparent

bi-component adhesive avoiding outgassing and making populated PCB and components vacuum-compatible.

The STM PCB, was assembled in the STM mechanical flange described in Section 3.1.3 and subject to vibration tests at Politecnico di Milano facilities. The SPS resonance frequencies were searched before and after sine and random vibrations at various levels. The request is such that the SPS must have its first natural frequency $> 400\,Hz$, when mounted on a rigid interface (SPS-8622). The first natural frequency was found at about 1300 Hz.
The tests were successfully passed and neither the flange nor the PCB showed any damage.

4.5 Lessons learned, design changes and documents produced

4.5.1 The multiple sampling effect: running average

We investigated the influence of multiple sampling on measurements precision, performing measurements illuminating DM and EB in conjunction in the medium-high zone of the dynamic range, so to infer a general behaviour of the standard deviation as a function of the number of samples N. Figure 4.10 below shows the measured standard deviation values (in $\mu A\,cm^{-2}$) versus $\log_2$ of the number of samples N (from 1 to 1024) for three medium-high illumination levels (blue $\approx$ 1/10, red $\approx$ 1/3, green $\approx$ 2/3 of the saturation level, respectively 44, 153 and 334 $\mu A/cm^2$). Superimposed, the curve representing the ideal (theoretical) behavior of the standard deviation with respect to the number of samples N ($1/\sqrt{N}$).

The results showed that up to 128-256 averaged samples the precision of the measurements improve. As a consequence of these tests it was decided to operate a *running average* of N=256 samples on all SPS data before to pass it to the algorithm, a task that does not affect significantly the FPGA workload.

4.5.2 The power supply dependence

Another major issue identified during the tests concerned the SPS output dependence to any supply voltage noise and variation; the analyses and results contained in this section were reported in the Technical Note TN16017

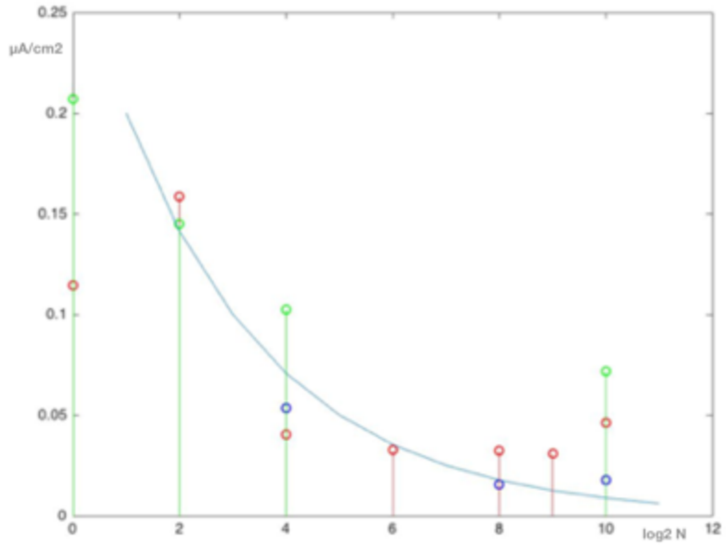

Figure 4.10: Effect of multiple sampling on the measurements taken at three different illumination levels. The blue curve is proportional to $(1/\sqrt{N})$.

[31]. The SPS output values are influenced by the voltage supply because, in the original design, the ADC and DAC were referenced directly by the supply voltage V_A that is not guaranteed to be sufficiently accurate and stable.

In this case, both the V_{DAC} pedestal and the digital readings from the ADC ($V(HG)$) depend on V_A:

$$V_{mis} = V_{DAC} + \frac{V(HG)}{10}$$

If we need a precise measurement of the light (as required by the algorithms), we cannot avoid knowing the actual value of the supply voltage with the needed accuracy comparable to 1 LSB (corresponding to 1.22 mV) because every noise contribution or fluctuation on the V_A will impact the value of the output voltage of the DAC.
The influence of an exact knowledge of the supply voltage V_A is twofold:

1. If V_A changes, the value subtracted before the last amplification stage changes accordingly:

2. The values read from the ADC are modified; in particular the digital value:

Considering both contributions, the expected dependency is inversely proportional as confirmed by the measurements of Figure 4.7:

$$V_{mis} = V_{real}\left(1 \mp \frac{\Delta V_A}{V_A}\right)$$

Possible solutions of the power supply dependence issue are:

1. Specifying tighter requirements on the power supply voltage.

2. By means of a correction at software level based on the real-time knowledge of the value of the voltage

3. Introducing a voltage reference in the design

The feasibility of the first solution contrasts with the specifications regarding the type and quality of supply voltages available for SPS at the end of phase B [50] in which the SPS receives ± 5 V supply voltage from the Power Control Unit (PCU, a subsystem of the CCB).

Assuming a voltage stability of the order of 1 LSB, the provided maximum voltage uncertainty of $100mV_{pp}$ is NOT compliant with the SPS needs and should be improved by almost two orders of magnitude.
Moreover, great care should be paid to the routing of a so accurate voltage supply from the origin in the PCU to the final destination in the SPS.

Regarding a possible software correction (representing an additional load on the computational resources), this should be based on an exact (much more precise of the expected 5% accuracy and 10 mV resolution) knowledge of the supply voltage in real-time (or quasi real-time) and this is not planned.

Finally, the adopted solution was the #3 with the adoption of the voltage reference component LM4050 from Texas Instruments (as suggested by ADC128S102QML and DAC121S101QML datasheet). This led to significant changes in design and further difficulties:

- LM4050, in its space-qualified version, is characterized by a rather bulky package (10-Lead Ceramic CLGA package). The SPS-PCB was already rather crowded and other possible substitute were just as big.

- A voltage reference needs a voltage greater than $V_{ref} + V_{drop} \gtrsim 7.5V$ to work properly. This should to be supplied in addition to the $\pm 5V$.

Nevertheless, we considered as mandatory the adoption of a voltage reference stabilizing the power supply coming from the PCU to be integrated in the SPS design and feeding the ADCs and DAC V_{ref}.
At the end it was decided to supply to the SPS PCB $\pm 12V$ instead of $\pm 5V$ and introduce LDO (Low Drop-Out) voltage regulators generating $+5V$ (and $+3.3V$ for the LVDS interfaces) on-board.

Chapter 5

The relaxation of requirements, the new design and the ADM *(Advanced Demonstration Model)*

We have seen in Section 3.3.3 how the most stringent requirement on sensitivity was the 1 mm accuracy on the longitudinal displacement, implying the need of a dynamic range equivalent to or more than 14-bit.
After thorough studies and analyses on the electronics readout performance, on the algorithm intrinsic errors and on the contribution to error given by the lack of knowledge of the illumination profile, ESA and CSL agreed to relax both requests given in requirement COR-IID-0018, namely:

1. SPS shall have a lateral measurement accuracy of $\mathbf{500\,\mu m}$ (3σ) in each axis;
2. SPS shall have a longitudinal measurement accuracy of $\mathbf{50\,mm}$ (3σ).

This relaxation, being the need of finer measurements relative only to the low-end part of the measurements, i.e. approaching the umbra, and being that the DAC and LUT round-trip added only a fictitious increasing in accuracy (due to the voltage reference issues), then it was sufficient to enhance only the part of the range close to the umbra.
The selected amount of amplification of the lower signals ($A_{HG} = \times 5$) was investigated as a compromise between region of interest to be enhanced and number of bits gained with this second stage of amplification.

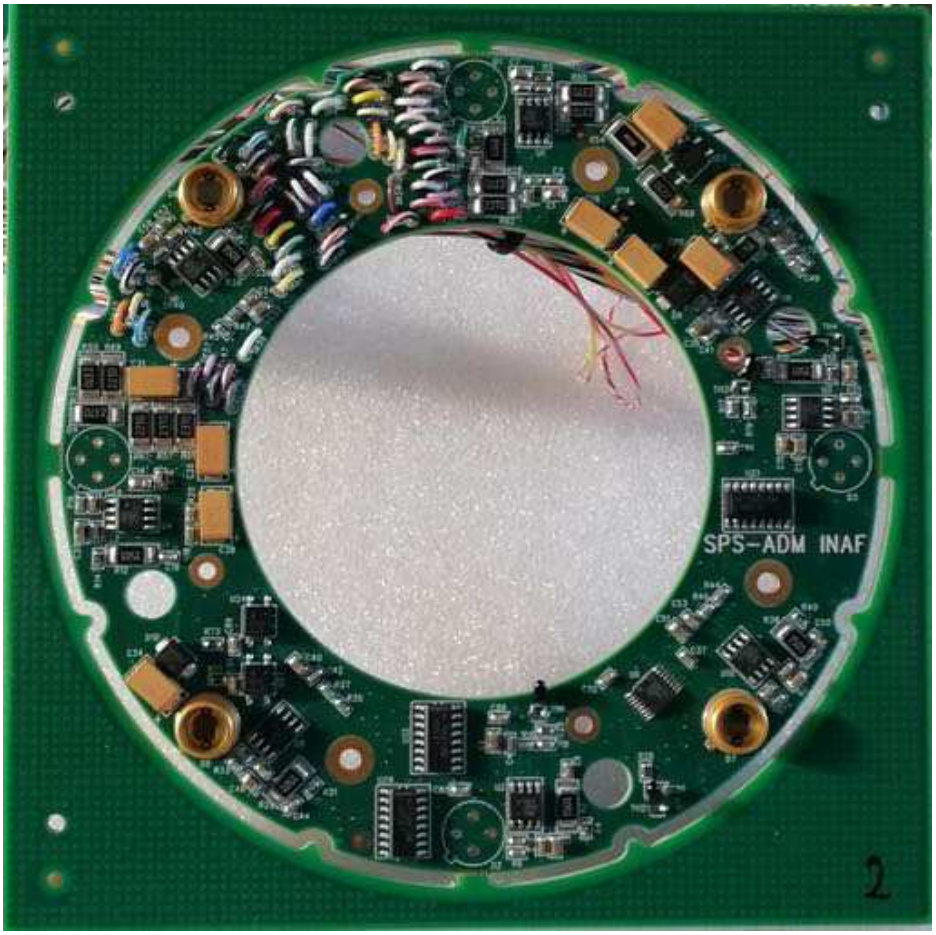

Figure 5.1: Picture of the ADM-2

Due to these and other important changes in design and requirements, the Evaluation Breadboard and the Development Model do not represent anymore the final Flight Model electronics faithfully.
For this reason, a new COTS-based (Commercial Off-The-Shelf) evaluation model (ADM *Advanced Demonstration Model*) has been produced during phase C. Images of ADM and of its GUI interface are showed in Figures 5.1 and 5.2. This model has been developed by INAF for internal use in the same period in which EQM (*Engineering Qualification Model*) was going to be produced.

INAF produced three ADM boards having the same electrical and functional characteristics of the EQM and of the FM. Minimal differences concern the usage of commercial components and some subsequent minor adaptations

of the footprints and routing. The micro-D connectors are commercial equivalent (Glenair MWDL37P-6E5-18) of the space qualified ones. In order to perform all the desired tests, the three ADM have been assigned to:

1. ADM-1: to Turin/Catania Astrophysical Observatories
2. ADM-2: to University of Florence laboratory
3. ADM-3: without connectors and SiPM, to be delivered to SensL

Initially, on the ADM-1 and ADM-2 only one set of sensors have been mounted (A set for ADM-1 and B set for ADM-2). This was done with the purpose of injecting currents directly in the amplification chain (from a few nA to 50 µA) to characterize the analog and the digital sections.

Figure 5.2: The Advanced Demonstration Model and EQM GUI main front panel.

The ADM has undergone several tests having the purpose of investigating the proper working of the new SPS design, also in comparison with DM, in particular with respect to the output dependence from the supply voltage. Additionally, the experience obtained with ADM has represented a firm base to develop the experimental set-up and define the procedures for the EQM qualification (see Chapter 6) and future FM acceptance processes.
Summarizing, the SPS-ADM was built in order to satisfy the following needs:

- New electronic design validation
- EQM and FM test set-up and procedures definition
- Interface board development (SensL) and verification of its functionalities (INAF, etc.) without any risk for EQM
- Realization of a representative electronics to be inserted in the data chain described in Section 7.2.

Figure 5.3: ADM/EQM/FM FPGA interface board

5.1 Design changes

The original SPS electronic design solution proposed by SensL [6] [5] has been deeply modified[1] in order to change (and simplify) the design still covering

[1]This section has been written as part of "SPS: a trade-off study on dynamic range and sensitivity", technical note [30]

the *goal box* region with an appropriate margin, and taking into account also the introduction of the bandpass 500-660 nm filter. Additional improvements regarded the adoption of high accuracy (0.01%) and low TCR (Thermal Coefficient of Resistance, 5 ppm/°C max) resistors, the change of the OpAmp model and the suppression of the second amplification stage. Summarizing, the main changes in the electronics are:

1. The system has now only two stages whose gains are $A_{TIA} = 100\,kV/A$ (transimpedance amplifier, low-gain) and $A_{HG} = 5$ (non-inverting amplifier, high-gain).

2. The OpAmp component has been changed to the LMP2012QML (Texas Instruments) that has lower noise, in particular in terms of I_B bias current (-3 pA)

3. The voltage reference component LM4050 (0.1% initial accuracy) has been added to reference ADC and feed OpAmps.

The overall final design is shown in the charts of Appendices from A.2 to A.4. A detail of the amplification stage for one sensor is shown in Figure 5.4.

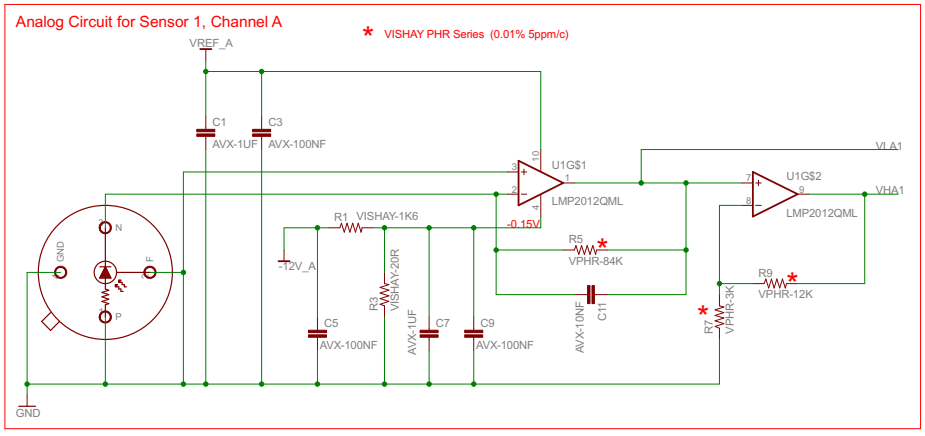

Figure 5.4: The amplification chain of one SiPM (current design)

Other important changes with respect to Phase B design are:

- introduction of a power-supply switching section based on opto-isolated devices as Solid State Relays (SSR) and optocouplers, in order to comply with Single Point of Failure (SPF) requirement (COR-IID-3007) and fault back-propagation to CCB concerns;

- generation of secondary voltages on-board as a consequence of the voltage reference introduction;
- adoption of differential signals for transmission (LVDS, Low-Voltage Differential Signaling) in order to meet ESA requests, and, consequently:
- change of the Micro-D connector pin-count (37 pin).

Range and sensitivity

For SPS, the most important constraint concerning the range derives from the requirement COR-IID-3005 establishing the condition of non-saturation for the measurements performed inside the *goal box*.
Setting the value of R_F (the feedback resistor of the Trans-Impedance Amplifier) to 100 kΩ, we obtain a margin between the *goal box* lateral limit (125.7 mm) and the saturation, that occurs at about 175 mm. This means a headroom of about 85% in terms of signal levels (irradiance or current) and 40% in terms of lateral movement.

The second stage (high-gain) allows us to obtain an improved resolution for the lowest signal levels. In fact, one LSB (Least Significant Bit) at the output of the high gain stage corresponds to an input of 2.44 nA instead of 12.2 nA (low-gain). The measurements done are described in Section 3.3.3.

With reference to the variation of DNs expected for the minimum lateral displacement of 50 µm given in Figure 3.14, we conclude that inside the *requirement box* the system provides a sensitivity sufficient to obtain the desired measurement accuracy.

High-gain to low-gain threshold

The output of the SPS system consists in digital number in the range [0:20475], because the low-gain readings are multiplied ×5 in order to make them comparable to the high-gain data.
Being that the output value is subject to a running average operation (performed on a number N=256 of samples), as described in Section 4.5.1, the problem arises in choosing a threshold for triggering from high-gain to low-gain values that should not be exactly 4095 (in this case, we could obtain an incorrect average for a growing signal).

We have calculated the threshold considering: a readout window of 100 ms (COR-IID-7002), a maximum relative velocity of 1 mm/ sec in the requirement box (COR-IID-7068) and the highest readouts in the high-gain mode in *requirement box* (2600 DN). At the end, the threshold has been conservatively fixed at 4000 DN.

To recap, when the high-gain output is in the range [0:4000] DN the SPS algorithm receives the high-gain data; if the high-gain output is > 4000 the algorithm will receive the low-gain output after a $\times 5$ multiplication operated by the FPGA inside the CCB. By consequence, the full range is sampled at different quantization steps: from 0 to 4000 there are 1 bit steps (high-gain) and from 4000 to 20475 data progress in 5 bits steps (low-gain).

5.1.1 Voltage reference

As a feedback of the DM tests and numerical model analyses illustrated in Section 4.5.2, CSL provided new power supply requirements:

Req. ID	Req. Text	Verif. Meth.
SPS-6420	The SPS shall be power supplied using $\pm 12V$ input voltage with a common return line. The common return line shall be the zero volt reference of the SPS (GND-SPS). (created)	D
SPS-6421	The SPS shall remain operational without performance degradation all along the following input voltage ranges: MIN (V) TYP (V) MAX (V) +11.50 +12 +12.50 (created). -13 -12 -11	D, T
SPS-6423	The SPS shall remain operational without performance degradation while the input voltages are submitted to some output ripple up to $500\,mV_{pp}$ (10 kHz - 2 MHz). (created)	D, T

Note how the adoption of the voltage reference on-board allows to obtain the required performance also with a rather large interval in supply voltage value and ripple ($500\,mV_{pp}$ instead of $100\,mV_{pp}$).

Obviously, this change impacted on the power budget, but we must also consider that, at the origin, the $\pm 5V$ supply voltages were derived on the

PCU from $\pm 12V$ using linear regulators as well, then the rising of power consumption on the SPS-PCB is compensated by a lower consumption on the PCU.

The original power budget allocated for SPS was 0.75 W plus a 20% margin, that is 0.9 W, but considering a DC/DC conversion efficiency ($\approx$ 75%) at system level, the consumption sums up to 1.22 W.

3.3V LDO - *Low Drop-Out* regulator

A *worst-case analysis* (WCA [38]) was performed in order to guarantee that the circuit shown in Figure 5.5 could operate both in normal conditions and in case of failure (VRG8660 LDO short circuit). In case of normal

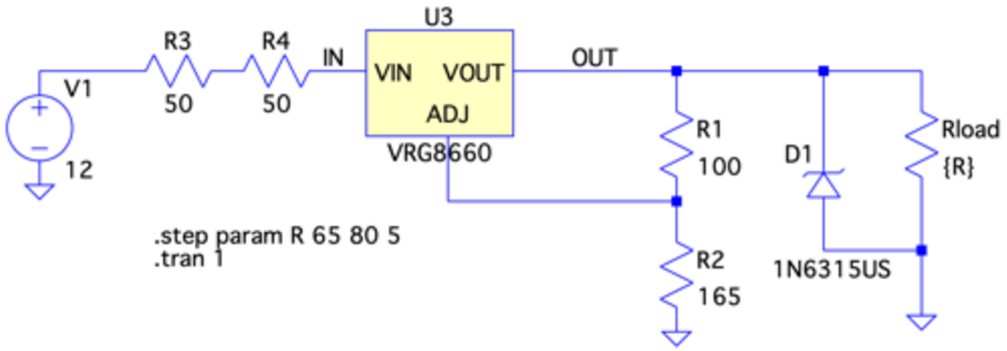

Figure 5.5: The scheme of the overvoltage protection comprising the current limiting resistance, split over two resistors, and the Zener diode D1.

operations, two series 50 Ω resistors limit the current up to the maximum voltage drop still permitting to the voltage regulator to correctly work in worst case conditions. We used two resistors to better dissipate the maximum heat and, at the same time, comply with ECSS derating.

With these values of the components the voltage drop across the resistors is always above the voltage drop of the regulator plus the maximum output voltage, so ensuring proper operation. In case of failure, instead, the circuit can withstand the regulator short circuit current in a permanent way without failure propagation to the transmitters lines.

5.1.2 Differential transmission

ESA required to realize all data interconnections realized in LVDS technology, using components with *failsafe* functionality.
ECSS-E-ST-50-12C (SpaceWire - Links, nodes, routers and networks) defines the *failsafe* operation as "the condition in which the receiver output goes to the high state (inactive) whenever: the receiver is powered and the driver is not powered, or the inputs are short circuited, or input wires are disconnected".
The same document lists the conditions that must be satisfied for *failsafe* operation of LVDS signals. All these cases have been considered when planning SFT (Short Functional Tests) and FFT (Full Functional Tests) for the ADM and the EQM (refer to Section 6.4).

In the table below the requirements applicable to signal transmissions are listed:

Req. ID	Req. Text	Verif. Meth.
SPS-6510	Any communication line implemented for performing the control and the data acquisition of the SPS shall be LVDS (3.3 V). (parent: EMC-39)	D
SPS-6512	The SPS and the control unit must not have their communication line references connected directly through the electrical interface but shall however remain operational without performance degradation with $\pm 1V$ of common-mode applied between both references.	D, T

The introduction of this type of transmitters and receivers made it necessary to generate 3.3 V on-board, by means of Cobham VRG8660 linear regulators.

5.1.3 Power switching section

Other requirements relevant to power supply, beside the ones cited in Section 5.1.1, are:

Req. ID	Req. Text	Verif. Meth.
SPS-6412	The SPS shall survive without any degradation to any accidental simultaneous power ON, data acquisition and control from both of its nominal and redundant electrical interfaces. (parent: GERS-87)	D, I, T
SPS-6514	Eventual digital input control lines shall be galvanically isolated using photodevices. Note: the CCB shall provide digital signals using open-collector circuitry with 5 V common bias. The 5 V is not available to the SPS for other functions and must not be referenced to SPS-GND (different ground domain). (created)	D, T

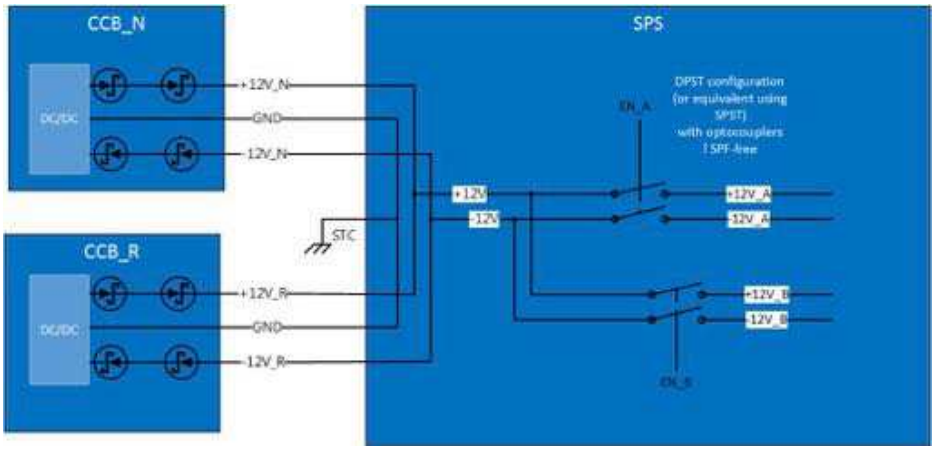

Figure 5.6: Simplified scheme of the power switching section.

An all new optically isolated section (see Figures 5.6 and 5.7) was designed using Solid State Relays to switch on and off sections A and B with supply power coming from either nominal or redundant CCB (the occurrence of contemporary ON of both CCB was explicitly excluded from CSL side). In addition to SSR, there is a set of optocouplers used to put in *idle* state the unused transmitters and receivers. Both types of components, SSR and optocouplers are enabled/disabled by a separate, active-low, circuit operating with a +5 V bias voltage and a different ground reference.

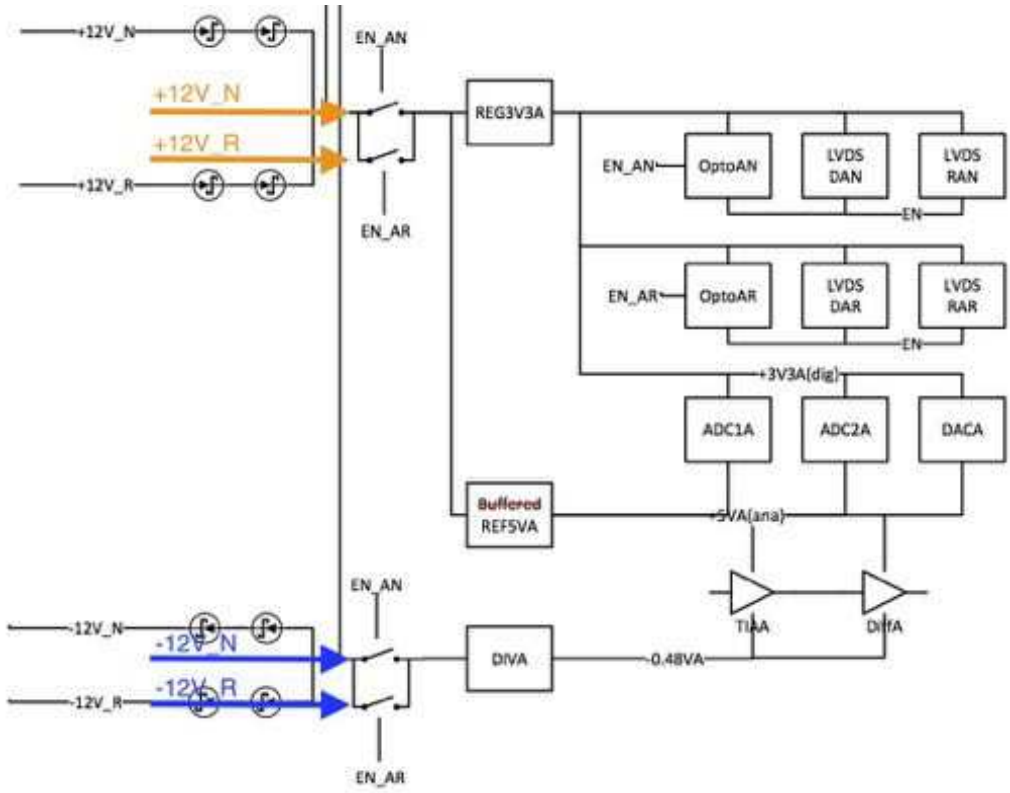

Figure 5.7: Scheme of the power switching section

5.1.4 Bandpass filter optimization

In Section 3.2.1 we have seen that integration over the whole visible spectrum, where the SPS responsivities are larger than zero, will give two major problems for the SPS calibration:

- Temperature dependence: Being that for $\lambda > 660\,nm$ the SPS responsivity changes significantly with the sensor temperature, provided that SPS algorithm does not have the possibility to apply a real-time correction for temperature, we observe the minimum responsivity percentage variation in the range between 200 nm and 680 nm.

- On the opposite side of the spectrum, for $\lambda < 500\,nm$ the limb darkening coefficients (u_λ and v_λ) are not constant and depend on the wavelength. Then, the K conversion parameter (Equation 3.4 in W/A or, equivalently, W/DN) would depend on the transverse displacement within the penumbra we are considering. This would make impossible

to perform a real in-flight calibration of SPS with DNs measured in full Sun with known irradiance, because otherwise the W/DN conversion factor could be different from the one relative to the SPS located at the nominal position in the penumbra at 55 mm from the telescope optical axis.

5.2 Electrical interfaces

The SPS PCB is connected to the CCB by means of two *pigtail* 37-pin micro-D connectors (Axon model MDSA537PV01301L30B). The wires free sides are glued and soldered to the PCB according to ECSS-Q-ST-70-08C specifications (see Figure 5.8).

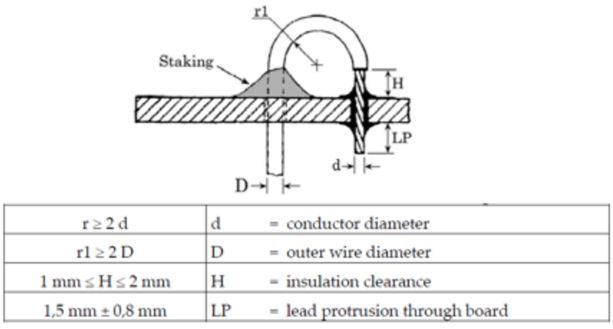

r ≥ 2 d	d	= conductor diameter
r1 ≥ 2 D	D	= outer wire diameter
1 mm ≤ H ≤ 2 mm	H	= insulation clearance
1,5 mm ± 0,8 mm	LP	= lead protrusion through board

Figure 5.8: Method of *strain relief* as prescribed by ECSS-Q-ST-70-08C

The signals running through the harness between SPS and CCB should be routed separately depending on their EMC classification (SPS-8659):

1. Power lines and any analogue signals whose current is greater than 50 mA.
2. Analogue signals (analogue telemetry, temperature sensors etc.).
3. Digital signals.
4. RF signals (not applicable to SPS).
5. Power/control lines to pyro (not applicable to SPS).

In our case it was extremely unpractical (and never planned) to route power and digital signals on separate bundles. It must also considered the fact that

typical current flowing at +12V is about 45 mA for each SPS section.
For these reasons we made the choice to "segregate" signals at connector level separating with unused pins the $\pm 12\,V$ power lines and $+5\,V$ (enable bias) from digital signals.

Concerning the grounding principle of CSC spacecraft it is required that: "the spacecraft structure shall be the 0 V ground reference. All primary power return lines shall be grounded to the spacecraft structure".

5.3 ADM Electrical and functional tests

5.3.1 Experimental setup

The experimental setup is analogue to the one used for the EQM described in Section 6.4.1 except for the fact that the ADM does not have cleanliness requirements.

5.3.2 FFT - *Full Functional Tests*

The Full Functional Test is a series of electrical tests that can be performed with the basic instrumentation usually present in a generic electronics laboratory with and without the use of the FPGA interface board (see Figure 5.3).

After visual inspection and dimensional check (inner and outer diameters, thickness, weight and mounting holes), the connections are verified using the pinout of figure in Appendix A.15 for conformance. The rest of the FFT is listed in Table 5.1.

5.3.3 SFT - *Short Functional Tests*

The Short Functional Test, listed in Table 5.2, is a subset of FFT aiming to determine quickly the correct operation of the SPS electronics in all his parts (acquisition, digitization and transmission) with or without the need of the FPGA interface board and also with the PCB mounted in the flange or after conformal coating. In these cases, in fact, the secondary voltages cannot be probed and the PCB cannot be imaged with the IR camera.

Test	Description	Acceptance criteria	Notes
Continuity	Continuity between grounds	Resistance $<2\,\Omega$	Between GND pins and PCB GND pad
High resistance Enable	Optical devices producing proper I/O isolation	Resistance $>100\,\mathrm{M}\Omega$	Between connectors pins showing a virtually infinite resistance.
High resistance primary voltage	Nominal and Redundant $\pm 12V$ power lines are galvanic isolated	Resistance $>100\,\mathrm{M}\Omega$	No back-propagation of failures to CCB
Receivers input resistance	Check the correct value for termination resistances	Resistance: $100 \pm 10\ \Omega$	Failsafe function not testable for RX
Transmitters failsafe isol.	Check failsafe function for TX	Resistance $>100\,\mathrm{k}\Omega$	When TX is not powered
Primary voltage switching	$\pm 12V$ present when ON	Voltage: $+12 \pm 0.5$ V -12 ± 1 V	Before conformal coating
Secondary voltage (3.3 V)	$3.3V$ present when ON	Voltage $= 3.3 \pm 0.3$ V	Before conformal coating
Secondary voltage (5 V)	Reference voltage present when ON	Voltage $= 5 \pm 0.05$ V	Before conformal coating
Secondary voltage OpAmp V^-	OpAmp negative supply voltage present when ON	Voltage $= -0.15 \pm 0.015$ V	Before conformal coating
Primary currents	Verify the max currents sourced from $\pm 12V$	+12V: $<70\,\mathrm{mA}$ -12V: $<30\,\mathrm{mA}$	For each channel channels enabled
Power		Power $<900\,\mathrm{mW}$ per channel	1 or 2 channels enabled
Thermal	Identify hot spots using IR thermal camera	Temperature $<85\,^\circ\mathrm{C}$	On a part-by-part basis
Sensors functional and performance tests	Sensors are illuminated with various levels from dark to saturation	$\Delta DN < 2\%$	Constant source. Also small variations around nominal values.
Temperature readout test	Check thermistors R/O	ΔT $<0.5\,^\circ\mathrm{C}$	

Table 5.1: FFT, Full Functional Test description.

Category / Test	Acceptance criteria	Notes
Continuity	Resistance $<2\,\Omega$	Only between GND pins
High resistance Enable	Isolation $>100\,\mathrm{M}\Omega$	Between connectors pins
High resistance primary voltage	Isolation $>100\,\mathrm{M}\Omega$	Between connectors pins
Primary currents	$+12\,\mathrm{V}$: $<70\,\mathrm{mA}$ $-12\,\mathrm{V}$: $<30\,\mathrm{mA}$	Requires wire break-out
Sensors functional and performance tests	$\Delta DN < 2\%$	
Temperature R/O test	ΔT $<0.5\,^{\circ}\mathrm{C}$	

Table 5.2: SFT, Short Functional Test content.

5.4 Conclusions and documents produced

The documents described below, Part Stress Analysis, Worst-Case Analysis and Failure Modes Effects Analysis are documents necessary for the Critical Design Review finalization. They were redacted by me in autonomy or in cooperation (WCA) and finally included in the CDR data-pack.

5.4.1 PSA - *Part Stress Analysis*

The technical note P3-INF-TN-17021 contains the SPS Part Stress Analysis. The objective of this analysis is to demonstrate the compliance of the SPS circuit to the *derating* rules of ECSS-Q-30-11C, which have been applied in order to guarantee EEE (Electrical, Electronic, and Electromechanical) parts reliability and the system performance up to its end of life. In the document every component is listed with an indication of its operational limits highlighting any potential condition of overstress. The derating procedure is useful to increase the margin of safety between the operating stress level and the actual failure level for the part, providing additional protection from system anomalies unforeseen by the designer.

The main environmental variables to which the SPS system is subject and that are applicable to the Part Stress Analysis are:

1. Power supply variations (Section 5.1.1)

2. The ambient temperature derived from the thermal analysis as described in document [46].

3. Time of mission, from Beginning Of Life (BOL) to End Of Life (EOL).

4. Radiation (Section 2.3).

The power dissipated by each component has been calculated when the component is running according to the average power included in the thermal analysis; additionally, we have considered the components self-heating calculated considering the flowing current and the thermal resistance.

The SPS has been designed to cope with the in-flight radiation environment as specified in SPS requirements specification [50]. In the table of Appendix A.7, for each component, the SMD (Standard Micro Drawings) containing the relevant information with regard to radiation hardness are indicated.

The Part Stress Analysis has been performed, applying at part level and in the nominal conditions the limits and load ratios of the appropriate parameters specified in ECSS-Q-30-11C (different for each type of component, usually one or more of: voltage, current, power and temperature) in order to reduce the stress applied to components.

The PSA outcome consists in an introductory document and in an attached Excel file containing the stress analysis and composed of six tables (see Appendices from A.8 to A.11) divided between:

1. Resistors

2. Capacitors

3. All other components

The information contained is detailed for each component that is uniquely identified by a reference identifier (R, C, D, U etc.) and by its part number. Components subject to similar stress conditions are grouped for sake of simplicity.

For each parameter to be derated (voltage, current, power etc.) are computed:

1. Derating factor to be applied at that particular type of component, as specified by ECSS standard.

2. Maximum allowable value for that parameter applying the derating factor.

3. Case or package maximum temperature.
4. Maximum parameter value resulting from analysis.
5. Stress Ratio: i.e. the ratio between actual and maximum allowable values.
6. Compliance statement with respect to applicable derating requirements.

Regarding the statement of compliance we must observe that the PSA was not simply a tool used for a final *assessment* of the design, but, rather it has been used as an instrument to recursively identify weak points (e.g. the two limiting resistors in Section 5.1.1) in design that needed modifications or change of components. This is the reason why, necessarily, at the end all items resulted compliant.

5.4.2 WCA - *Worst Case Analysis*

The Worst Case Analysis (P3-INF-RP-17021) has been co-authored with the industry (OHB Firenze). The worst-case effects on V(LG), V(HG) and V(ref) of all the following parameters, using the Root Sum Square (RSS) method have been evaluated:

- Nominal value dispersion
- Thermal drift
- Ageing
- Radiation effects

At mission beginning, the ageing and radiation will not affect the parameters yet and the initial deviations with respect to the nominal values can be calibrated on-ground. Then, the only drift that influences the system behaviour at BOL is the changing in temperature inside the operational range ($35 \pm 6\,°C$) plus the qualification range ($\pm 10\,°C$).
For the parts sizing, an EVA (Extreme Value Analysis) criterion was rather adopted.

The following conclusions were drawn:

1. For both circuits, low and high gain, the contribution to output error is negligible with respect to the ADC LSB.

2. The LM4050 voltage reference effect on the global error is negligible with respect to the ADC LSB.

3. The analog chain noise is not negligible with respect to the ADC LSB, but it could be averaged by software to lower it under the LSB threshold (the OpAmp has a flat spectral density with reduced 1/f noise; the limit in noise reduction is given by the photodiode 1/f noise).

4. The major error contributions are due to the ADC errors.

5.4.3 FMEA - *Failure Mode Effect Analysis*

The Technical Note P3-INF-TN-17025 contains the results deriving from the Failure Modes and Effects Analysis that I drew in accordance with the guidelines given in ECSS-Q-ST-30-02C.

The FMEA purpose is to identify all failures and modes of failure that can occur at component level and to investigate the final effects on the SPS system, as well as the possible failure prevention and compensation methods.

Preliminary, I assigned a severity category to the consequences of each failure mode according to Table 5.9. This value reflects the severity of the observed effects on the whole SPS system deriving from each component potential failure. Although SPS is a subsystem with dependances from other complex devices (e.g. CCB), I identified a case in which a SPS failure could back-propagate to other systems (the CCB itself), so deserving a class 2 severity (see Table 5.10).

I started the FMEA performing a functional breakdown organized as a block diagram and on this basis it was given an unique numbering (5-digits) for each block. In the figures of the Appendices A.12 and A.13 we show the functional splitting of the SPS design. Each component composing the block was listed in the worksheet, where the components common to other blocks were written in bold.

In the FMEA worksheets we reported all possible failures for each component, their consequences and severity and the mitigating actions. FMEA analysis final outcome comprehend 48 tables with hundreds of entries, more than the total number of parts, considered that each component can have one or more failure modes. For every fault case it is indicated one or more corrective action.

Table 4-1: Severity of consequences

Severity category	Severity level	Description of consequences (failure effects)	
		Dependability effects (as specified in ECSS-Q-ST-30)	**Safety effects (as specified in ECSS-Q-ST-40)**
Catastrophic	1	Failure propagation (refer to 4.2c)	Loss of life, life-threatening or permanently disabling injury or occupational illness.
			Loss of an interfacing manned flight system.
			Severe detrimental environmental effects.
			Loss of launch site facilities.
			Loss of system.
Critical	2	Loss of mission	Temporarily disabling but not life-threatening injury, or temporary occupational illness.
			Major detrimental environmental effects.
			Major damage to public or private properties.
			Major damage to interfacing flight systems.
			Major damage to ground facilities.
Major	3	Major mission degradation	
Minor or Negligible	4	Minor mission degradation or any other effect	

Figure 5.9: Failure severity levels as defined in ECSS-Q-ST-30-02C.

FMEA identified 8 failure modes, similar to each other, having severity class 2SP (critical and Single Point of Failure) occurring when set A and B cannot be enabled from CCB Nominal but only from CCB Redundant (and vice-versa). The compensating provision being: switching to CCBR (CCBN), if permitted.

Hazard analysis spotted 2 failure modes (classified with 2SH) that could potentially lead to safety consequences: a short-circuit between IN and OUT pins in 3.3VA (and 3.3VB) linear regulator (VRG8660). The risk for safety consists in the possible leakage of +12 V from the line feeding the linear regulator to its output.
This voltage would be present directly to the receivers/transmitters inputs, possibly returning to CCB (both Nominal and Redundant!) by means of the transmission lines, then representing a severe risk for the mission itself.

The compensating provision consists in the protection circuit of Figure 5.5 composed of the current limiting resistor(s) before the input of the regula-

Severity category	Severity level	Description of consequences (failure effects)	
		Dependability effects	End effects
Catastrophic	1	NA	
Critical	2	Failure propagation to other systems. Necessity to switch on Nominal or Redundant CCB in order to operate SPS.	Permanent failure to N CCB or R CCB
			Set A and B cannot operate from N CCB
			Set A and B cannot operate from R CCB
Major	3	Loss of set A. Non-feasibility of in-flight calibration. Loss of mission's capability to reach desired formation-flying performances.	Loss of set A
			Loss of set A HG values
			Non-feasibility of in-flight calibration
Minor or Negligible	4	Necessity to switch to Nominal or Redundant CCB in order to perform in-flight calibrations. Minor mission degradation or any other effect	Set A or B cannot operate from N CCB
			Set A or B cannot operate from R CCB
			Loss of set B
			Loss of set B HG values

Figure 5.10: Severity of consequences applied to SPS sub-system.

tor (limiting the input voltage up to $V_{in}(min) = 3.3\,V + V_{drop}(max) = 4.8\,V$) and a Zener diode at the output in order to maintain the final voltage inside the absolute maximum rating of the transceiver (4.8 V reducing to 4.32 V if we consider a 90% *derating*).

5.4.4 *SPS Error Budget*

The Technical Note P3-INF-TN-15012, containing the Error Budget Analysis for the SPS subsystem, needed to be updated in consequence of several analyses and changes in design. I contributed in particular to the part concerning the electronics. This document begins describing the transfer function that returns the position of the ASPIICS entrance pupil center with respect to the penumbra profile center at the nominal inter-satellite distance, ISD. From this analytical expression the SPS signal error can be translated into the error of the entrance pupil position returned by the metrology algorithm. Every source of error of the SPS signal is identified, given an estimate and used to derive their contribution to the entrance pupil position error.

Radiometric & variability of sources

The dominant contribution to the error in the signal of the solar penumbra profile is the term given by the difference between real solar penumbra profile and the one based on numerical simulations and on-ground calibrations. Its

value, for the lateral error, sums up to 600 µm inside the *Requirement Box* and up to more than 3 mm in the *Goal Box*. In order to reduce this error to the level for which the algorithm will return the penumbra position with the required accuracy, the real penumbra profile must be calibrated in-flight.

The contribution of diffraction caused by the occulter edge σ_{DIFF} is calculated for the case of a toroidal shape and the diffraction curve is used in place of the geometrical one.

Mechanical

We have considered all the tolerances in SPS manufacturing and positioning as well as the tolerances on the COB on which SPS is mounted.

manufacturing of the M4 holes for SPS fixation on COB	0.05 mm
positioning of the fixation holes on the COB	0.05 mm
alignment pin holes positioning	0.05 mm
COB length	0.05 mm
pupil diameter	0.02 mm

Table 5.3: Mechanical tolerances.

We considered the total budget for the alignment of the SPS-flange with the optical tube, the front door and with the electronic board (SPS-PCB). We concluded that the maximum alignment budget that can be allocated for the SPS subsystem is $\leq 93\mu m$. Anyway, this misalignment can be calibrated and most of it converge in the σ_{PFC} residual and in the individual k_i sensor parameters. The thermal expansion cannot be calibrated, but being mostly symmetrical it gives a negligible contribution to the lateral error. On the contrary, it represents a bias for the longitudinal error and contributes a maximum of 1.8 mm to it.

Electronics

Electronics contribution to error budget is negligible, consisting essentially in the quantization error. This is due to the fact that the original design was conceived to comply with requirements that were 10 or 50 times more challenging than the current ones.

In case of a periodical (3 months) calibration, the maximum residual lateral error given by the sensor and the electronics is:

$$\sqrt{\sigma_{RT}^2 + \sigma_{PFC}^2 + \sigma_{CAL}^2} = 21\,\mu m$$

At BOL, just after the initial calibration, this term sums up to only 5 µm. A similar calculation gives, for the longitudinal error, respectively 4.3 mm and 1 mm.

Calibrations

At the end of the on-ground calibration activities, the residual σ_{PFC} has been quantified in 5 µm (1 mm longitudinal).
For the in-flight calibration, we considered an initial commissioning campaign to be completed within $\leq$ 1 month and that further calibration campaigns will occur with time intervals $\leq$ 3 months. The residual is computed in σ_{CAL} and sums up to 21 µm (4.3 mm longitudinal).

5.4.5 Error Budget conclusions

The final Table 5.6 presents the lateral and longitudinal total errors inside the *requirement box* in the four cases:

1. at beginning of life, before the first in-flight calibration, not having a proper knowledge of penumbra profile;
2. at beginning of life, just after the first in-flight calibration;
3. during the mission in case of an in-flight calibration every 3 months;
4. at end of life in case the in-flight calibration was never performed.

We can conclude that it is mandatory to perform calibration campaigns in-flight with the following purposes:

- Initially, to explore the penumbra and obtain a realistic profile to be used as a model and to re-calibrate sensors and electronics individually.
- Periodically, to keep under control drifts in electronics and sensors due to ageing and radiation.

In all cases, it should be kept in mind the important contribution of sunspots that could be corrected using Sun observations from Earth.

Contribution and Symbol	Estimated Error (µm) (or included in:)	Notes
Uncertainties on the penumbra profile (diffraction σ_{DIFF} + limb darkening coeff. variat. σ_{LDCV})	600	Bias, 600 µm is the maximum value inside the Req. Box.
Earth albedo σ_{EA}	Negligible	Same bias on all sensors, time dependent
Sun spots σ_{SUNSP}	215	Bias on one or two sensors, time dependent
SPS mechanical alignments $\sigma_{SPS-COB}$, σ_{SPS-BF} etc.	σ_{PFC}	To be measured and included in σ_{PFC}
SPS Flange thermal expansion $\sigma_{SPSF-TE}$	Negligible	Bias, only asymmetric expansions
EO shape σ_{EOS}	10	Bias, only for edge irregul. $\leq 31\,mm$ and non circularity (residual error of the roll operation)
EO Tilt σ_{EOT}	Negligible	tilt <5°
Diode Responsivity variation with temperature σ_{RT}	1	0.1 DN (81 °C)
Diode Responsivity variation with radiation/aging σ_{RRA}	σ_{CAL}	Included in single sensor proportional factor. Residual in σ_{PFC} and σ_{CAL}
Initial offset (V_{OS} I_B etc.)	σ_{PFC}	Included in single sensor offset. Residual in σ_{PFC}
Offset drift due to radiation/aging (I_B)	Negligible	
Initial proportional (Amplifiers, voltage ref etc.)	σ_{PFC}	Included in single sensor proportional factor. Residual in σ_{PFC}
Proportional drift due to radiation/aging	σ_{CAL}	Included in single sensor proportional factor. Residual in σ_{CAL}
Quantization error	0.6	
ADC INL σ_{INL}	9	Integral Non-Linearity
Algorithms $\sigma_{AlgoLat}$	54	Bias, 54 µm is the maximum value at the corners of the Req. Box
On-ground calibration residual σ_{PFC}	5	
In-flight calibration residual σ_{CAL}	21	Random, allocated budget for the residual error of the in-flight calibration. EOL without any calibration = 160

Table 5.4: Lateral error budget allocation

Contribution and Symbol	Estimated Error (µm) (or included in:)	Notes
Uncertainties on the penumbra profile (diffraction σ_{DIFF} + limb darkening coeff. variat. σ_{LDCV})	120	Bias, to be reduced by means of in-flight calibrations
Earth albedo σ_{EA}	1	Bias
Sun spots σ_{SUNSP}	22	Bias on one or two sensors, time dependent
SPS mechanical alignments $\sigma_{SPS-COB}$, σ_{SPS-BF} etc.	σ_{PFC}	To be measured and included in σ_{PFC}
SPS Flange thermal expansion $\sigma_{SPSF-TE}$	1.8	Bias, time dependent. Symmetric and asymmetric contributions
EO shape σ_{EOS}	22	Bias, residual error of the roll operation
EO Tilt σ_{EOT}	Negligible	tilt <4°
Diode Responsivity variation with temperature σ_{RT}	0.2	0.1DN (81 °C)
Diode Responsivity variation with radiation/aging σ_{RRA}	σ_{CAL}	Included in single sensor proportional factor. Residual in σ_{PFC} and σ_{CAL}
Initial offset (V_{OS} I_B etc.)	σ_{PFC}	Included in single sensor offset. Residual in σ_{PFC}
Offset drift due to radiation/aging (I_B)	Negligible	
Initial proportional (Amplifiers, voltage ref etc.)	σ_{PFC}	Included in single sensor proportional factor. Residual in σ_{PFC}
Proportional drift due to radiation/aging	σ_{CAL}	Included in single sensor proportional factor. Residual in σ_{CAL}
Quantization error	0.1	
ADC INL σ_{INL}	0.2	
Algorithm $\sigma_{AlgoLon}$	6	Bias, 6 mm is the maximum value at the corners of the Req. Box
On-ground calibration residual σ_{PFC}	1	
In-flight calibration residual σ_{CAL}	4.3	Random, allocated budget for the residual error of the in-flight calibration. EOL without any calibration = 32

Table 5.5: Longitudinal error budget allocation

Total lateral error in absence of sunspots		
BOL no calib.	$\sqrt{\sigma_{DIFF}^2 + \sigma_{LDCV}^2 + \dots} + \sigma_{AlgoLat} + \dots = 655\,\mu m$	Without proper knowledge of penumbra profile
BOL	$\sqrt{\sigma_{AlgoLat}^2 + \sigma_{PFC}^2} = 54\,\mu m$	Largest contribution due to algorithm
3 months	$\sqrt{\sigma_{AlgoLat}^2 + \sigma_{PFC}^2 + \sigma_{CAL}^2} = 58\,\mu m$	Largest contribution due to algorithm
EOL no calib	$\sqrt{\sigma_{DIFF}^2 + \sigma_{LDCV}^2 + \dots} + \sigma_{AlgoLat} + \sigma_{EOL} = 815\,\mu m$	Largest contribution due to lack of calibrations
Total lateral error in presence of sunspots		
BOL no calib.	$\sqrt{\sigma_{DIFF}^2 + \sigma_{LDCV}^2 + \dots} + \sigma_{SUNSP} + \dots = 870\,\mu m$	Without proper knowledge of penumbra profile
BOL	$\sqrt{\sigma_{AlgoLat}^2 + \sigma_{PFC}^2} + \sigma_{SUNSP} = 270\,\mu m$	Largest contribution due to sunspots
3 months	$\sqrt{\sigma_{AlgoLat}^2 + \sigma_{PFC}^2 + \sigma_{CAL}^2} + \sigma_{SUNSP} = 274\,\mu m$	Largest contribution due to sunspots
EOL no calib	$\sqrt{\sigma_{DIFF}^2 + \sigma_{LDCV}^2 + \dots} + \sigma_{SUNSP} + \dots \approx 1\,mm$	Largest contribution due to lack of calibrations
Total longitudinal error in absence of sunspots		
BOL no calib.	$\sqrt{\sigma_{DIFF}^2 + \sigma_{LDCV}^2 + \dots} + \sigma_{AlgoLon} + \dots = 144\,mm$	Without proper knowledge of penumbra profile
BOL	$\sqrt{\sigma_{AlgoLon}^2 + \sigma_{PFC}^2} = 6\,mm$	Largest contribution due to algorithm
3 months	$\sqrt{\sigma_{AlgoLon}^2 + \sigma_{PFC}^2 + \sigma_{CAL}^2} = 10\,mm$	Largest contribution due to algorithm
EOL no calib	$\sqrt{\sigma_{DIFF}^2 + \sigma_{LDCV}^2 + \dots} + \sigma_{AlgoLon} + \sigma_{EOL} = 176\,mm$	Largest contribution due to lack of calibrations
Total longitudinal error in presence of sunspots		
BOL no calib.	$\sqrt{\sigma_{DIFF}^2 + \sigma_{LDCV}^2 + \dots} + \sigma_{AlgoLon} + \sigma_{SUNSP} + \dots = +144\,mm\ -166\,mm$	Bias
BOL	$\sqrt{\sigma_{AlgoLon}^2 + \sigma_{PFC}^2} + \sigma_{SUNSP} = +6\,mm\ -28\,mm$	Largest bias due to sunspots
3 months	$\sqrt{\sigma_{AlgoLon}^2 + \sigma_{PFC}^2 + \sigma_{CAL}^2} + \sigma_{SUNSP} = +10\,mm\ -32\,mm$	Largest bias due to sunspots
EOL no calib	$\sqrt{\sigma_{DIFF}^2 + \sigma_{LDCV}^2 + \dots} + \sigma_{SUNSP} + \dots = +176\,mm\ -198\,mm$	Largest contribution due to lack of calibrations. Exceeds the whole budget

Table 5.6: Lateral and longitudinal errors

Chapter 6

EQM - *Engineering Qualification Model*

In this chapter the process of qualification of the EQM *Engineering Qualification Model* is illustrated. The qualification has the purpose of validate a system, submitting a model (EQM) fully representative of the flight version, to stress levels that it is not opportune to apply to the Flight Model. Other tests aim, instead, to verify the electrical and functional compliance.

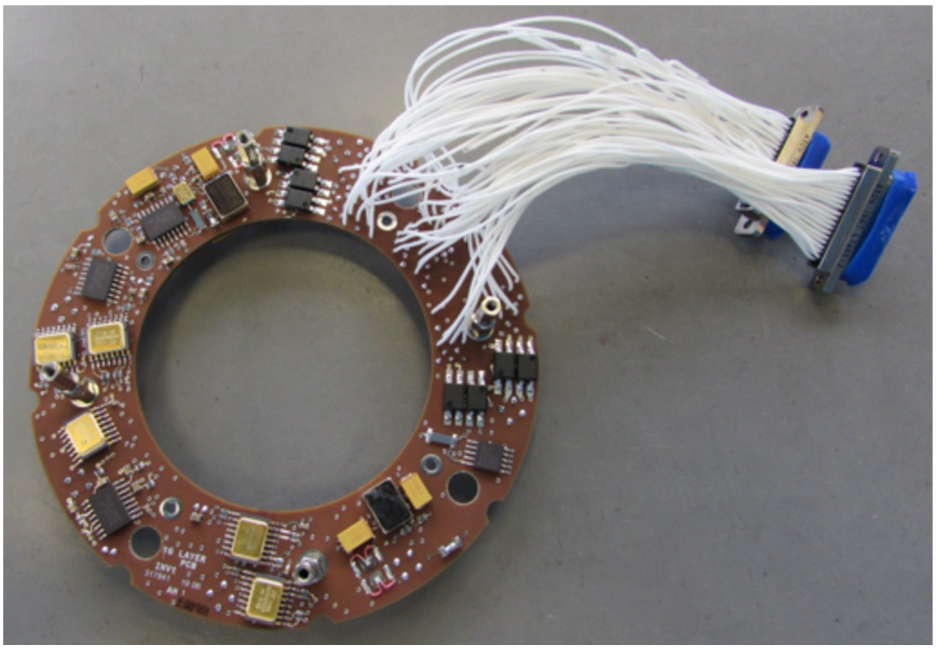

Figure 6.1: The EQM-PCB with the pigtail connectors.

The FPGA-based board used to interface EQM with a PC for functional tests is the same used for the ADM and this was of great advantage to us because it allowed to test simultaneously the two boards and prepare in advance test set-up and procedures for the qualification process. The EQM layout is shown in Appendix A.1.

6.1 EQM qualification tests

The qualification tests are listed in Table 6.1 as part of the activities and tests to which the various SPS models are subject.

Table 6.1: SPS Test Matrix

Test Category	Test Content	STM	EQM	FM	Notes
General	Funct./perf.		T	T	All facilities
Physical	Mass	T	T	T	INAF/OATo
	Dimensions check	T	T	T	INAF/OATo
	COG	A	A	A	By analysis only
	MOI	A	A	A	By analysis only
Mechanical	Random vibration	T	T_{QQ}	T_{AA}	PoliMI (STM)
	Sine vibration	T	T_{QQ}	T_{AA}	SERMS (EQM-FM)
	Shock		T		SERMS
Thermal	Thermal vacuum		T_{QQ}	T_{AA}	IAPS/Rome
	Thermal balance	T	T		
Electrical	Calibration		T	T	ALTEC/OPSYS
	EMC		T	T	at system level (CSL)
	ESD		T		at system level (CSL)

Where T_{QQ} means that test duration and cycles are at qualification level, while T_{AA} means at a lower acceptance level.

The SPS (EQM and FM) shall be subject to a bake-out before delivery to CSL [28]. The bake-out shall be performed under vacuum by heating the SPS at a temperature of 80 °C for a minimum of 72 hours.

Parameter	Nominal	Measured	Notes
PCB mass	76.77 g	123 g	included harness and connectors
PCB internal diameter	70.5 mm	$70.5 \pm 0.1\,mm$	
PCB external diameter	121.5 mm	$121.5 \pm 0.1\,mm$	
PCB thickness	2.0 mm	$2.01 \pm 0.01\,mm$	
M4 holes diameter	7.0 mm	$6.80 \pm 0.05\,mm$	NC, see Section 6.2.1
SPS total mass	560 g	$538 \pm 2\,g$	SPS-5200
Flange internal diameter	50 mm	$50.0 \pm 0.1\,mm$	entrance pupil diam.
Flange external diameter	127 mm	$127.0 \pm 0.1\,mm$	SPS-5101
Flange width	40 mm	$40.0 \pm 0.1\,mm$	
Wall thickness	Front: 4 mm Side: 3 mm Back: 5 mm		

Table 6.2: EQM PCB and flange physical parameters summary table.

6.2 Cleanliness control

The SPS verification activities have taken place in controlled environments in conformance with the mission cleanliness and contamination requirements, that is: "The SPS AIT activities shall be performed in an environment having a class ISO-7, when protected, and ISO-5, when uncovered" (SPS-7110). Actual environmental factors must be monitored following the relevant cleanliness requirements:

SPS-8300	All external surfaces shall be visually free of contamination such as scales, particles, rust, dirt, grease, oil, water or other material.
SPS-8301	The particulate contamination of the SPS (EQM & FM), at the delivery to CSL, shall be ≤ 12 ppm on all surfaces.
SPS-8302	The molecular contamination of the SPS (EQM & FM), at the delivery to CSL, shall be $< 1.0 \times 10^{-7}$ g/cm^2 on all surfaces

During transport the SPS shall withstand the following environmental conditions (SPS-7120):

- Temperature from -40 °C to 60 °C.

Environmental Parameters	Instrument Integration Site (CSL, Belgium)	Spacecraft Integration Site	Under launcher fairing
Pressure	atmospheric	970 hPa to 1050 hPa	atmospheric
Temperature	22 ± 5 °C	20 ± 10 °C	22 °C to 25 °C
Humidity	55% RH ± 10%	45% RH ± 15%	45% to 55% RH
Cleanliness	ISO-7 when protected or closed, ISO-5 when uncovered or open	ISO-8	ISO-7 (lid closed)

Table 6.3: AIT, Storage and Launch Site Environment

- Loads: Vertical $\pm 3\,g$, Horizontal: $\pm 2\,g$.
- Shocks: $\pm 2\,g$ (20 ms, *Saw Tooth*).

6.2.1 Mechanical Non-conformances

Non-conformance control is applied as foreseen in the product assurance and safety requirements document [51] and in ECSS-Q-ST-10C.
Once a non-conformance report (compliant to ECSS-Q-ST-10-09C) has been issued, a non-conformance review board (NCRB) takes place and actions to mitigate the problem are adopted.

Diameter of M4 fixation holes

Description: The fixation holes had a diameter of 6.80 ± 0.05 mm. The expected dimension is 7.0 mm. The fit check within the flange gave a negative result.
Action: Evaluate the possibility to increase the diameter of holes up to 7.1 mm. From a preliminary check on the *gerber* files seems there is enough room around the holes for this operation.

The SiPM protrude from the front surface of the PCB

Description: The SiPM cases protrude for approximately 6.65 mm from the front surface of the PCB. This is not compatible with the flange design. **Action**: For the EQM model, spacers will be installed in order to place the sensor to the right distance from the pinhole.

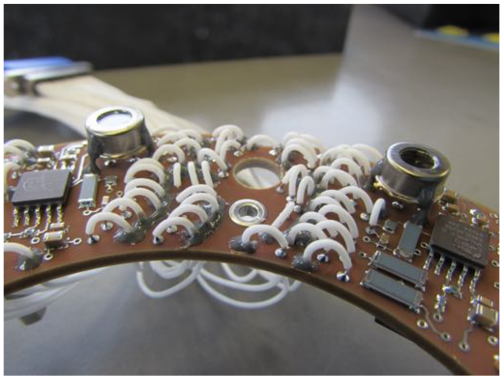

Figure 6.2: The wires staking on the EQM-PCB before reworking.

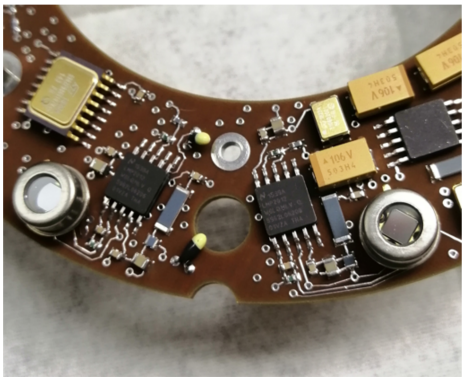

Figure 6.3: One of the thermistors occluding the fixation holes.

Other minor non-conformances are:

- The cable *stakings* are not uniform and too high (see Figure 6.2, refer to Figure 5.8 for the norm), and this required their reworking, reducing and uniforming them.
- One of the temperature sensors was bent (see Figure 6.3), partially occluding one of the fixation holes. Solved straightening the sensor and increasing the rigidity of the sensor pins.

6.3 Vibration and pyroshock

For the random vibration tests, for each axis in [50] are given three tables reporting the loads (g^2/Hz), for frequencies spanning from 20 Hz to 2 kHz. The test duration is 2 minutes for qualification and 2.5 minutes for acceptance. The shock tests will not be performed on Flight Model and the Shock Response Spectrum amplitude is 10 g at 100 Hz and 750 g at 1 and 10 kHz.

Test was successful, in fact the structure did not show any damage evidence and the SPS functionalities have not been affected.

Table 6.4: Sine vibration test loads for all axes [50]

Frequency (Hz)	Acceptance Levels	Qualification Levels
5-100 Hz	24 g	30 g
Sweep Rate	4 Oct/ min (up)	2 Oct/ min (up)

6.4 Electrical and functional tests

Document P3-INF-RP-19036 [34] reports the results obtained during the functional qualification of the SPS-EQM (Engineering Qualification Model) system. The qualification followed the test plan given in [33] and is aimed at verifying the electrical compliance, the functional operation and to validate the absolute performance of the system.

Electrical and functional tests took place in clean-room (ISO-6) laboratory at INAF/OATo (Astrophysical Observatory of Torino). The Turin Observatory facilities are suitable for optical activities of testing, integration and calibration. During electrical and functional tests, the PCB has been exposed for a total of 29 hours to ISO-5 environment. All the OGSE and EGSE (Optical and Electrical Ground Support Equipments) used for the calibration purposes were at the same cleanliness level.

6.4.1 Experimental setup

The Optics laboratory comprises of two environmentally-controlled rooms and a 10 m^2 clean-room equipped with a laminar flux hood and optical benches ($3m \times 1.25m$ for aligning optical instrumentation and an Ultra Performance optical bench, with passive vibration dumping system ($1.6m \times 1.2m$).

SPS-EQM was subject to non-calibrated light sources:

- Flat-field source (Geoptic).
- 200 W Tungsten light source (Newport model QTH 66884). Controller Newport model 69331.

At the PCB center was placed a calibrated photodiode (Opto Diode model AXUV100) whose current was measured by a Keithley 6485 ammeter.

The resistance and conductance measurements were conducted using a a multimeter Keithley model 289. A laboratory bench supply Aim-TTi MX100TP (315W) was used to power the FPGA board and, through it, the PCB.

The dark measurements were performed using vacuum compatible caps machined in Catania Observatory with DELRIN® material.

6.4.2 Power budget

Prior to ADM and EQM tests it was computed the theoretical consumption of SPS. The analitical power budget of one SPS section is detailed in Table 6.5 where is listed the power consumption of each SPS component.

Component	Model	V	mA	#	Tot.(mA)	mW
SiPM	MicroFC-30035-X05	NA	0	4	0	0
OpAmp	LMP2012QML-SP	5reg	1.9	4	7.8	39
ADC (VA)	ADC128S102QML-SP	5reg	0	2	0	0
Vref	LM4050QML	12-5=7		1	7.8	56
Total 5Vreg					7.8	95
ADC (VD)	ADC128S102QML-SP	3.3	0.9	2	1.8	6
Diff. Driver	RHFLVDS31A	3.3	16.5	1	16.5	54.5
Diff. Driver red.	RHFLVDS31A	3.3	2.8	1	2.8	9.2
Diff. Receiver	RHFLVDS32A	3.3	13	1	13	42.9
Diff. Receiver red.	RHFLVDS32A	3.3	3	1	3	9.9
Lin. Regulator 3.3V	VRG8660	12-3.3=8.7		1	37.1	322.8
Total 3.3V					37.1	445.3
Total 12V					44.9	540.3
Enable (5V)					64	322

Table 6.5: Typical consumption for one SPS chain.

The receivers/transmitter in *idle* state draw a non-zero current. Also the 5 V enable signals (routed to the SSR and optocouplers) and the −12 volt OpAmp polarization contribute to dissipate power.

The maximum values of +12 volt current absorbed and power dissipated used in the Worst-Case analysis are, respectively, 56 mA and 0.72 W.
This last result raised some doubt of non-conformance with respect to requirement SPS-5300 from CSL side on the basis that the two channels could be operated at the same time e.g. during calibration procedures. At the end, however, this was not considered an issue both for consumption and for

thermal balance considered that these activities take place occasionally and for a rather short time.

6.4.3 Visual inspection and dimensional measurements

Visual inspection was aimed at verifying the cleanliness and the overall status of the PCB, the right correspondence between components positioning and design layout and the pigtail connectors connections.

Dimensional measurements were all performed in ISO-5 ambient, except for mass measurement that has been deduced from the difference between the packaged PCB and the package alone. The results are given in Table 6.2.

6.4.4 Electrical passive tests

This class of tests was performed with the unpowered PCB, eventually, switching on/off the enable signals. All these tests gave a compliant result.

Ground continuity

This test aimed at checking that the ground wires, when disconnected from the switching board, were all connected between them and to the TP-GND pad on the board. The target resistance was $<1\,\Omega$. Measured resistances were all around 0.2-0.3 Ω.

Enable network input

This test aimed at checking that the optical devices (SSR and optocouplers) were properly connected. We measured the voltage drop V_{drop} on the input LED using the multimeter in diode mode (expected value 0.8 - 1.4 V as reported in datasheet).
The measured voltages were all 1.12 V

Termination resistance for input differential lines

This test aimed at checking that the receivers input differential couples of wires showed a $100\,\Omega(+20\,\Omega\text{-}10\,\Omega)$ resistance ensuring that the termination resistors were mounted correctly.
The measured resistances were all between 101.7 Ω and 103.2 Ω.

High impedance output differential lines

This test aimed at checking that a high impedance (>100 kΩ) was present between the following differential couples of wires, when the drivers were not powered.
The measured resistances were all between 85 and 95 MΩ with the exception of the value of HI-ODL-R#2 (26 MΩ). Although this value is in the desired range >100 kΩ, it is very different from the other ones and it should be further investigated.

6.4.5 DC Electrical tests

This class of tests is performed supplying the PCB by means of the FPGA interface board and by the usage of the laboratory bench supply voltage.

Isolation of primary voltages

This test aimed at checking that the $\pm 12\,V$ redundant power lines are galvanic isolated from main ones by means of SSR, thus maintaining an isolation of at least 1 MΩ (<1 µS) and so ensuring that any failure in one CCB shall not affect the function of the other CCB. The test was done using flying wires inserted in the Nominal and Redundant PCB connectors and measuring the isolation resistance or, equivalently, the conductance. The measured resistances were out of instrument scale showing a conductance <0.01 nS

Power Supply switching

This test aimed at checking that, when SSR and optocouplers are switched on/off, and $\pm 12\,V$ is supplied, the primary voltages at the linear regulator input (+12 V) and before the voltage divider (−12 V) are present (or not). The secondary voltages are checked, too. It was done by:

1. Connecting the EQM-PCB to the FPGA board and enabling/disabling signals as in previous tests.
2. Checking the voltages into the test points.

Using a multimeter set to DC voltage, we verified that all (+12, -12, 3.3, 5, -0.12) voltages were in the desired range (see Table 5.1).

Supply currents measurements

This test aimed at verifying that min, max and average currents sourced from $\pm 12\,V$ were within the limits. It could be done measuring the $+12\,\mathrm{V}$, $-12\,\mathrm{V}$ and enable $5\,\mathrm{V}$ currents using the pigtail connector as a breakout. The expected currents depend from the usage and are detailed in [34]. In Table 6.6, a summary of the measured currents.

Voltage	set A (mA)	set B (mA)	both (mA)
$+12\,\mathrm{V}$	59	59	118
$-12\,\mathrm{V}$	29	30	59
enable $5\,\mathrm{V}$	18	18	36
Total power mW	1146	1158	

Table 6.6: Measured SPS-EQM input currents.

In both cases with a single channel on or both channels ON, the total power consumption is well above the requirement specification of $0.9\,\mathrm{W}$. This non-conformance is not considered an issue for the reasons explained in Section 5.1.1.

6.4.6 Functional tests

These tests aimed at checking SPS full functionally at nominal supply voltage ($\pm 12.0\,V$) and FPGA interface board clock frequency ($7\,\mathrm{MHz}$ instead of $4.16\,\mathrm{MHz}$). It was done by:

1. Connecting the EQM-PCB to the FPGA board and enabling/disabling signals as in previous tests.
2. Checking the outputs.

Linearity

The linearity of the 8 channels is confirmed and the ratio 1:5 between low gain and high gain is also confirmed for signals higher than $100\,\mathrm{DN}$ (Low Gain) as shown in Figure 6.4.

Even if the ratio 1:5 between the low gain and high gain channels is not respected on the full radiometric range, we believe that this is not critical for the system performance and in case could be calibrated.

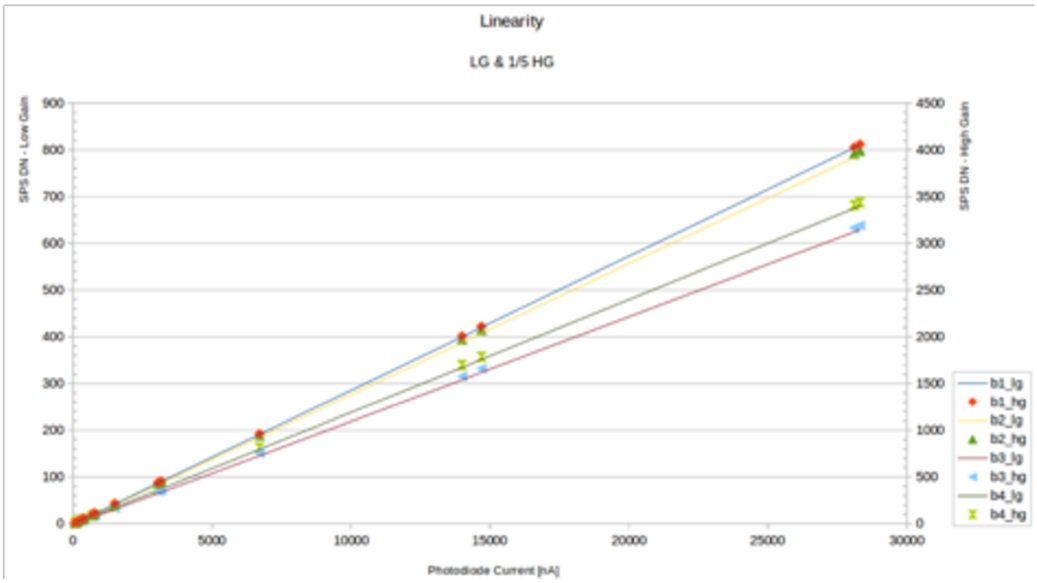

Figure 6.4: Superposition of low and high values in function of the calibrated photodiode current, showing linearity in SPS response and proportionality between high and low gain outputs.

Sensitivity

The variations of currents associated to the variations of 1 DN on the high gain give an average of 2.4 nA/DN. These measurements will be replicated when the radiometric tests will be performed using a more accurate set-up.

6.5 Thermovacuum

The thermo-vacuum qualification and functional/performance tests have been performed at IAPS (Institute for Space Astrophysics and Planetology) facility in Rome where the thermal vacuum chamber is located inside a clean-room. The thermal qualification test campaign of the SPS EQM consisted of:

1. Thermal Vacuum Test: eight cycles in the qualification temperature range (−30 °C, 89 °C), with a ON/OFF sequence of the instrument during the first cycle at the operative temperature limits (−19.6 °C, 78.7 °C);

2. Thermal Balance Test: consisting in switching on the SPS in two cases, hot and cold (FDA structure interface set to 70 and -37 C, respectively)

The thermal cycles have been performed as expected and the functional verification during and after them has shown that no impact has been suffered by the unit. The hot and cold case of the thermal balance test were defined by the temperature range of the relevant interfaces to the SPS (see Table 3.1:

1. FDA structure (radiative): (−36.8 °C, 70.3 °C)
2. FDA lid (radiative): (−80 °C, 68.5 °C)
3. COB tube (conductive and radiative): (34 °C, 36 °C)

A set of shields and supports were designed and manufactured purposely for this test and couples of thermometer/heater were integrated in order to provide the active control needed to reach the desired temperature at the interfaces

The T-VAC functional/performance test consisted in two sequences having a duration of about 30 minutes each, in which four types of tests were performed:

1. Power ON/OFF cycle, checking the power absorption of the 3 channels (±12 V and 5 V) of the SPS board.
2. SPS Dark Signal Acquisition, registering the DN returned by the SPS board while acquiring a dark signal.
3. SPS Board Temperature Acquisition, registering the temperatures returned by the SPS board.
4. SPS Radiometric measurements, registering the DN returned by the SPS board while acquiring a flat field signal.

After a short functional test (SFT), running tests # 1, 2 and 3, it was performed the radiometric functional test (RFT) running tests 1 and 4.

Chapter 7

Future work, on-ground and in-flight calibrations

7.1 Introduction

This chapter describes the current status of the SPS subsystem development, further activities and discusses the perspective for future research.

An hybrid (hardware and software) data-chain will simulate all SPS functions and will be useful before and after the launch to verify the electronics and the algorithm performance. This SPS metrology simulator is treated in Section 7.2. SPS electronics needs to be accurately calibrated on-ground to minimize its contribution to the error and this activity is outlined in Section 7.3.

The main outcome of the error budget analysis is that the lack of knowledge of the real penumbra profile present in space can introduce a huge error in SPS measurements. This leads to the need of performing the in-flight characterization of the shape of irradiance levels around the nominal position scanning the penumbra with lateral (retargeting) and longitudinal (resizing) maneuvers. Details on the in-flight activities are given in Section 7.4.

7.2 SPS metrology performance simulator

The SPS system behaviour is simulated by a data-chain whose purpose is to describe the various steps taking place in SPS system: from spacecrafts rel-

ative displacements (X,Y,Z) to illumination level variations, electric signals, digital data, up to the reconstruction of the position by the algorithm.

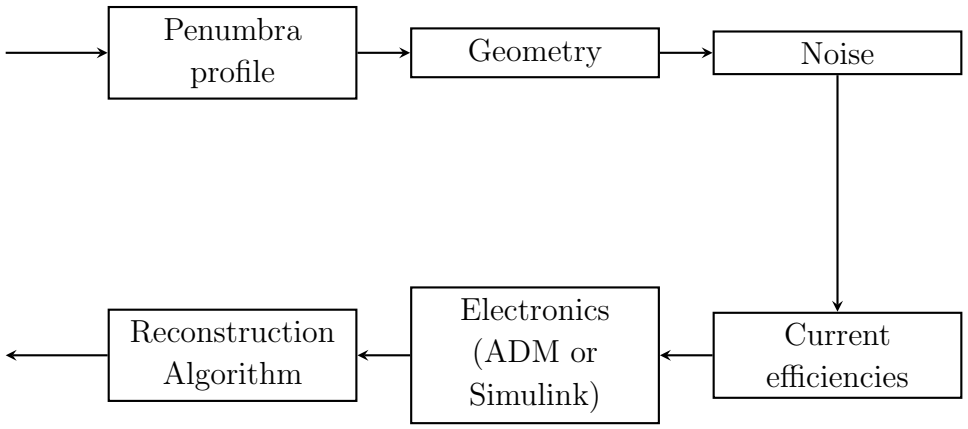

Figure 7.1: SPS metrology performance simulator overview.

Block #	Name	Input	Parameters	Output
1	Penumbra profile	(X,Y,Z)	limb dark coeff. λ, T_F, T_W	Radial profile
2	Geometry	Radial profile	SiPM respons.	SiPM 8× currents
3	Noise	8×C	n_i.	8×C
4	Current correction	8×C	k_i	8×C
5	Electronics	8×C	El. parameters Temperature	16×DN
6	Reconstruction Algo	16×DN	a, b, c H, K, L	(X,Y,Z)

Table 7.1: The blocks composing the SPS simulator

All these parts can be simulated by software, described by models (e.g. MatLab/Simulink modules, see Figures A.5 and A.6 in Appendix) or hardware (the ADM covers many blocks), in order to give a realistic response.

7.3 Radiometric on-ground calibrations

Calibration on-ground [8] will consist in the SPS radiometric and stability calibration and in the validation of the algorithms. This calibration will be

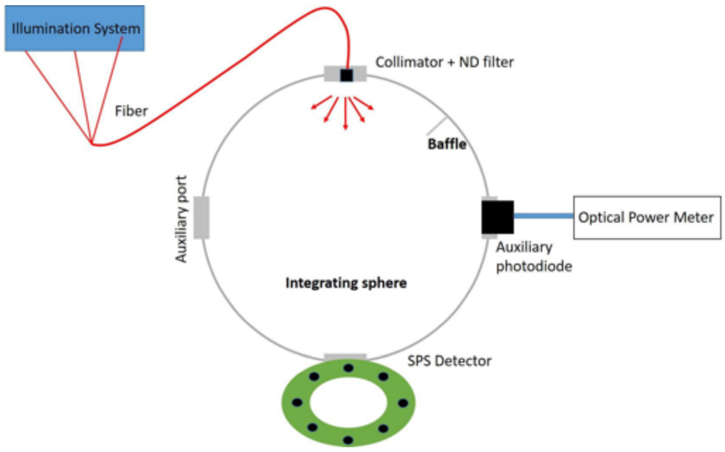

Figure 7.2: Schematic view of the set-up for the stability tests on the ADM

performed at SPS system level by INAF with full functional and performance tests on the EQM and short functional tests on the FM. Short functional tests will also be performed at instrument level after the FM environmental test campaign and before the delivery of the ASPIICS instrument to ESA.

The document [23] describes the on-ground calibration procedure for the instrument verification and calibration of the whole ASPIICS system. Calibration will be performed at the INAF/OPSYS facility (in ALTEC, Turin) at instrument level, following the calibration plan given in [8], with the objective to verify the instrument conformance with the science and performance requirements.

The light source is characterized by a high dynamical range and accuracy. The illumination system is composed by three Prizmatix UHP-F LED coupled to a fiber bundle connecting to a collimator covered by a Neutral Density (ND3) filter. A 3-channels, 12-bit controller, using I2C (Inter Integrated Circuit) protocol is used for remote power control. The LED emission is centered at 625 nm with a FWHM (Full Width at Half the Maximum) of 25 nm. The fiber optics diameter is of 3 mm.

The tests described in the following Table 7.2 will be done on the ADM using the integrating sphere as illustrated in Figure 7.2. EQM and FM, instead, will be subject to direct illumination.

Test Type	Description	ADM	EQM	FM
Stability	3 levels of irradiance	X	X	X
Radiometric	Estimation of responsivity in the full operative range	X		
Radiometric (temperature dependence)	Repeated at different temperatures.	X	X	X
Error budget verification	Estimation of responsivity in the full operative range	X		
Algorithms validation	Simulation of different FF configurations	X	X	

Table 7.2: Summary of the SPS on-ground tests

7.4 In-flight calibrations

SPS in-flight calibration [7] will take place during commissioning and during formation-flying demonstration activities and will consist in:

1. Calibration of the penumbra profile parameters using: formation roll, retargeting and resizing maneuvers.

2. Radiometric calibration using retargeting maneuvers.

All these maneuvers were described in Section 2.2.3.

7.4.1 Penumbra profile calibration/validation

We have seen in Section 5.4.4 how the residual main uncertainty that can affect the SPS algorithm is the model describing the Sun irradiance profile present in the penumbra.

The penumbra profile parameters used by the algorithms are 6: a, b, c, H, L and K (see Section 3.4); the in-flight calibration will recalibrate these parameters periodically and will consist in two operations:

1. Longitudinal scan

2. Lateral scan

The *longitudinal scan* will detect the center of the penumbra for eleven ISD around the nominal one, from $-500\,\mathrm{mm}$ to $+500\,\mathrm{mm}$ in steps of $100\,\mathrm{mm}$.

The calibration proceeds evaluating the parameters H, L and K first: Once fixed the ISD, using the retargeting maneuver between -1° and $+1^\circ$, the center of the penumbra can be detected. The roll maneuver (0-360° in 10 steps) is used to increase the accuracy of the measurements. Applying these two maneuvers at different ISD (obtained by the formation resizing maneuver and controlled by the FLLS subsystem) we expect to evaluate the longitudinal parameters.

The parameters a, b and c of the pseudo-paraboloid are, instead, retrieved using the retargeting maneuver, between -1° and $+1^\circ$, at the nominal ISD (lateral scan operation). The calibration of penumbra profile will exploit also information coming from other metrology subsystems (FLLS, Star Trackers, OPSE etc.), and, in order to obtain the parameters with a good accuracy, it is required to know the retargeting velocity with an accuracy of $0.5\,\mathrm{mm\,s^{-1}}$.

7.4.2 SPS radiometric calibration

The in-flight calibrations of the SPS SiPM individual responses (k_i) are performed with the CSC in full Sun and the front door closed, and can be done just at the beginning of the mission when S/C are in stacked configuration. After this pre-calibration, the SPS radiometric response will be recalibrated again during safe orbit commissioning. In the rest of the mission, radiometric calibration of the SPS will take place when the FF is broken and the CSC is pointing the Sun. From this absolute calibration, we expect to monitor the ageing of the SPS. Both the information of current and temperature must be available in order to take into account the temperature effects on the SPS responsivity. The ratio between the measured current and the theoretical one will give the normalization factors k_i.

Appendix A

Appendix

A.1 SPS layout and schematics

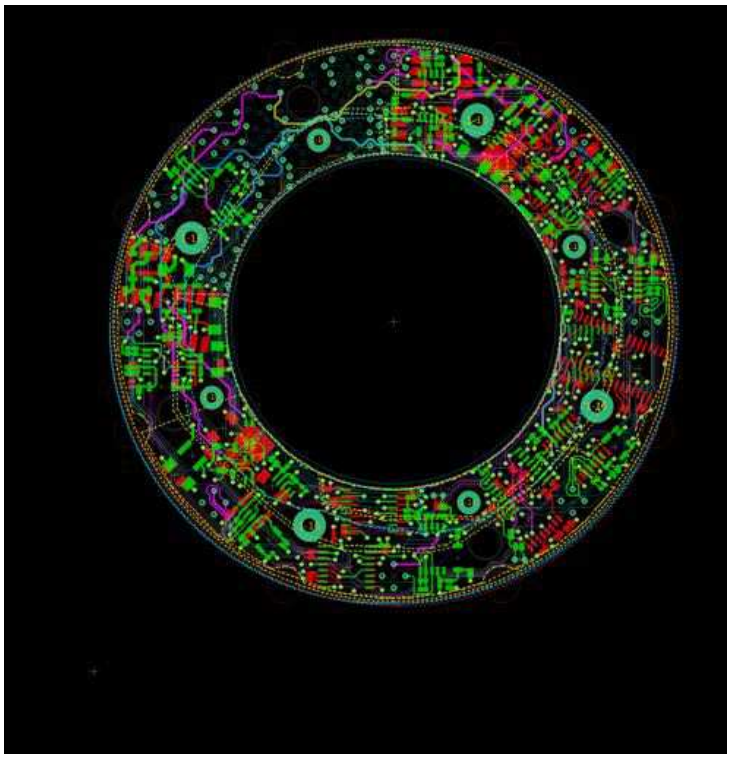

Figure A.1: SPS layout.

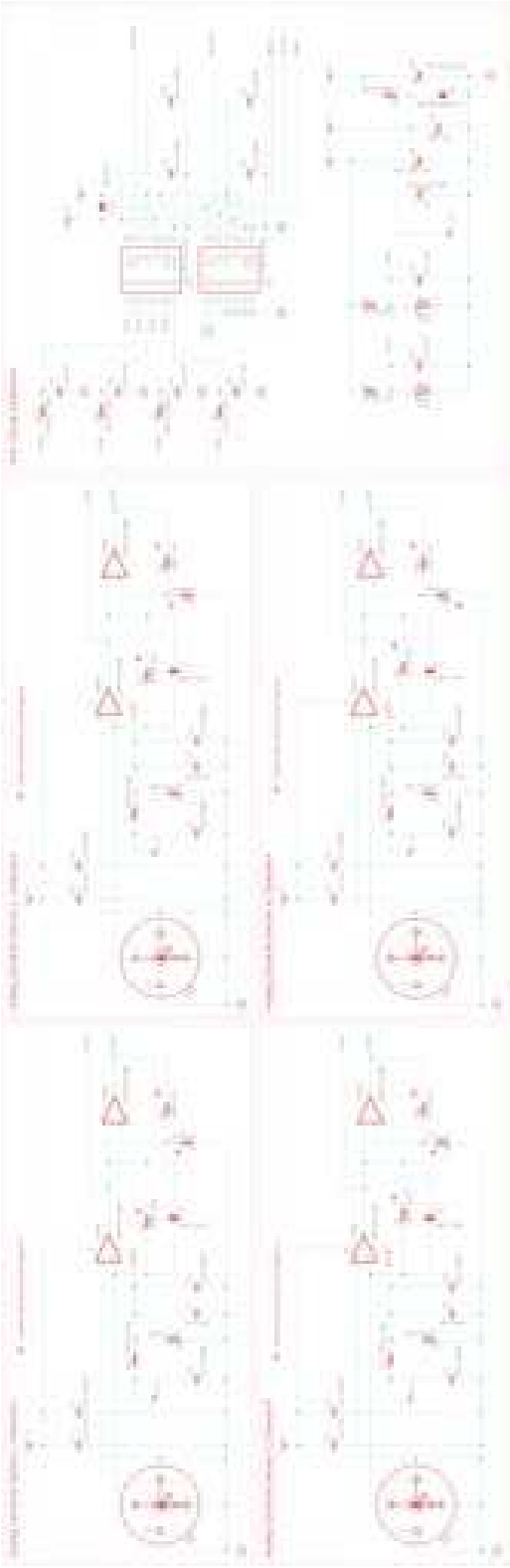

Figure A.2: Schematic page 1.

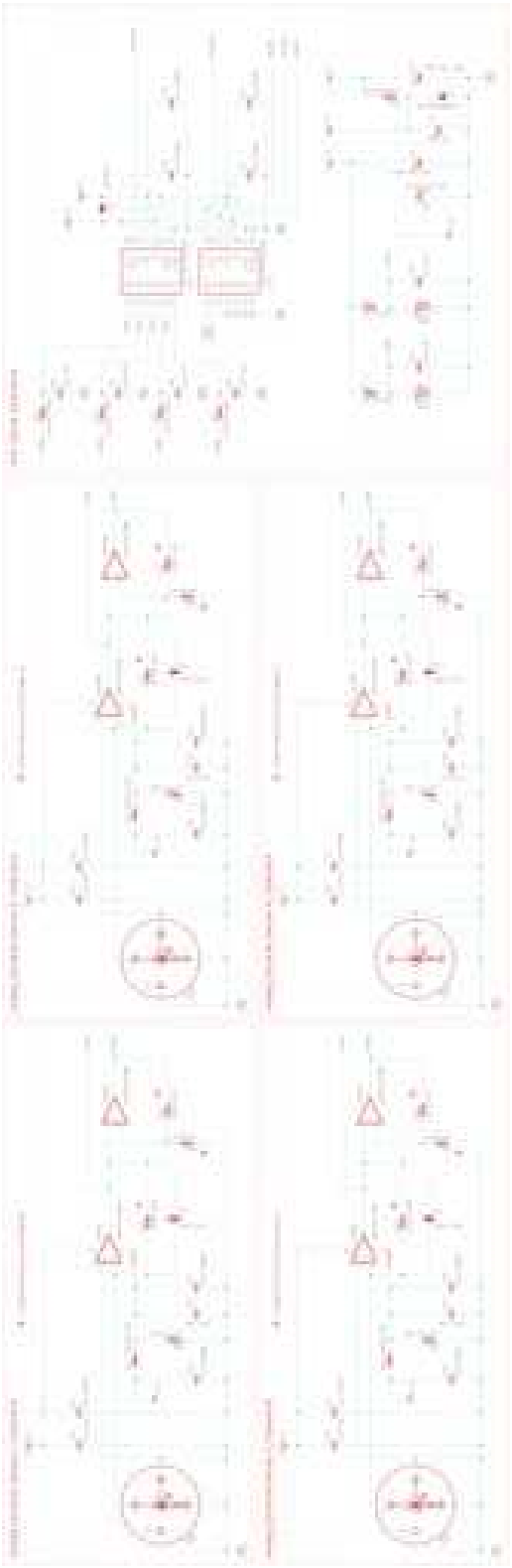

Figure A.3: Schematic page 2.

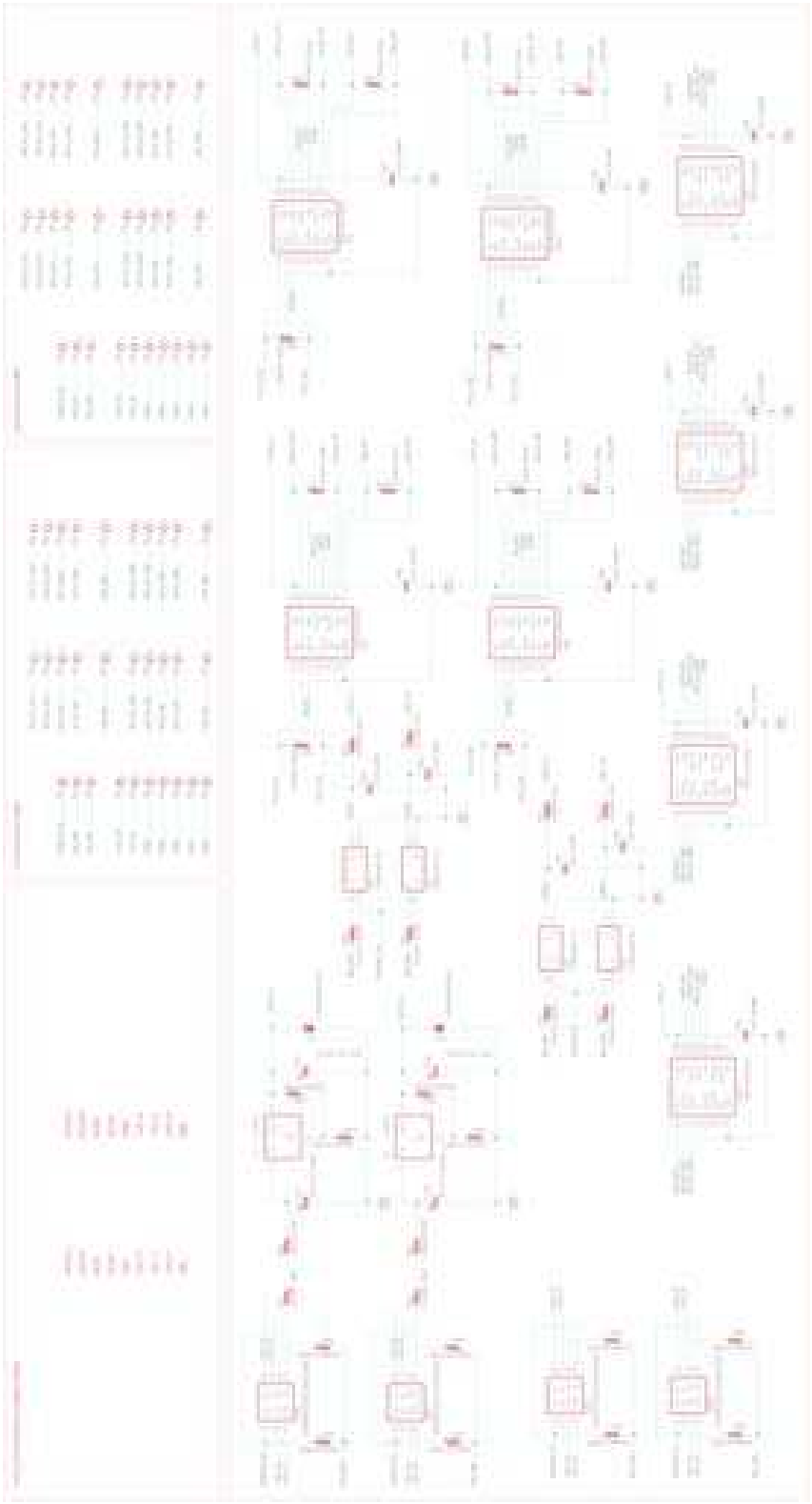

Figure A.4: Schematic page 3.

A.2 MatLab/Simulink models

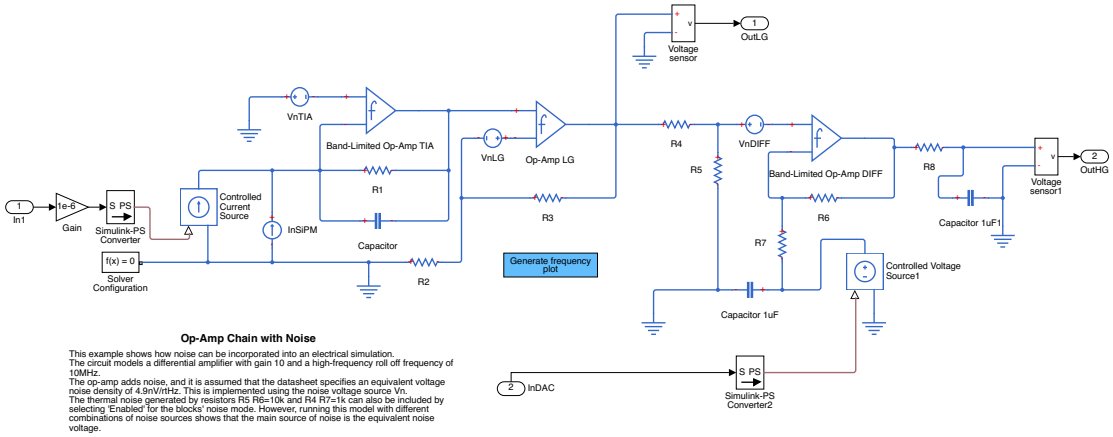

Figure A.5: The Simscape/Simulink model of one complete amplification chain used to evaluate the noise produced by a SPS sensor and by its electronics.

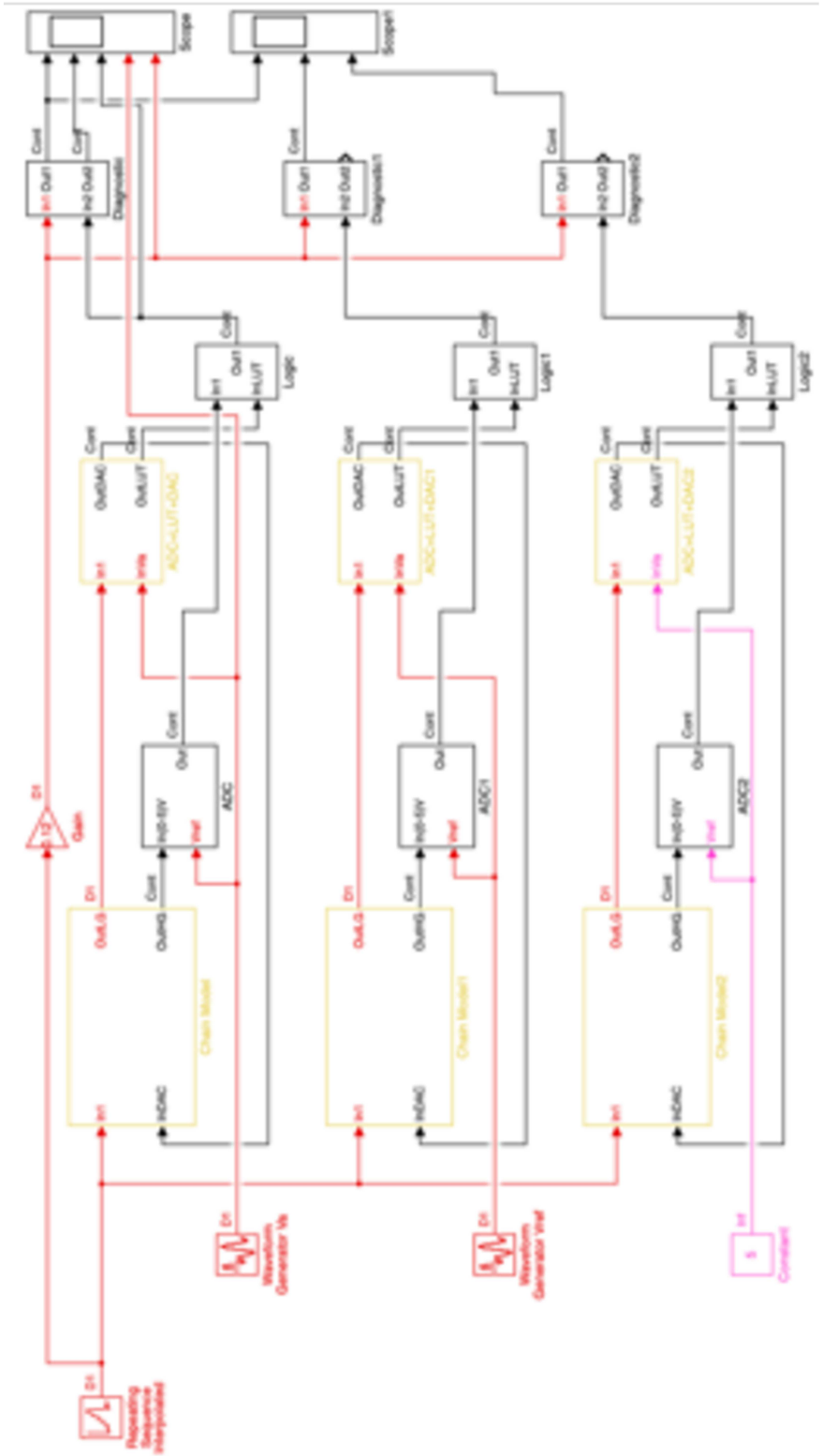

Figure A.6: The Simulink model used to analyse the influence of the voltage supply uncertainties on the amplification chain of one SPS sensor.

A.3 PSA tables

Item	Qty	EPFL Family Code	Part ID	Value	bom	θjc θja °C/W	Brand	Part Number	SMD/Qualification	TID krad	ELDRS	Comment
1	40	01-02	Multilayer Cap. SMD	various µF	0805	250	AVX	3009041 03... KA	ESCC QPL 30009/041			X=16V A=25V MAX 0805 1 µF
2	48	01-02	Multilayer Cap. SMD	various nF	0603	400	AVX	3009041 02... KA	ESCC QPL 30009/041			MAX 0603 180 nF
3	10	01-03	Tantalum Cap. SMD	10-68 µF	2917	<100	AVX	TAJD ... 35ESA				
4	24	10-08	0.01% resistor	various kΩ	0402	<800		4001/023				
5	40	10-08	Thin Film Resistor SMD	various Ω	0505	<500	Vishay	M55342 E 02 B ... TTSV	MIL-PRF-55342			
6	40	10-08	Thin Film Resistor SMD	various kΩ	0505	<500	Vishay	M55342 E 02 B ... TTSV	MIL-PRF-55342			
7	14	10-08	Thin Film Resistor SMD	various Ω	2208	<200	Vishay	M55342 E 05 B ... TTSV	MIL-PRF-55342			
8	14	10-08	Thin Film Resistor SMD	50 Ω	2512	110	Vishay	M55342 E 09 B ... TTSV	MIL-PRF-55342			
9	2	10-08	Thin Film Resistor SMD	453 Ω	2512	110	Vishay	M55342 E 09 B ... TTSV	MIL-PRF-55342			
10	8	10-08	Thermistor	NTC 2252 Ω	BEAD 5-lead	125 1000	TE Connectivity	44901	GSFC S-311B-P-18-0157R6 MIL-PRF-23648			
11	24	08-50	LMP2012QML-SP	OpAmp	10-lead CLGA NAC	12.3	Texas Instruments	LMP2012QML-SP	5962-06206 5962-0620601VDA			ELDRS free 50 krad
12	2	04-04	LM4050QML-SP	5V reference	10-Lead Cer. CFP	214	Texas Instruments	LM4050QML-SP	5962R9233611VZA	100		SEFI immune
13	4	18-01	CSM100	Optocoupler	4-pin LCC		ISOLINK			150		
14	8	08-61	ADC12B5102QML-SP	ADC	16-pin CFP NAC	11.2 127	Texas Instruments	ADC12B5102WGQV	5962R0722701VZA			SEL immune up to 120 MeV..
15	6	18-01	RDHA701CD10A2NX	SSR	8 pin ceramic	30	IR	RDHA701CD10A2NX				8 Pin Ceramic SMD
16	4	08-55	RHFLVDS31A	Diff Driver	16-Lead FLATPACK	22 —	ST	RHFLVDS31A	5962F98651	300		SEL immune up to 135 MeV
17	4	08-56	RHFLVDS32A	Diff Receiver	16-Lead FLATPACK	22 —	ST	RHFLVDS32A	5962F98652	300		SEL immune up to 135 MeV
18	2	08-52	VRG8660	Regulator	SMD	3 —	Cobham	VRG8660-901	5962-0920601	100		SMD-0.5 Power Pkg

Figure A.7: The list of SPS components deduced from the Bill Of Material.

Part ref.	Part type	Nom. Value	Mfg Toler.	Parameter	Rated value	Derating*	Max. Derated	Actual max	Stress Ratio	Compliant	Remarks
R5, 6, 15, 16, 32, 33, 42, 43	Thin Film Chip Resistor	100 kΩ	0.01%	Junction T (°C)	155	NA	125	62	0.5	yes	Rth_{j-a} = 800 °C/W
	SMD 0402			Voltage (V)	50	0.8	40	<5	<0.2	yes	
	4001023-131003L9 (PHR)			Power (mW)	50	0.5	25	<300µ	negig.	yes	
R7, 8, 17, 18, 34, 35, 44, 45	Thin Film Chip Resistor	3 kΩ	0.01%	Junction T (°C)	155	NA	125	62	0.5	yes	Rth_{j-a} = 800 °C/W
	SMD 0402			Voltage (V)	50	0.8	40	1	negig.	yes	
	4001023-133001L9 (PHR)			Power (mW)	50	0.5	25	0.3	negig.	yes	
R9, 10, 19, 20, 36, 37, 46, 47	Thin Film Chip Resistor	12 kΩ	0.01%	Junction T (°C)	155	NA	125	62	0.5	yes	Rth_{j-a} = 800 °C/W
	SMD 0402			Voltage (V)	50	0.8	40	4	negig.	yes	
	4001023-133202L9 (PHR)			Power (mW)	50	0.5	25	1.3	negig.	yes	
R3, 4, 13, 14, 30, 31, 40, 41	Thin Film Resistor	20 Ω	1%	Junction T (°C)	155	NA	125	62	0.5	yes	Rth_{j-a} = 500 °C/W
	Surface Mount Chip 0505			Voltage (V)	40	0.8	32	0.12	negig.	yes	
	M55342E02B20D0TTSV			Power (mW)	125	0.5	62	1.1	negig.	yes	
R1, 2, 11, 12, 28, 29, 38, 39	Thin Film Resistor	1.6 kΩ	1%	Junction T (°C)	155	NA	125	79	0.64	yes	Rth_{j-a} = 200 °C/W
	Surface Mount Chip 2208			Voltage (V)	175	0.8	140	12.5	0.08	yes	
	M55342E05B1E60TTSV			Power (mW)	225	0.5	112	90	0.8	yes	
R65, 66	Thin Film Resistor	100 Ω	1%	Junction T (°C)	155	NA	125	69	0.56	yes	Rth_{j-a} = 500 °C/W
	Surface Mount Chip 0505			Voltage (V)	40	0.8	32	<3.3	negig.	yes	
	M55342-E02B100DTTSV			Power (mW)	125	0.5	62	16	0.26	yes	
R63, 64	Thin Film Resistor	165 Ω	1%	Junction T (°C)	155	NA	125	74	0.6	yes	Rth_{j-a} = 500 °C/W
	Surface Mount Chip 0505			Voltage (V)	40	0.8	32	<3.3	negig.	yes	
	M55342-E02B165DTTSV			Power (mW)	125	0.5	62	26	0.42	yes	

*the power derating is 50% up to 85°C, decreasing to 0% at 125°C

Figure A.8: The PSA page 1: part of resistors.

Part ref.	Part type	Nom. Value	Mfg Toler.	Parameter	Rated value	Derating	Max. Derated	Actual max	Stress Ratio	Compliant	Remarks
C11, 12, 23, 24, 49, 50, 61, 62	Multilayer capacitor SMD 0603	10 nF	10%	Case temp (°C)	125	*	85	61	0.72	yes	
	3009041 02 103 KA			Voltage (V)	25	0.6	15	5.05	0.34	yes	
C89 C90 C91 C92	Multilayer capacitor SMD 0603	10 nF	10%	Case temp (°C)	125	*	85	61	0.72	yes	EN
	3009041 02 103 KA			Voltage (V)	25	0.6	15	3.5	0.23	yes	
C32 C33 C70 C71	Multilayer capacitor SMD 0603	100 nF	10%	Case temp (°C)	125	*	85	61	0.72	yes	
	3009041 02 104 KA			Voltage (V)	25	0.6	15	5.05	0.34	yes	
C36 C37 C74 C75	Multilayer capacitor SMD 0603	100 nF	10%	Case temp (°C)	125	*	85	61	0.72	yes	
	3009041 02 104 KA			Voltage (V)	25	0.6	15	3.5	0.34	yes	
C3 C4 C15 C16 C41 C42 C53 C54	Multilayer capacitor SMD 0603	100 nF	10%	Case temp (°C)	125	*	85	61	0.72	yes	Vdd OpAmp
	3009041 02 104 KA			Voltage (V)	25	0.6	15	5.05	0.34	yes	
C9 C10 C21 C22 C47 C48 C59 C60	Multilayer capacitor SMD 0603	100 nF	10%	Case temp (°C)	125	*	85	61	0.72	yes	Vee OpAmp
	3009041 02 104 KA			Voltage (V)	25	0.6	15	0.15	0.23	yes	
C81, 82, 83, 84, 85, 86, 87, 88	Multilayer capacitor SMD 0603	100 nF	10%	Case temp (°C)	125	*	85	61	0.72	yes	TX/RX
	3009041 02 104 KA			Voltage (V)	25	0.6	15	3.5	0.34	yes	
C5 C6 C17 C18 C43 C44 C55 C56	Multilayer capacitor SMD 0603	100 nF	10%	Case temp (°C)	125	*	85	61	0.72	yes	-12V
	3009041 02 104 KA			Voltage (V)	25	0.6	15	13	0.87	yes	
C25 C26 C27 C28 C63 C64 C65 C66	Multilayer capacitor SMD 0805	1µF	10%	Case temp (°C)	125	*	85	61	0.72	yes	C LP filter
	3009041 02 105 KA			Voltage (V)	25	0.6	15	5.05	0.34	yes	
C7 C8 C19 C20 C45 C46 C57 C58	Multilayer capacitor SMD 0805	1µF	10%	Case temp (°C)	125	*	85	61	0.72	yes	Vee OpAmp
	3009041 02 105 KA			Voltage (V)	25	0.6	15	0.15	0.01	yes	
C29 C30 C67 C68	Multilayer capacitor SMD 0805	1µF	10%	Case temp (°C)	125	*	85	61	0.72	yes	Thermistors
	3009041 02 105 KA			Voltage (V)	25	0.6	15	3.5	0.23	yes	
C1, 2, 13, 14, 39, 40, 51, 52	Multilayer capacitor SMD 0805	1µF	10%	Case temp (°C)	125	*	85	61	0.72	yes	Vdd OpAmp
	3009041 02 105 KA			Voltage (V)	25	0.6	15	5.05	0.34	Yes	

*the voltage derating is 60% up to 85°C, decreasing to 40% at 110°C and 0% beyond.

Figure A.9: The PSA page 3: part of capacitors.

Part ref.	Part type	Package	Parameter	Rated value	Derating	Max. Derated	Actual value	Stress Ratio	Compliant	Remarks
D1 D2 D3 D4 D5 D6 D7 D8	SiPM MicroFB-30035-X05	X05	Junction Temperature (°C)	85*	NA	85	81**	0.96	yes	*Max recommended operating temperature range **See P3-INF-TN-17020
			Power (mW)	90	0.5	45	<0.01	neglig.	yes	
			Output Current (mA)	3	0.8	2.4	0.05	<0.03	yes	
			Vce	30	0.75	22	0.7	<0.04	yes	
D9 D10	Schottky diode 1N5822U	LCC2B	Junction Temperature (°C)	150	NA	110	61	0.56	yes	
			Power (mW)	1200	0.5	600	<<1	neglig.	yes	
			Reverse voltage (V)	40	0.75	30	<3.5	<0.2	yes	
			Peak forward current (A)	80	NA	NA	<0.05	neglig.	yes	
			Forward current (mA)	3000	0.75	2200	<0.05	neglig.	yes	
D11 D12	Zener diode 1N6315US		Junction Temperature (°C)	175	NA	110	72	0.66	Yes	*When protection is active, otherwise <<1
			Power (mW)	500	0.65	325	294*	0.91	yes	
TH1 TH2 TH3 TH4	Thermistor 44901	BEAD	Junction Temperature (°C)	90	NA	90	61	0.68	yes	
			Power (mW)	NA	0.5	NA	<1	neglig.	yes	
U1 U2 U3 U4 U8 U9 U10 U11	LMP2012QML Dual Operational Amplifier TI	10-lead CFP NAC0010A	Junction Temperature (°C)	150	NA	110	61	0.56	yes	*used Input current instead of input voltage as per doc ECSS-Q-ST-30-11C Rev 1 table 6-21
			Power (mW)	714	NA	714	<12	neglig.	yes	
			Supply voltage (V)	5.8	0.9	5.22	5.15	0.99	yes	
			Input current (mA)*	30	0.5	15	0.5	neglig.	yes	
			Output current (mA)	30	0.8	24	2	neglig.	yes	
U7 U14	LM4050QML Voltage Reference	10-lead CFP NAC0010A	Junction Temperature (°C)	150	NA	110	68	0.62	yes	
			Power (mW)	467	0.65	303	<35	0.12	yes	
			Reverse current (mA)	20	0.65	13	<7	0.5	yes	
U5 U6 U12 U13	ADC 128S102	CDFP4-FP16	Junction Temperature (°C)	175	NA	110	63	0.58	yes	*Min between max operating conditions and 90% of 6.5V **up to VA
			Power (mW)	1181	NA	1181	8	neglig.	Yes	
			Analog supply voltage (V)	6.5	0.9	5.25*	5.05	0.96	yes	
			Digital supply voltage (V)	6.5	0.9	5.25**	3.5	0.67	yes	
			Input voltage (V)	NA	0.8	5.25**	5.05	0.96	yes	

Figure A.10: The PSA page 5: active components

Part ref.	Part type	Package	Parameter	Rated value	Derating	Max. Derated	Actual value	Stress Ratio	Compliant	Remarks
U15 U16 U17 U18	RDHA701CD10A2NX	8-pin ceramic	Junction Temperature (°C)	150	NA	110	61	0.56	yes	Pdmax=1W <40 mW
	LED Side		Diode Forward Current (mA)	40	NA 0.5	20	10	0.5	yes	
			Diode Reverse Voltage (V)	1.85	0.75	1.3	0	0	yes	
	Photo-transistor Side		Output Current (mA)	1000	0.8	800	50	0.06	yes	
			Vce	100	0.75	75	12.5	<0.2	yes	
U22 U23 U24 U25	Optoisolator CSM300	4-pin LCC	Junction Temperature (°C)	150	NA	110	61	0.56	yes	<20 mW
	LED Side		Diode Forward Current (mA)	40	linear	40	10	0.25	yes	65°C - 0.67mA/°C
			Diode Reverse Voltage (V)	2	0.75	1.5	0	0	yes	
	Photo-transistor Side		Output Current (mA)	50	0.8	40	<1	neglig.	yes	
			Vce (V)	40	0.75	30	3..5	neglig.	yes	
U19 U20	VRG8660	SMD-0.5	Junction Temperature (°C)	150	NA	110	63	0.6	yes	* @63°C
			Power (W)	14*	linear	7**	0.253	neglig.	yes	** 50%
			Supply voltage (V)	43	0.9	38	8.8	0.25	yes	θjc =3°C/W
			Input voltage (V)	43	0.9	38	8.8	0.25	yes	
			Output Current (mA)	1500	0.8	1200	46	neglig.	yes	
U21 U26 U29 U32	RHFLVDS31A	16-Lead FLATPACK	Junction Temperature (°C)	150	NA	110	63	0.58	yes	θjc =22°C/W
			Power (mW)	1250	NA	1250	55	neglig.	yes	
			Supply voltage (V)	4.8	0.9	4.3	3..5	0.76	yes	
			Input voltage (V)	4.8	0.9	4.3	3..5	0.76	yes	
			Output Current (mA)	650	0.8	522	14	neglig.	yes	
U27 U28 U30 U31	RHFLVDS32A	16-Lead FLATPACK	Junction Temperature (°C)	150	NA	110	63	0.58	yes	
			Power (mW)	1250	NA	1250	43	neglig.	Yes	
			Supply voltage (V)	4.8	0.9	4.3	3..5	0.76	Yes	
			Input voltage (V)	4.8	0.9	4.3	3..5	0.76	Yes	
			Output Current (mA)	650	0.8	522	neglig.	neglig.	Yes	

Figure A.11: The PSA page 6: active components.

A.4 FMEA worksheet

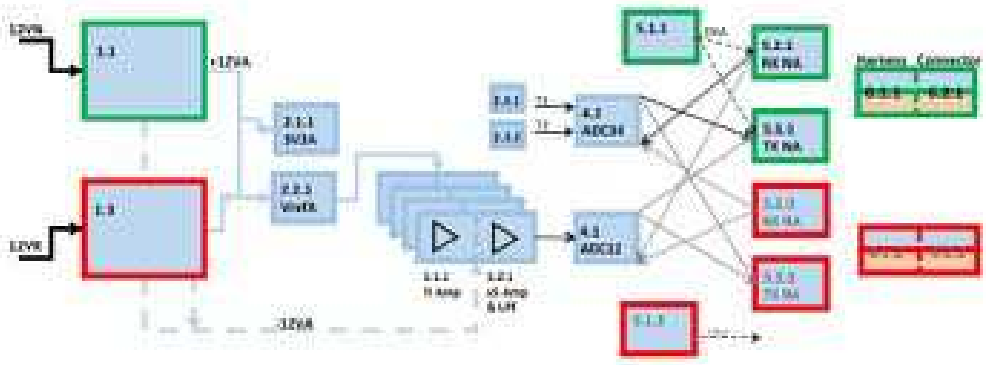

Figure A.12: A detailed functional splitting of the SPS set A only.

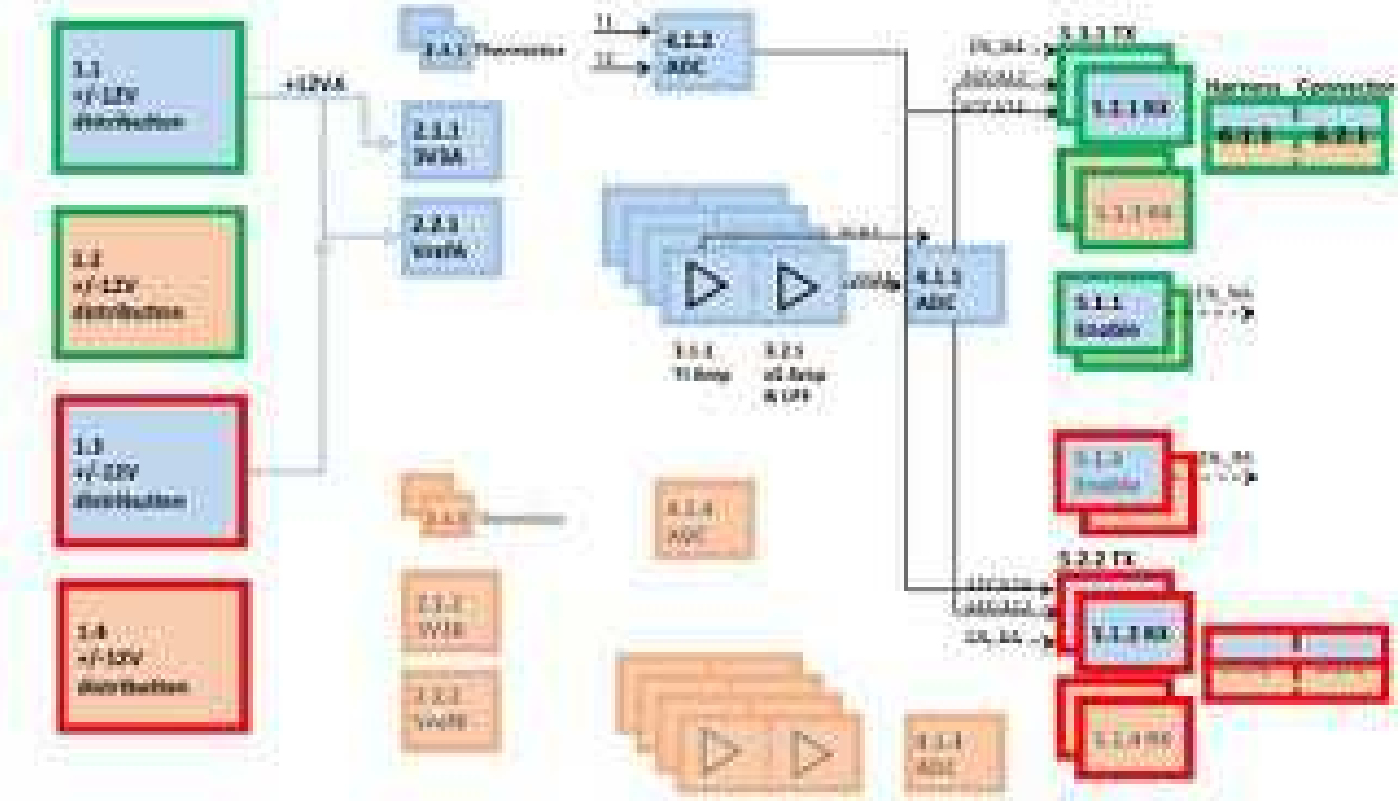

Figure A.13: A functional splitting of the SPS design. Green/red colors mark the nominal/redundant parts of the electronics, light blue and pink distinguish the set A from the set B.

A.5 Connector pinout

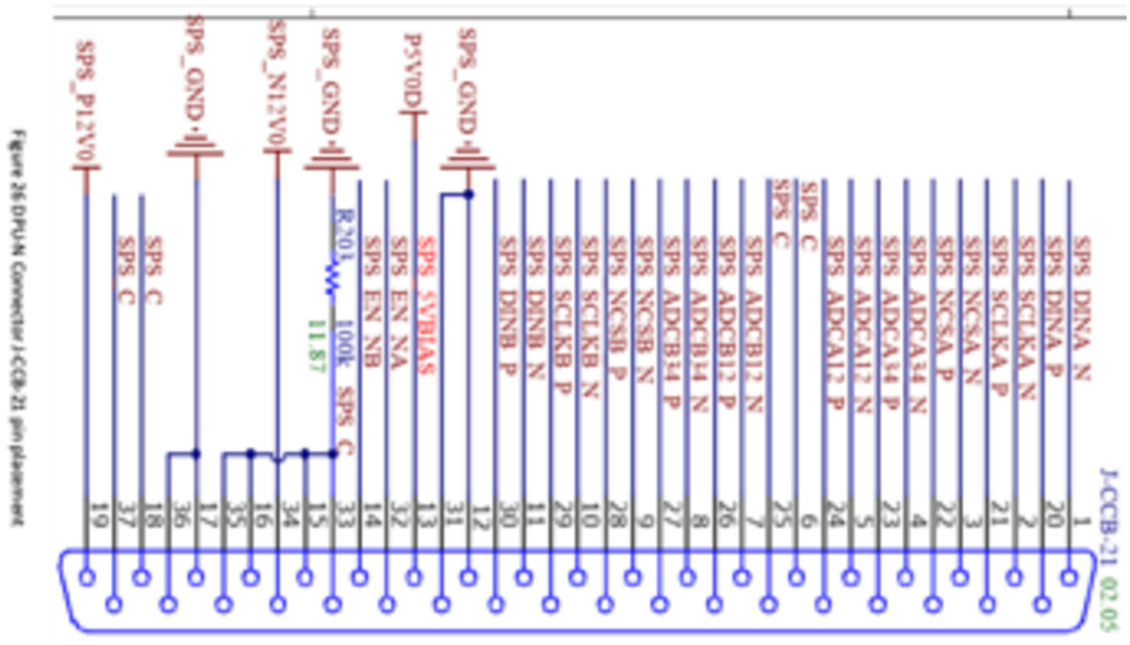

Figure A.14: CCB pinout.

Pin No	DIR	Signal (N)	Signal (R)	Signal Type	Pin No	DIR	Signal (N)	Signal (R)	Signal Type
1	I/P	DIN_NA/	DIN_RA/	LVDS	20	I/P	DIN_NA	DIN_RA	LVDS
2	I/P	SCLK_NA/	SCLK_RA/	LVDS	21	I/P	SCLK_NA	SCLK_RA	LVDS
3	I/P	NCS_NA/	NCS_RA/	LVDS	22	I/P	NCS_NA	NCS_RA	LVDS
4	O/P	ADC34_NA/	ADC34_RA/	LVDS	23	O/P	ADC34_NA	ADC34_RA	LVDS
5	O/P	ADC12_NA/	ADC12_RA/	LVDS	24	O/P	ADC12_NA	ADC12_RA	LVDS
6	N/A	SHIELD	SHIELD	POWER	25	N/A	SHIELD	SHIELD	POWER
7	O/P	ADC12_NB/	ADC12_RB/	LVDS	26	O/P	ADC12_NB	ADC12_RB	LVDS
8	O/P	ADC34_NB/	ADC34_RB/	LVDS	27	O/P	ADC34_NB	ADC34_RB	LVDS
9	I/P	NCS_NB/	NCS_RB/	LVDS	28	I/P	NCS_NB	NCS_RB	LVDS
10	I/P	SCLK_NB/	SCLK_RB/	LVDS	29	I/P	SCLK_NB	SCLK_RB	LVDS
11	I/P	DIN_NB/	DIN_RB/	LVDS	30	I/P	DIN_NB	DIN_RB	LVDS
12	N/A	GND	GND	POWER	31	N/A	GND	GND	POWER
13	N/A	5VBIAS_N	5VBIAS_R	POWER	32	N/A	EN_NA/	EN_RA/	TTL
14	N/A	EN_NB/	EN_RB/	TTL	33	N/A	SPARE	SPARE	N/C
15	I/P	SPARE	SPARE	N/C	34	N/A	-12V_N	-12V_R	POWER
16	I/P	SPARE	SPARE	N/C	35	N/A	SPARE	SPARE	N/C
17	N/A	GND	GND	POWER	36	N/A	GND	GND	POWER
18	N/A	SPARE	SPARE	N/C	37	N/A	SPARE	SPARE	N/C
19	N/A	+12V_N	+12V_R	POWER					

Figure A.15: SPS pinout.

Bibliography

[1] C. Baccani, F. Landini, M. Romoli *et al.*, "Preliminary evaluation of the diffraction behind the PROBA 3/ASPIICS optimized occulter," in *Proc. of SPIE Space Telescopes and Instrumentation, Optical, Infrared, and Millimeter Wave*, vol. 9904, 2016.

[2] A. Bemporad, "Expected penumbra illumination profile and SPS output currents for PROBA-3/ASPIICS," INAF, Tech. Rep. P3-INF-TN-14001, 19 March 2018.

[3] P. Bodin, R. Larsson, F. Nilsson *et al.*, "PRISMA: An In-Orbit Test Bed for Guidance, Navigation, and Control Experiments," *Journal of Spacecraft and Rockets*, vol. 46, no. 3, pp. 615–623, 2009.

[4] G. E. Brueckner *et al.*, "The large angle spectroscopic coronagraph (LASCO)," *Solar Physics*, vol. 162, no. 1, pp. 357–402, December 1995.

[5] S. Buckley, "SPS development model electronics design description," SensL, Tech. Rep. P3-SNL-TN-15002, 28 October 2015.

[6] ——, "SPS electronics and sensor preliminary design," SensL, Tech. Rep. P3-SNL-TN-14000, 21 January 2015.

[7] G. Capobianco, "SPS in-flight calibration plan," INAF, Tech. Rep. P3-INF-PL-17009, 31 July 2017.

[8] ——, "SPS on-ground calibration plan for DM, EQM and FM models," INAF, Tech. Rep. P3-INF-PL-17004, 4 August 2017.

[9] M. Casti *et al.*, "PROBA-3 formation-flying metrology: Algorithms for the Shadow Position Sensors system," in *Proceedings of the International Conference on Space Optics ICSO 2018*, 2018.

[10] ——, "Fine positioning algorithm for the ESA PROBA-3 formation flying mission," in *IEEE International workshop on Metrology for Aerospace*, 2019.

[11] M. Casti, "Implementation and error analysis of the algorithms for PROBA-3/ASPIICS F2 Metrology," INAF, Tech. Rep. P3-INF-TN-17024, 20 October 2017.

[12] ——, "SPS algorithms for PROBA-3/ASPIICS F2 metrology," INAF, Tech. Rep. P3-INF-TN-17022, 20 October 2017.

[13] A. N. Cox, *Allen's astrophysical quantities*. Springer, 2000.

[14] M. Focardi, "Trade-off study on implementation approaches of the F2 metrology for PROBA-3/ASPIICS," INAF, Tech. Rep. P3-INF-TN-14006, 29 January 2015.

[15] M. Focardi *et al.*, "Formation Flying Metrology for the ESA-PROBA3 Mission: The Shadow Position Sensors (SPS) silicon photomultipliers (SiPMs) readout electronics," in *Proc. of SPIE*, vol. 9604, no. 96040D, 2015.

[16] M. Focardi, V. Noce, S. Buckley *et al.*, "The shadow position sensors (SPS) formation flying metrology subsystem for the ESA PROBA-3 mission: present status and future developments," in *Proc. of SPIE*, vol. 9904, no. 99044Z, 2016.

[17] D. Hestroffer and C. Magnan, "Wavelength dependency of the Solar limb darkening," *Astronomy and Astrophysics*, pp. 333–338, 1998.

[18] J. Ibarz *et al.*, "PROBA-3: Demonstrating formation flying," in 4^{th} *International Conference on Spacecraft Formation Flying Technologies*, Quebec, Canada, 2011.

[19] C. Jackson, K. O'Neill, L. Wall, and B. McGarvey, "High-volume silicon photomultiplier production, performance, and reliability," *Optical Engineering*, vol. 53, no. 8, pp. 081 909–1–10, August 2014.

[20] G. Krieger, A. Moreira, H. Fiedler *et al.*, "TanDEM-X: A Satellite Formation for High-Resolution SAR Interferometry," *IEEE Transactions on Geoscience and Remote Sensing*, vol. 45, no. 11, pp. 3317–3341, 2007.

[21] F. Landini, "EO diffracton model and influence of its pattern on the SPS based F2 metrology," INAF, Tech. Rep. P3-INF-TN-14008, 29 January 2015.

[22] ——, "Evaluaton of the EO diffracton on the plane of the pupil," INAF, Tech. Rep. P3-INF-TN-15014, 14 December 2015.

[23] D. Loreggia, L. Zangrilli, and V. Noce, "ASPIICS on-ground calibration procedure," INAF, Tech. Rep. P3-INF-PR-20004, 12 February 2020.

[24] B. Lyot, "Etude de la couronne solaire en dehors des eclipses," *Zetischrift fur Astrophysics*, vol. 5, no. 8, p. 73, 1932.

[25] ——, "The study of the solar corona and prominences without eclipses," *Monthly Notices of the Royal Astronomical Society*, vol. 99, no. 8, pp. 580–594, 1 June 1939.

[26] A. Mestreau-Garreau *et al.*, "PROBA-3 high precision formation-flying mission," in *4th International Conference on Spacecraft Formation Flying Technologies*, Quebec, Canada, 2011.

[27] A. Mestreau-Garreau, K. Gantois, A. Cropp, D. Evans, and F. Teston, "PROBA 3: In-Orbit Demonstration Mission for High Precision Formation Flying," in *Proceedings of the Symposium on Small Satellite Systems and Services (4S)*, 2010.

[28] G. Nicolini, "PROBA-3/ASPIICS SPS AIT plan," INAF, Tech. Rep. P3-INF-PL-18010, 21 January 2018.

[29] V. Noce, "SPS DM preliminary tests," INAF, Tech. Rep. P3-INF-RP-16004, 19 September 2016.

[30] ——, "SPS a trade-off study on dynamic range and sensitivity," INAF, Tech. Rep. P3-INF-RP-16016, 7 August 2017.

[31] ——, "SPS DM voltage supply dependency analysis," INAF, Tech. Rep. P3-INF-TN-16017, 7 August 2017.

[32] ——, "SPS error budget analysis," INAF, Tech. Rep. P3-INF-TN-15012, 23 March 2018.

[33] ——, "SPS ADM/EQM Electronics Test Plan and Procedures," INAF, Tech. Rep. P3-INF-PL-19012, 22 March 2019.

[34] ——, "SPS-EQM Functional Test Report," INAF, Tech. Rep. P3-INF-RP-19036, 25 June 2019.

[35] V. Noce *et al.*, "Metrology on-board PROBA-3: The Shadow Position Sensor (SPS) subsystem," *Nuovo Cimento*, vol. 42, no. 1, 12 June 2019.

[36] ——, "Metrology on-board PROBA-3: the Shadow Position Sensors subsystem," *Advances in Space Research*, vol. Special Issue: Sat Constellations and FF, August 2020.

[37] V. Noce, M. Focardi, S. Buckley *et al.*, "An improved version of the Shadow Position Sensor readout electronics on-board the ESA PROBA-3 Mission," in *Proc. of SPIE*, vol. 10397, no. 103971B, 2017.

[38] S. Pierattini and V. Noce, "SPS worst case analysis report," OHB, Tech. Rep. P3-INF-RP-17021, 23 March 2018.

[39] PROBA-3 team, "PROBA-3 Mission Requirements Document," ESA-ESTEC, Tech. Rep. P3-EST-RS-1006, 17 September 2008.

[40] ——, "PROBA-3 System Requirements Document," ESA-ESTEC, Tech. Rep. P3-EST-RS-1001, 10 July 2008.

[41] ——, "Proba-3 Instrument Interface Document ASPIICS Coronagraph," ESA, Tech. Rep. P3-EST-ICD-7001, 3 July 2017.

[42] E. Renotte, "PROBA-3 ASPIICS - Coronagraph System Technical Requirements Specification," CSL, Tech. Rep. P3-CSL-RS-14000, 3 April 2015.

[43] E. Renotte *et al.*, "Recent achievements on ASPIICS, an externally occulted coronagraph for PROBA3," in *Proc. of SPIE*, vol. 9904, no. 99043D, 2016.

[44] R. Rougeot, "Straylight from Earth albedo," ESA-ESTEC, Tech. Rep. P3-EST-TN-2111, 15 May 2017.

[45] R. Rougeot, R. Flamary, D. Galano, and C. Aime, "Performance of the hybrid externally occulted Lyot solar coronagraph - Application to ASPIICS," *Astronomy & Astrophysics*, vol. A2, p. 599, 2017.

[46] L. Salvador, "PROBA-3 Coronagraph System ASPIICS Thermal Analyses," CSL, Tech. Rep. P3-CSL-TN-15006, 27 January 2016.

[47] U. Schlifkowitz, E. Finsterle, and W. Schmutz, "Development of a Phase-sensitive Absolute Radiometer for Space and Ground-based Use," in *Proceedings of the 17th ESA Symposium on European Rocket and Balloon Programmes and Related Research*, 2005, pp. 467–469.

[48] J. S. Servaye, "PROBA-3 Coronagraph System Project Management Plan," CSL, Tech. Rep. P3-CSL-PL-14000, 29 October 2014.

[49] J. Sørensen, "Environmental specification," ESA-ESTEC, Tech. Rep. P3-EST-RS-6003, 26 September 2008.

[50] C. Thizy, "PROBA-3 ASPIICS - SPS Requirements Specification," CSL, Tech. Rep. P3-CSL-RS-14001, 21 February 2017.

[51] C. Thorne, "PROBA-3 Coronagraph system Product Assurance and safety requirements," CSL, Tech. Rep. P3-CSL-PL-14001, 24 October 2014.

[52] S. Vivès *et al.*, "Recent developments of ASPIICS: a giant solar coronagraph for the ESA/PROBA-3 formation flying mission," in *Proc. of SPIE*, vol. 8862, no. 886209, 2013.

[53] W. Xiang and J. L. Jorgensen, "Formation Flying: A subject being fast unfolding in space," in *5th IAA Symposium on Small Satellites for Earth Observation*, 2005.